The Nanoscale Structure of Fully Dense Human Cortical Bone

The Nanoscale Structure of Fully Dense Human Cortical Bone

By

ELIZABETH A. MCNALLY, B.SC.

A Thesis

Submitted to the School of Graduate Studies

in Partial Fulfillment of the Requirements

for the Degree of

Doctor of Philosophy

McMaster University

DOCTOR OF PHILOSOPHY (2010)	McMaster University
(Department of Materials Science and Engineering)	Hamilton, Ontario

TITLE:	The Nanoscale Structure of Fully Dense Human Cortical Bone
AUTHOR:	Elizabeth A. McNally, B.Sc.
	(Queen's University at Kingston, Ontario)
SUPERVISORS:	Gianluigi A. Botton and Henry P. Schwarcz
NUMBER OF PAGES:	xvii, 145

Abstract

The nanoscale structure of fully dense human cortical bone is explored using advanced transmission electron microscopy (TEM) techniques. Studies of fully dense cortical bone are rare because of the sample preparation challenges. In this work, cryogenic ion milling is compared favourably with traditional ultramicrotoming methods because of the clearer imaging results and better preservation of biological structures in the ion milled samples.

Ion milled samples were prepared parallel, perpendicular and at a 45 degree angle to the long axis of a human femur. The samples are cooled with liquid nitrogen while being milled to prevent heating damage to the bone structure.

Bright-field and dark-field imaging show that mineral mainly occurs as 65 nm wide, 5 nm thick mineral structures, external to the collagen fibrils, and with the long axis of the mineral running parallel to the fibrils. In samples cut parallel to the long axis of the bone, the mineral structures have their c-axes aligned with the collagen fibril long axis. In these sections the mineral structures extend up to 200 nm and are grouped into stripe-like bunches, 53 nm apart.

Samples cut perpendicular to the long axis of the bone show open areas roughly 45 nm in diameter. These open areas are assumed to be the location of collagen fibrils within the structure and are tangentially surrounded by 65 nm wide, 5 nm thick mineral structures. On average, there are 22 nm of mineral structures between adjoining collagen fibrils.

Samples cut at 45 degrees to the long axis of the bone confirm that the open structure seen in the perpendicular section is not an artefact of sample preparation. By tilting the sample, the 45 degree sample shows the structure of both the parallel and perpendicular sections. The parallel structure strongly resembles images of embryonic bone and other mineralized tissues seen in the literature, so the perpendicular open structure is not caused by sample preparation. An examination of ultramicrotoming's effect on mineral structure size compared with that of ion milling shows that the mineral structures in ion milled samples are twice as long as in ultramicrotomed samples, indicating that bone mineral may be damaged by the forces applied to the complex composite structure existing in fully dense cortical bone.

Using energy dispersive X-ray spectroscopy (EDXS) results and a simplified model of the locations of mineral within the collagen/mineral framework, a calculation of the percentage of external mineral was performed. The result showed that 80 ± 6 % of the mineral in fully dense cortical bone must be external to the collagen fibrils to obtain the EDXS results.

Finally, Z-contrast tomography, based on the use of high angle annular dark-field (HAADF) imaging, was used to prepared tomographic reconstructions of the

external mineral in fully dense cortical bone. Unlike bright-field tomography, the Z-contrast technique allows examination of crystalline materials as the contrast in HAADF images is mass-thickness dependent instead of diffraction based. These reconstructions again showed the mineral tangentially surrounding 50 nm diameter cylindrical holes, assumed to be the location of collagen fibrils in all directions.

This work shows the importance of mineral that is external to the collagen fibrils to the nanoscale structure of fully dense cortical bone.

Acknowledgements

This document is the culmination of many years of work by me and support from many others. I would like to thank those who have helped me along the way:

My supervisors, Henry P. Schwarcz and Gianluigi A. Botton. This project was a stretch for all three of us, but the results stand for themselves.

Larry Arsenault, the third member of my supervisory committee. He provided the outside voice that clarified and pulled this work together.

Dr. Bob Pilliar and Dr. Marc Grynpas for conversations and guidance that helped define and steer the project.

The staff and faculty of the Canadian Centre for Electron Microscopy. Andy Duft, Fred Pearson and Dr. Carmen Andrei ensured I could make samples, look at the samples in the microscope and understand what I was doing.

The late Dr. Nigel Colterjohn donated the human bone that remained after he had performed an allograft.

Cora Tomowich analysed ground sections of the human bone to determine the degree of remodelling.

The Botton group and the Department of Materials Science and Engineering staff and students at McMaster University. Helpful, happy and a joy to be around.

Janet McNally made this thesis readable despite not fully understanding it.

My family and friends fed me, cheered me on and nodded like they understood when I talked about research.

Finally, Derek Peeling stuck by me through thick and thin. Who knew this is what you were getting into when you married me? The images of the models you made from my sketches are great.

Contents

List of Figures

List of Tables

Chapter 1

Introduction and Literature Survey

1.1 Bone

Bone makes up the largest percentage of connective tissue in the body and serves five main functions. The skeleton provides shape while structurally bones support and offer rigid attachment points for the muscles to move the body. Bones such as the ribs and skull protect sensitive organs like the lungs and brain. The skeleton also is a store of calcium and other ions necessary for proper functioning of the body. Finally, bones contain bone marrow that produces blood cells. Bone structure is optimized to perform all five these functions. It is strong but tough, able to maintain homeostasis, and can repair and remodel itself to ensure continued functioning.

1.1.1 Bone at the Macroscale

In order to perform these four main functions, bones are highly specialized. There are three main types of bones: long, flat, and irregular bones. Typically flat bones provide protection to organs while long bones support the limbs and appendages. Irregular bones form the spine and other specialized structures that protect the nervous system. The two major bone structures, cortical and cancellous, coexist within each bone type (see figure1.1).

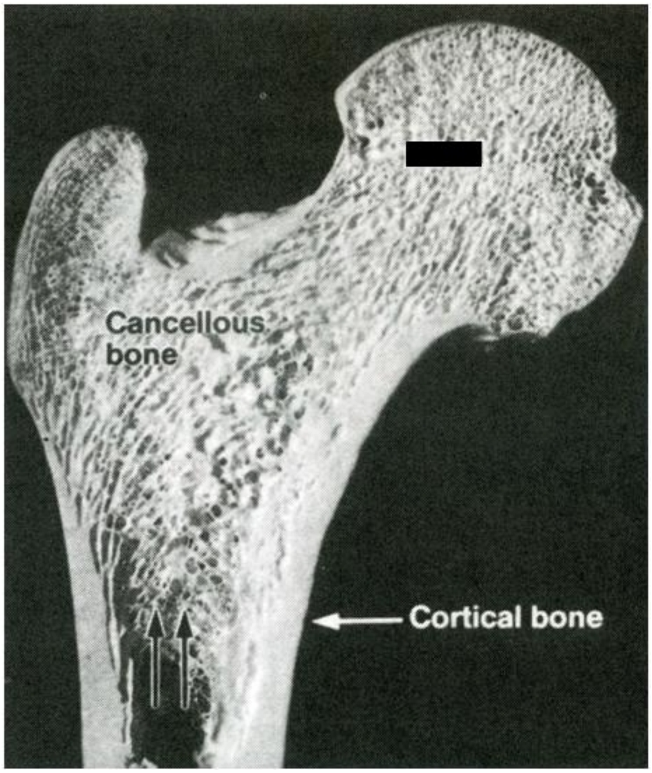

Figure 1.1: The two main bone structures shown in a femur cut parallel to the long axis of the bone. The outer shell consists of cortical bone, while the epiphysis and metaphysis, seen at the top of the image, are filled with cancellous bone. From Recker & Barger-Lux (2002).

Cortical bone is dense and strong; it forms the outer layer of all bones. For long bones, cortical bone provides most of the strength and load bearing capabilities. Cancellous bone is low density bone; its structure is sometimes described as spongy.

The diaphysis (central portion) of long bones consists of a cylinder of cortical bone (see figure1.1). At either end, cancellous bone fills in the cortical shell of the epiphysis and metaphysis to provide additional strength and a framework for the attachment of bone marrow. Flat bones like the skull and the irregular bones of the vertebrae have a thinner shell of cortical bone and are filled with cancellous bone and marrow.

1.1.2 Microscale Components of Cortical Bone

At the microscale, cortical bone consists of the extracellular matrix and the cells that build, maintain and resorb bone.

Extracellular Matrix

The extracellular matrix (ECM) forms the structure in which the cells of bone live and on which they act to create the form of the skeleton. The ECM is composed of 35 percent protein by weight when dry while the other 65 weight percent is mineral (Recker & Barger-Lux, 2002).

Cells

Osteoblasts Osteoblasts are differentiated mesenchymal cells that produce the collagen and other proteins that form the bone's extracellular matrix before mineralization occurs (Ducy *et al.*, 2000). This unmineralized matrix is called osteoid. In humans mineralization of the osteoid occurs 10-15 days after its formation (Baron, 2003).

Osteocytes Osteocytes are osteoblasts that have reached the final stage of cellular differentiation. They are surrounded by the ECM and have long processes that reach through the ECM in canaliculi to contact other osteocytes. Osteocytes play an important role in maintaining the skeleton. When the osteocytes in a volume of bone die, that volume will undergo remodelling (Olsen, 2003).

Osteoclasts Osteoclasts are multinucleated cells that resorb bone. They form when RANKL and CSF-1 cause blood monocytes to fuse (Boyle *et al.*, 2003). Osteoclasts are attracted to a site that needs resorption by chemoattractants. The osteoclast attaches to the bone using a sealing zone rich in f-actin and integrins. In the volume between the cell and the bone surface, a ruffled border creates a large surface area for a number of proton pumps to reduce the pH to approximately 4.5 at the bone surface (Teitelbaum, 2000). This low pH dissolves the mineral in the bone while added proteolytic enzymes including cathepsin K digest the proteins (Pollard *et al.*, 2008).

Remodelling Remodelling is the process by which a bone remakes itself. The cells involved in remodelling all have a specific purpose and typically balance to form a unit that tunnels through and replaces the bone. The balance between the removal and rebuilding of bone can be shifted to the removal side resulting in the net reduction of ECM, which is the basis of the bone disorder called osteoporosis. This balance is controlled by hormones like estrogen and parathyroid hormone as well as factors such as TGF-β and insulin-like growth factor released from the old matrix during resorption by osteoclasts (Harada & Rodan, 2003).

In cortical bone, the bone remodelling unit is called an osteon or Haversian system. First, osteoclasts cut a tunnel through the bone about 150 μm in diameter. Several days after the bone is dissolved, a lining of osteoblasts create new layers of osteoid filling the tunnel with concentric rings of new collagen (see figure 1.2). Osteoblasts that are surrounded by osteoid differentiate to form osteocytes and extend their processes through the ECM to maintain the bone. Within 200 days of initial cutting, the osteon is completely refilled with bone (Baron, 2003).

The resulting structure is a series of concentric lamellae centred on a blood vessel that nourishes the cells and connects them to the rest of the body (see figure 1.3). New osteons have cut through the existing bone structure. Over time, the entire bone will remodel with new osteons cutting through remnants of older osteons (Pollard *et al.*, 2008).

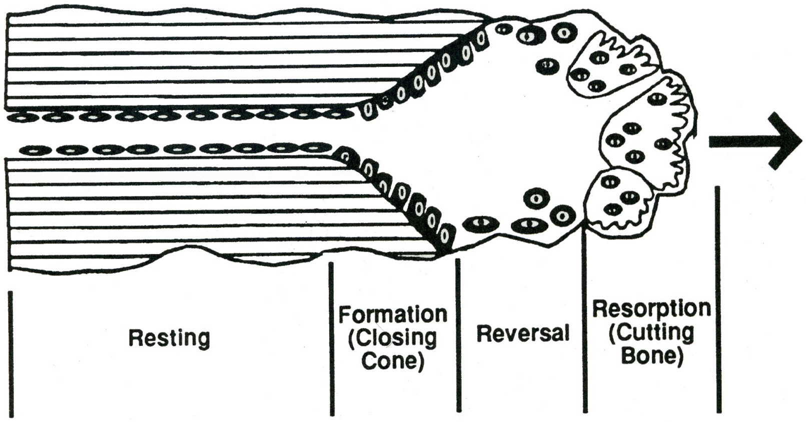

Figure 1.2: A Haversian system remodelling bone. From right to left the bone is digested, collagen is deposited and the new bone is mineralized. From Dempster (2002).

Figure 1.3: Polarized light microscope image of a cross section of cortical bone showing concentric circles of osteon structures. The remainder of older osteon structures that have been partially remodelled can be seen. From Dempster (2002)

1.1.3 Nanoscale Components of Cortical Bone

Bone consists of two main components: collagen and mineral. These two materials form the nanostructured composite material that makes bone so well adapted to its purpose. The collagen provides flexibility and fracture toughness, while the mineral provides stiffness and load bearing capabilities.

Collagen

89 % of the protein by weight in bone is type I collagen and the remainder is non-collagenous proteins and proteoglycans (Recker & Barger-Lux, 2002). Single collagen α-helix molecules are secreted from the cell. Two α_1 and an α_2 chains combine to form a right handed triple helix. In type 1 collagen every third amino acid in the collagen sequence is glycine. Immediately after the glycine in the collagen amino acid sequence is usually a proline or hydroxyproline. The third amino acid in every triplet varies. The presence of glycine in the structure kinks the α-chains, allowing them to twist around each other to form a triple helix. The dimensions of a single collagen triple helix are 1.5 nm in diameter by 300 nm in length.

After the triple helix has formed, collagen molecules assemble into larger structures called fibrils. A fibril consists of collagen helices docked together to form a long-ranging three-dimensional structure. The docking pattern is known to have a well defined gap between the end of one collagen triple helix and the start of the next one along the helical axis (Hodge & Petruska, 1963). The gap is 40 nm in length and is staggered between helices so the fibril holds together. On either side of the gap zone is a 27 nm long overlap region. The result is gap zones and overlap zones having a ratio of four collagen triple helices for every five helices in the overlap zone. This structure is shown schematically and with TEM imaging in figure 1.4.

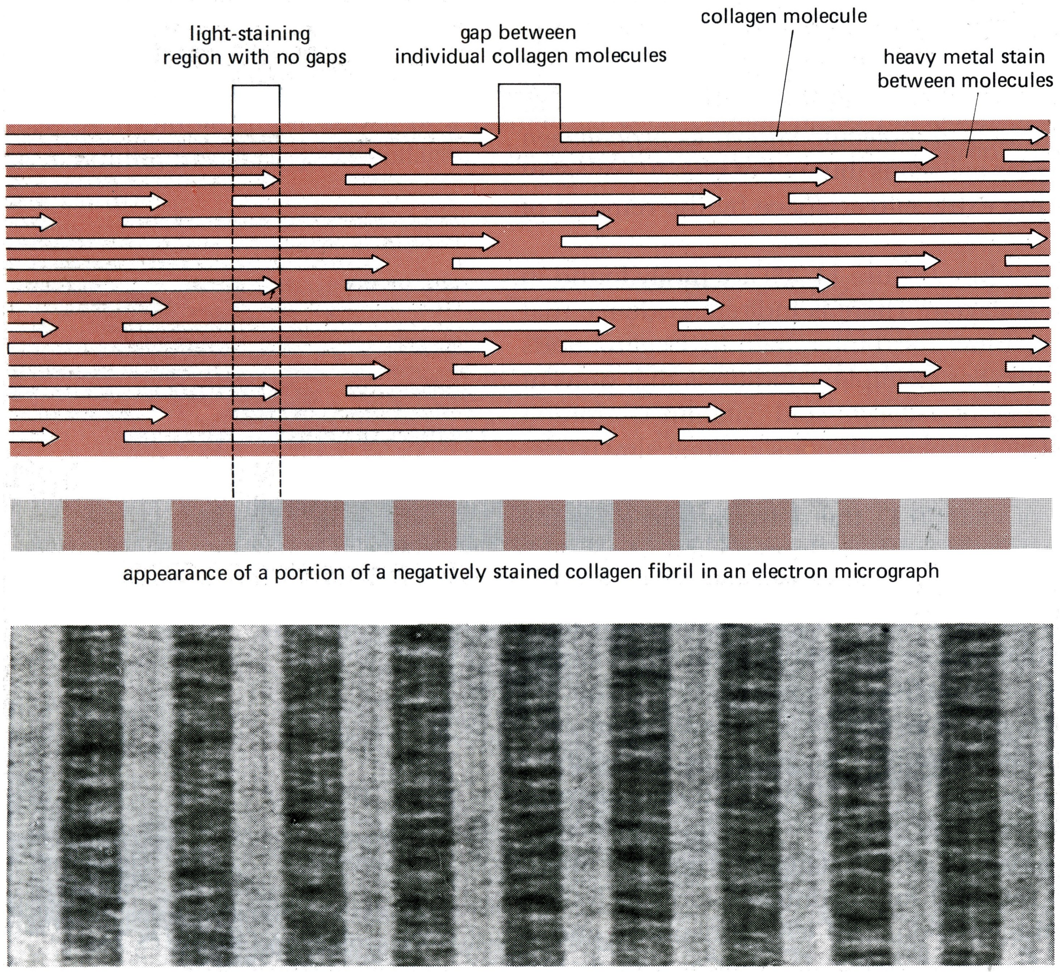

Figure 1.4: Staggered structure of collagen helices leading to striated TEM image. The 40 nm gap between molecules forms a gap that accepts stain (top). The gap is then visible in electron micrographs (bottom). From (Alberts *et al.*, 1989).

Mineral

The mineral in bone is a form of substituted hydroxyapatite (HA). It has the chemical formula $Ca_5(PO_4)_3OH$ and a hexagonal crystal structure, with $P6_3/m$ symmetry (Elliott, 2002). HA occurs only rarely on the earth's surface, yet it is abundant in bone and tooth structures. In the HA unit cell, consisting of two chemical units of HA, the phosphate tetrahedra of the structure are linked by calcium atoms and the hydroxyl groups form columns through the material aligned with the C-axis (Kohn *et al.*, 2002), as seen in figure 1.5. In bone, the mineral contains about 4-5% CO_2 present as CO_3 substituting for OH (A-type substitution) and PO_4 (B-type substitution) in the crystal structure. As well, fluorine and chlorine can substitute for the hydroxyl group and divalent (and some trivalent) ions can substitute for the calcium ions. These substitutions change the bonding within the crystalline structure and change the way it behaves compared to pure HA.

The shape of the HA in bone has been the subject of significant research. Hexagonal crystals form hexagonal prisms when unconstrained (Kohn *et al.*, 2002). The mineral in bone does not conform to this shape. Robinson and Watson were among the first to use transmission electron microscopy (TEM) to examine bone in the form of shavings of human rib cortexes that were then microtomed. They identified the mineral as platelet shaped structures aligned to the collagen fibrils based on the direction of the collagen banding (Robinson & Watson, 1952). Later, Fernandez-Moràn and Engstrom ultramicrotomed embedded bone and using

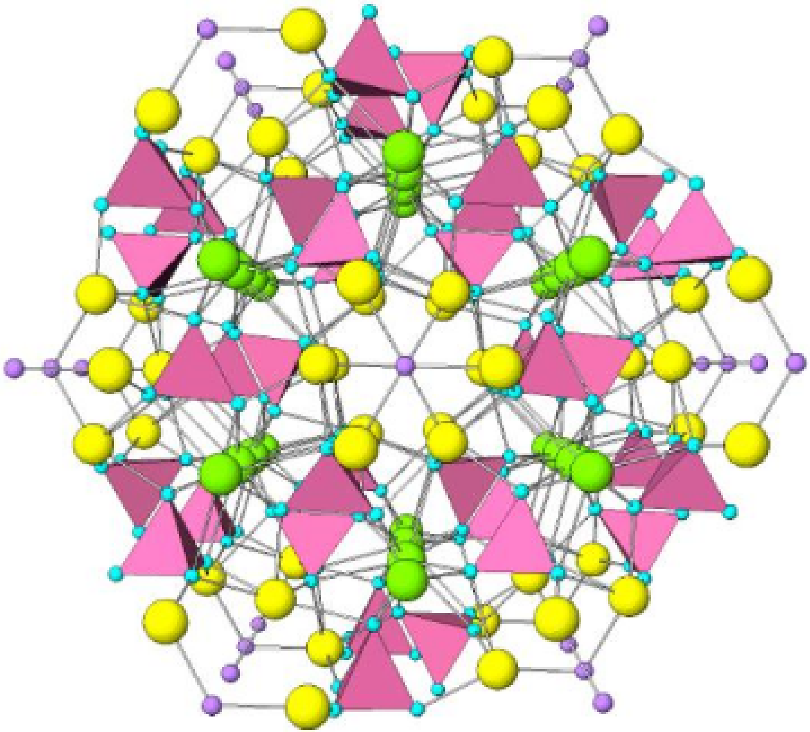

Figure 1.5: The crystal structure of apatite viewed down the [001] crystallographic axis. The structure consists of $(PO_4)^{3+}$ groups (pink tetrahedra), monovalent anions like F^- and $(OH)^-$ (purple spheres) in the ”tunnels” parallel to [0001], and Ca^{2+} cations in two coordinations: seven- and nine-fold. The CaO_6OH and CaO_9 polyhedra are colored yellow and green, respectively. From Chakhmourdian (2009).

TEM determined that the mineral is present in the form of plates and needles with the long axis of the structures aligned to the long axis of the collagen. They further suggest that the plates may be made of aggregates of needles (Fernandez-Moràn & Engstrom, 1957). Speckman and Norris noted in a brief article in Science in 1957 that there are two possibilities in the literature at that time for the form of mineral in bone: needles and plates, but their work suggests rods (Speckman & Norris, 1957). In the 1980s, Arsenault and his colleagues used cortical rat bone to show mineral in plates. They show that tilting the plates can make them look like needles and that the contrast changes significantly when tilting (Arsenault & Grynpas, 1988). Their work also suggests that the mineral plates are polycrystalline; they are not single crystals, rather they consist of small crystals that have come together to form a larger structure (Arsenault & Grynpas, 1988).

The research mentioned above uses samples of bone to determine the shape of the mineral. Significant work has focused on the examination of mineral removed from the organic matrix to study the size and shape of the mineral structure. This type of study uses finely ground bone powders that are exposed to an agent for collagen removal. The HA is left behind, resuspended in a carrier fluid, and then placed on a carbon film coated TEM grid for examination. This process exposes the HA structure to the large forces involved in grinding and to chemical attack during the collagen removal process.

Weiner's group performed several experiments using NaOCl in water to remove the collagen and other organics from the mineral. Their work shows that the majority of mineral in human femora is thin plates between 30 and 75 nm long, 15 and 45 nm wide and unspecified thickness (Weiner & Price, 1986). The work by Eppel et al. also shows the importance of technique in the measurement of mineral size. Atomic force microscopy (AFM) and TEM measurements of the same bone mineral powder show significantly different bone crystal sizes (Eppell *et al.*, 2001).

Several groups have used X-rays to understand bone mineral. X-ray diffraction results show the extent of uniformly crystalline areas in a sample. The results suggest much smaller HA structures than TEM or AFM results (Elliott, 2002).

One explanation is that the HA structures are polycrystalline; they have domains of uniform crystal structure with different orientations that border each other. Each of the small grains diffract at a different angle and the X-ray results show that the mineral is small since the individual grains are small (see figure 1.6(a). Another possibility is substitution in the HA structure, which changes the lattice spacing in the region around the substitution and causes the diffraction parameters to change (see figure 1.6(b)). Peak broadening techniques are used to determine the size on this scale, but the broadening caused by one short crystal dimension hides the narrow peak caused by the other larger dimensions.

1.1.4 Nanoscale collagen/mineral structure

The structure of collagen and mineral in fully dense cortical bone is not well understood. This review will focus on analyses based on TEM although other studies have used the related technique of AFM.

The earliest electron microscopic studies of bone focused on identifying the shape and size of the mineral. They also determined that the c-axis of the mineral is aligned with the collagen fibril long axis, as discussed in the previous section. Later research on the collagen mineral structure has been performed on mineralizing tendon. This tissue starts as a type I collagen tendon in the leg of a bird that gains mineral as the bird ages. Mineralizing turkey leg tendon (MTLT) is most commonly used due to its availability and large size compared with other birds. MTLT is an ideal tissue for sample preparation. It is easily sectioned into

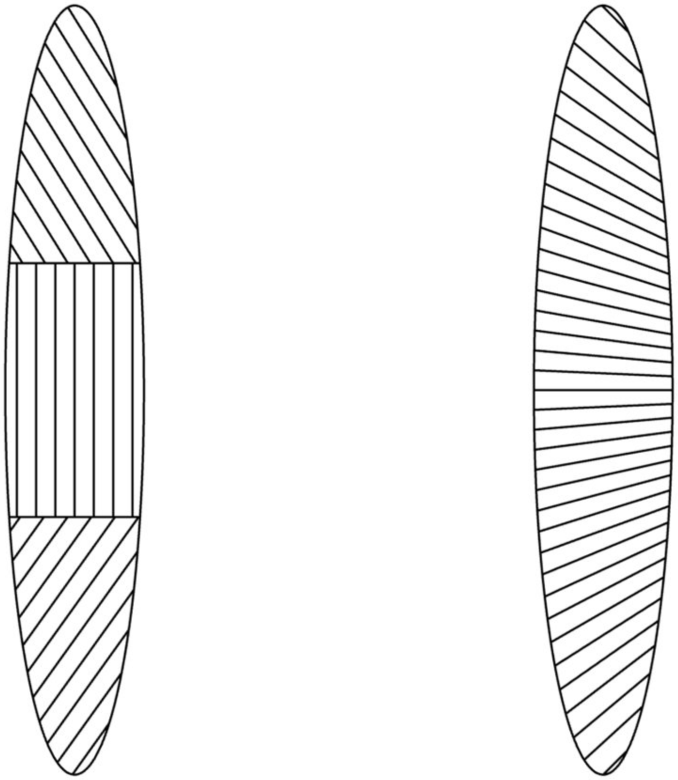

(a) polycrystalline (b) twisted, deformed or substituted lattice

Figure 1.6: TEM bright-field (BF) and diffraction methods can result in different measurements when the structure is polycrystalline, deformed, or substituted. In figure 1.6(a) the polycrystalline structure contains three smaller zones with aligned lattice spacing. Diffraction methods will measure the size of the smaller aligned zones, while TEM BF will measure the overall size of the structure with all three zones. In figure 1.6(b) the lattice is perturbed by being twisted, causing the lattice spacing and direction to gradually vary from one end of the structure to the other. Diffraction methods measure the size of the area with uniform spacing, so they would measure a small section of this structure, while TEM BF methods would measure the entire structure.

the thin sections needed for TEM. The length of a mineralizing tendon contains a spectrum from unmineralized tissue to fully mineralized tissue, allowing the initial states and locations of mineralization to be examined (Landis, 1986). A typical image of ultramicrotomed mineralizing tendon cut parallel to the long axis of the tendon is shown in figure 1.7.

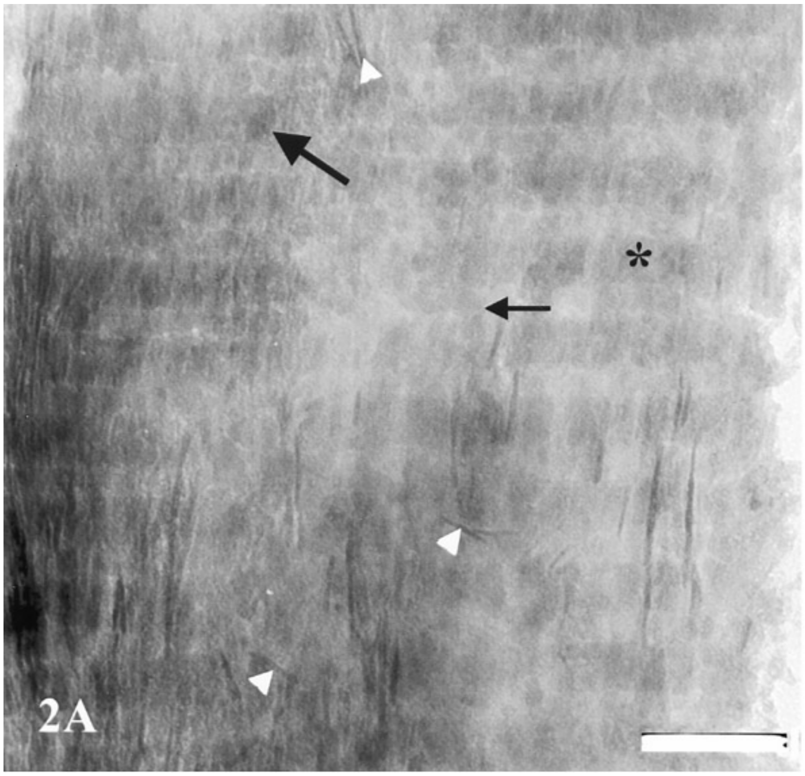

Figure 1.7: A typical mineralizing tendon long section. Wide arrow indicates gap zone mineral, narrow arrow indicates overlap zone mineral, asterisk indicates gap zone, and triangles indicate extrafibrillar mineral. Bar is 200 nm. From Prostak & Lees (1996).

The most widely accepted and cited model of bone structure on the nanoscale is that proposed by Landis et al in 1996, shown in figure 1.8. This structure is based on examination of embryonic chick bone by TEM and high voltage electron microscopy (HVEM) tomography. Plates of mineral, up to 80 nm long by 30 nm wide and 8 nm thick are located in the gap zone of collagen fibrils. The collagen molecules are aligned in one dimension such that the gap zones are next to each other to allow the 30 nm wide mineral pieces to fit into the aligned 1.5 nm wide gap zones. The mineral extends out of the gap zone along the collagen fibril as the 80 nm length will not fit into the 40 nm gap zone length. The long dimension of the plates is the crystallographic c-axis and it lies parallel to the collagen fibril axis and that the plates are parallel to each other through the diameter of the fibril (Landis *et al.*, 1996b).

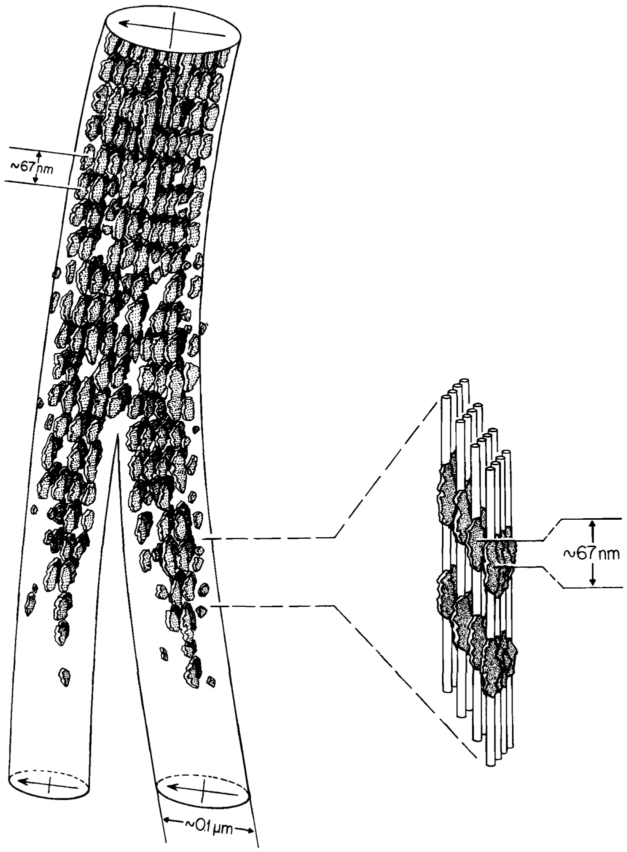

Figure 1.8: Illustration of the mineral-collagen structural relation based on the summary of previous tomographic results. From Landis *et al.* (1996b).

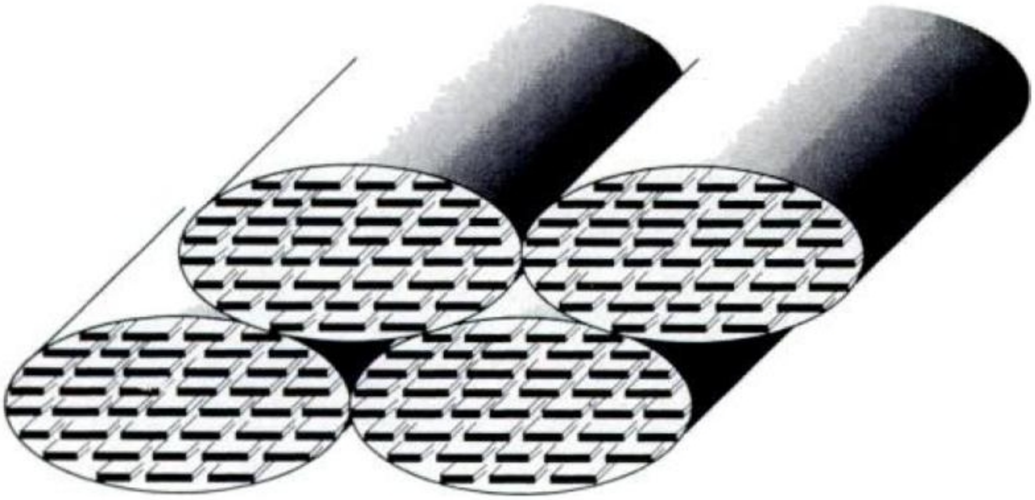

Figure 1.9: Schematic showing mineral plates running parallel to each other and to the collagen long axis in four adjacent collagen fibrils, as indicated by the images of ultramicrotomed perpendicular sections. From Weiner & Traub (1992)

Work by Weiner and Traub showed that the mineral within the collagen fibril is aligned in parallel layers as shown in figure 1.9.

A complementary HVEM tomography study on MTLT showed that some mineral forms on the outside of the collagen fibril (Landis *et al.*, 1996a) This external mineral is shown in figure 1.10 and has been alluded to by other researchers (Weiner *et al.*, 1991; Hohling *et al.*, 1971; Engstrom & Fernandez-Moràn, 1956; Arsenault, 1989; McKee *et al.*, 2005). Lees and Prostak showed significant extrafibrillar mineral arranged around the collagen fibrils and varied arrangement inside and outside the fibrils in MTLT and bone (Lees, 1979; Prostak & Lees, 1996). Cui's group in 2007 presented evidence of cylindrical shaped mineralization surrounding collagen fibrils using TEM and AFM of zebrafish (Ge *et al.*, 2007). More recently, Hong et al. showed ultramicrotomed

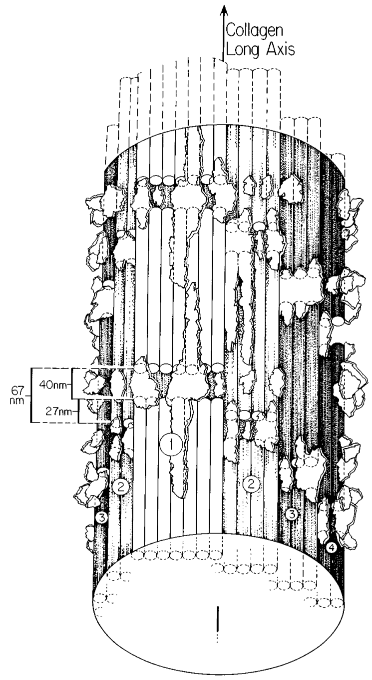

Figure 1.10: Landis et al. model of extrafibrillar mineral. From Landis *et al.* (1996a).

sections of murine femora and found that the parallel and perpendicular sections display the same structure (Hong *et al.*, 2009). It is also known that bone crystal size increases with the age of a bone (Bonar *et al.*, 1983; Kuhn *et al.*, 2008), therefore work with fully dense bone would complement the studies of MTLT, animal bone, and embryonic bone.

That some mineral is external to the collagen fibrils in fully dense cortical bone is not surprising. The gap zones in collagen comprise 12% of the volume of a fibril. Bone is 40 to 45 volume % mineral (Jager & Fratzl, 2000). Assuming the extension of the mineral plates to be twice as long as the gap zone, 15 to 20 volume % of the mineral would remain unaccounted for in this model. External mineral was observed by Sasaki et al. using AFM, and they estimated that 77 % of the mineral in cortical bone is external to the collagen fibrils (Sasaki *et al.*, 2002). The model resulting from their AFM data is shown in figure 1.11. Bonar et al. used neutron diffraction results to conclude that a large portion of the mineral in bone is external to the collagen fibrils (Bonar *et al.*, 1985). Modelling the mechanical behaviour of bone by Pidaparti et al. showed that 75 % of the mineral in cortical bone must be external to the collagen fibrils to obtain the mechanical properties demonstrated by bone (Pidaparti *et al.*, 1996).

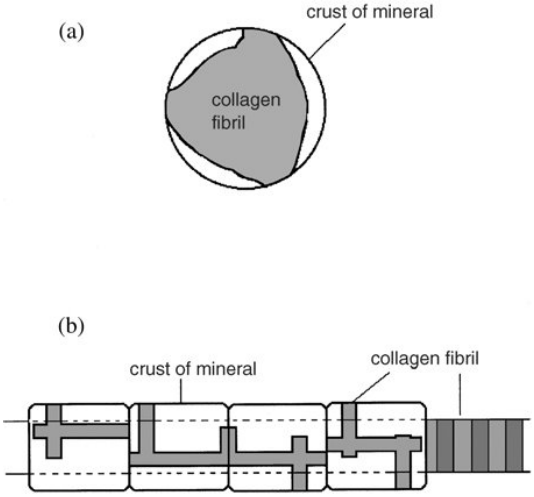

Figure 1.11: Sasaki et al. model for mineral around collagen fibrils. In part (a) the collagen fibril is cross sectioned, showing the mineral crust incompletely surrounding the collagen fibril. In part (b) a banded collagen fibril runs in the plane of the page. Plates of the mineral crust are shown lying face on, on top of the fibril. The lines running out of the fibril represent cross links to other collagen fibrils. From Sasaki *et al.* (2002).

While the previously discussed TEM experiments relied on samples prepared by ultramicrotoming, Cressey and Cressey in 2003 reported work using ion milling to create samples of modern sheep and historic human bone. They created samples cut both parallel and perpendicular to the long axis of the bone, as seen in figure

1.12. They also presented a model, showing external mineral with thin bridges into the collagen (Cressey & Cressey, 2003).

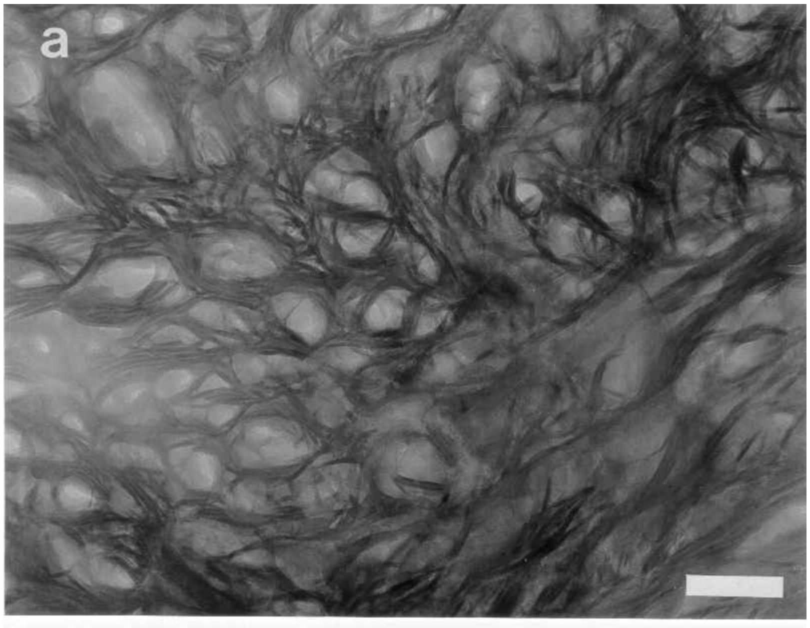

Figure 1.12: Cressey and Cressey's Perpendicular Section, bar is 100 nm. From Cressey & Cressey (2003).

Jantou et al. used focused ion beam milling to produce samples of dentin (Jantou *et al.*, 2009). A later work by the same group showed a significant portion of the mineral external to the collagen fibrils in ivory dentine (Jantou-Morris *et al.*, 2010).

Chapter 2

Research Objectives

While many other groups have attempted to understand the nanoscale structure of fully dense human cortical bone, advances in many areas make undertaking a new study of this material warranted. Using cryostage ion milling to preserve the structure of the bone without creating artefacts by crushing or fracturing the sample with ultramicrotoming or overheating the sample with traditional ion milling will ensure the bone's structure reaches the microscope intact. The addition of an amorphous carbon layer to reduce charging effects and damage allows examination of the samples for longer periods in new microscopes with better stability and resolution that obtain clearer images of the sample. Advances in the understanding of tomography reconstruction point to the need to use techniques like HAADF to remove diffraction contrast in samples like bone that contain crystalline materials. The goal of the research is to determine the nanoscale location, size and shape of the majority of the mineral component of bone.

Chapter 3

Experimental Methods

3.1 Sample Preparation

Fully dense cortical bone from the femur is the material used in this study. TEM microscopy requires samples that are electron transparent so the goal of sample preparation is to create thin samples without distorting the nanostructure of the material. The series of steps used to create a TEM sample from a large piece of bone is shown in figure 3.1. Details of the process are described below.

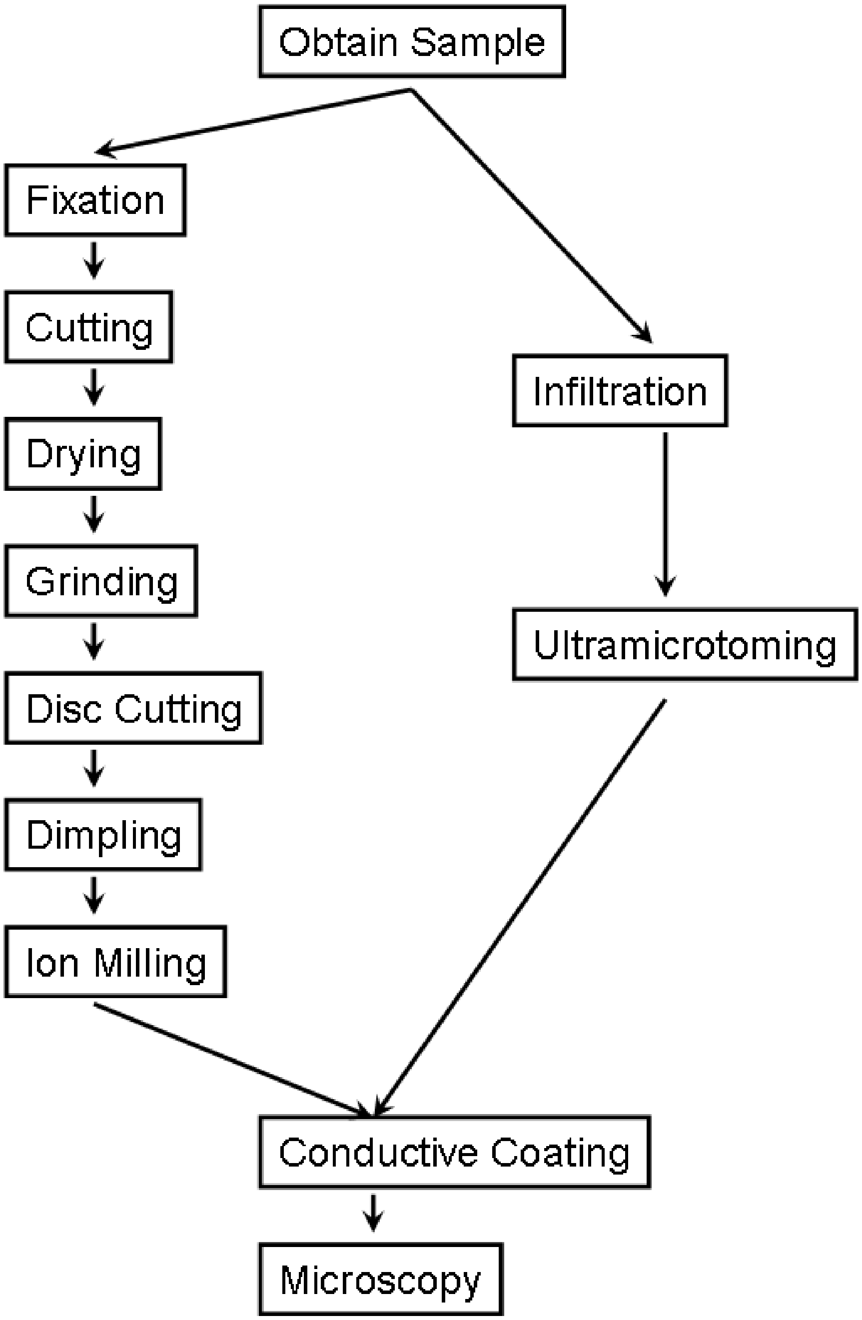

Figure 3.1: A flowchart showing the steps used to create ion milled and ultramicrotomed samples.

3.1.1 Samples

Human Sample

The human sample was donated by the late Dr. Nigel Colterjohn following an allograft surgery. An approximately 10 cm long portion of the diaphysis (central section of a long bone) of a human femur was donated in a formalin solution. The femur was from a healthy 60 year old male and was stored in a bone bank prior to receipt by Dr. Colterjohn. The bone was clean with no attached tissue or marrow. Ethical approval for this study was obtained from the Human Tissue Committee of the McMaster University Research Ethics Board, project number 08-198T. More than 30 samples from this single bone were sectioned, prepared and examined by TEM as part of this research. An optical microscopic study of the donated bone by Cora Tomowich (McMaster University undergraduate student) shows that the bone was extensively remodelled, with the result that essentially all sections prepared for TEM will have been cut from osteons rather than primary lamellar bone.

Bovine Sample

Pieces of bovine femur were obtained from the butcher counter at a local market in the form of soup bones. Sections with uniform cylindrical shape were chosen to ensure the samples were prepared away from the epiphysis. The marrow and other tissues were removed by scraping.

3.1.2 Fixation

Fixation is a process that preserves the structure of a biological sample for examination and that prevents decomposition. Different fixation techniques are used depending on the structures being examined. Some techniques preserve cells while others preserve the structures around the cells.

The fixation used for the human samples in this project is formalin soaking. Formalin, a 37 wt % formaldehyde solution, prevents bacteriological or other decay and is not thought to significantly alter the collagen structure. This technique also renders the samples biologically inactive which permits their use in a normal laboratory. Since this study is focused on the examination of the extracellular material in bone, fixatives to preserve the cellular structure are not employed.

Bovine samples were fixed in ethanol during the drying process as described below.

3.1.3 Cutting

The samples were cut to reduce the sample size to the point where they can be ground and dimpled. Slices approximately 1–1.5 mm thick were cut, oriented parallel, perpendicular, or 45 degrees to the long axis of the femur using a water-cooled, slow-speed South Bay Technology Model 660 diamond saw.

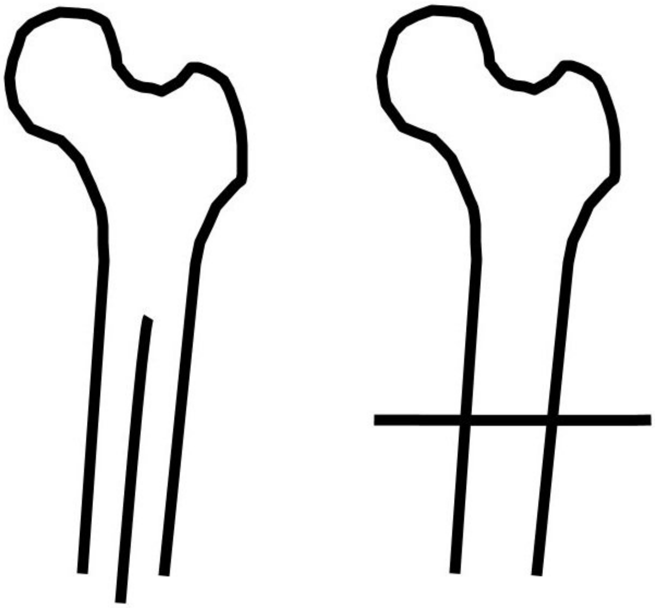

(a) Longitudinal Orientation (b) Perpendicular Orientation

Figure 3.2: Orientations of samples relative to the bone anatomy. Longitudinal sections are cut parallel to the long axis of the bone, while perpendicular sections are cut perpendicular to the long axis of the bone

3.1.4 Drying

The slices were then dehydrated in a graded series of ethanol baths. The baths were 70, 80, 90, 96 and 100% ethanol, and the slices were soaked three times at each concentration for 10 minutes (Everts *et al.*, 2003). Fresh ethanol solutions were used for each soaking period. After the final 100% ethanol bath, the slices were left in 100% ethanol overnight.

3.1.5 Infiltration

Infiltration of samples is often used in biological microscopy to preserve the structure during sample preparation and to permit sectioning by microtome. Common techniques include freezing the sample in an ice block or infiltrating it with paraffin wax or an epoxy resin. Typically, the sample is exposed to the infiltrant under a vacuum to maximize the distance the infiltrant travels into the sample and to minimize air bubbles.

Examination of cancellous bone is enhanced with the use of infiltration due to its open structure. The density of cortical bone suggests that infiltration would be challenging and perhaps unnecessary to maintain the structure (Grills & Ham, 1989). For this reason, infiltration is not performed on samples prepared by ion milling.

3.1.6 Grinding and Disc Cutting

Grinding further reduces the sample thickness. The sample is attached to the holder with a thin layer of low temperature melting wax that is later removed with heat and acetone. Care is taken to ensure the sample is not heated beyond the softening point of the wax (measured at 75°C), preserving the structures within the sample. Silicon carbide papers are used for grinding to reduce the thickness to approximately 150 μm. The silicon carbide paper is supported by a sheet of glass to ensure the grinding maintains parallel surfaces on the sample. De-ionized water is used to cool the sample, to lubricate the paper, and to remove the waste. Initial grinding uses 600 grit silicon carbide paper and the final grinding 1200 grit. This thin sheet of bone is then cut into discs 3 mm in diameter to fit into a standard TEM sample holder using an Gatan Model 601 ultrasonic disc cutter with 600 grit SiC powders and water.

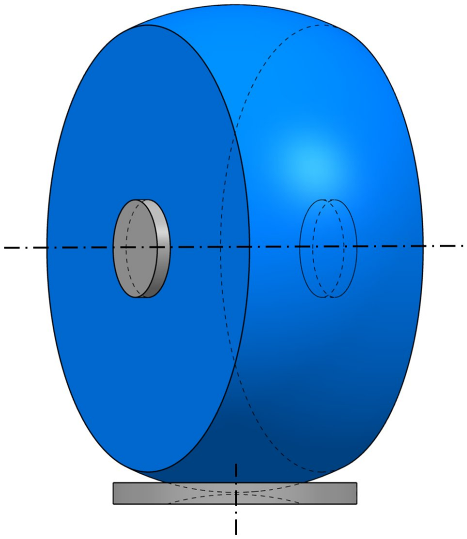

Figure 3.3: The dimpling process. The sample is attached to a rotating stub. An abrasive coated wheel with a curved edge rotates on the sample, creating a hemispherical depressing in the centre of the disc shaped sample. This process is repeated on the other side, creating a thin area approximately 30 micrometers thick in the centre of the disc.

3.1.7 Dimpling

To facilitate ion milling, the centre of the 3 mm diameter circular sample is thinned to 30 μm by dimpling on a Gatan Model 656 Dimple Grinder. The sample rotates on a puck while being eroded by a rotating wheel with an arced surface. The result is a dimple in the centre of the sample (see figure 3.3). Pastes with 8, 4, 2, and

1 μm diamonds were successively applied to the wheel to create the dimple. The dimples were polished with a felt wheel and 0.75 μm diamond paste. Both sides of the sample were dimpled; the cross section of the sample is shown in figure 3.4.

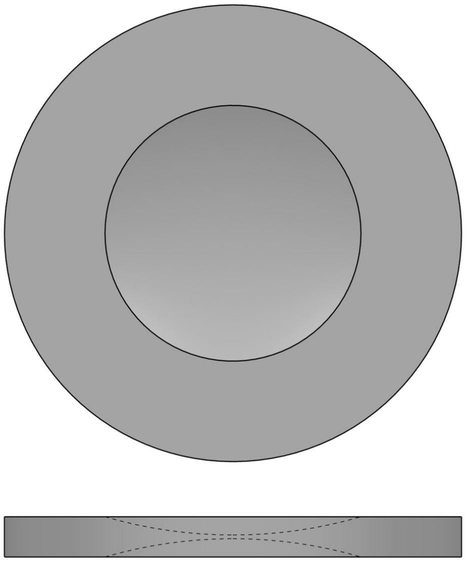

Figure 3.4: A dimpled sample has concave depressions on each side that thin the centre of the sample to minimize ion milling time.

3.1.8 Ion Milling

Ion milling utilizes a beam of argon atoms directed obliquely at the surface of the sample to erode it, resulting in a symmetrical wedge profile around a hole in the centre of the sample. The incidence angle of the beam and its energy are controlled to minimize damage to the sample. At the end of ion milling, the thickness of the sample around the hole will be in the order of tens to hundreds of nm, so the sample will be electron transparent. As the milling angle decreases, the resulting area of electron transparency increases, but the milling time also increases. Ion milling does not expose the sample to the deformation imposed by ultramicrotomy with the associated plastic deformation that causes slip or fracture within the crystalline component of bone (Boyde & Pawley, 1976; Noguchi *et al.*, 2000; Volkert *et al.*, 2004).

Ion milling is performed in a vacuum to allow the argon beam to form. Because of this, heat created by the argon ions hitting the sample will not dissipate through convective cooling. The exact temperature increase due to milling temperature obtained in the samples is unknown, but it is known that the milling process heats non-thermally conducting samples to several hundred degrees Celsius (Viguier & Mortensen, 2001). To prevent excessive heating of the sample, ion milling was performed in a Fischione 1010 Low Angle Ion Milling and Polishing System equipped with a cryostage. The mill erodes the sample's surface from above and below using argon ions at 3.0 kV and 3.0 mA while the samples are rotated. The samples were cooled with liquid nitrogen and the mill stopped milling if the stage temperature exceeded -60°C. Milling times varied, but were in the order of 10 hours to achieve a small hole in the centre of the sample. Ion milling has been used previously on bone samples (Cressey & Cressey, 2003) and cryogenically on dentin (Boyde, 1974), but the use of a cryostage to reduce heating effects on bone samples is unique to this study. By reducing heating effects, the sample should be kept at temperatures below that where the structure may degrade.

3.1.9 Ultramicrotomed Samples

Ultramicrotomed samples were prepared by Marcia Reid of the Health Sciences Electron Microscopy Lab at Hamilton Health Sciences, McMaster Campus. Small sections of dried bovine bone were embedded in Spurr's resin, then sectioned into slices between 70 and 90 nm thick using a Leica UCT ultramicrotome and a diamond blade angle of 45°. The ultramicrotomed slices were floated in water onto Formvar-coated copper grids.

3.1.10 Conductive Coatings

Bone is not electrically conductive. The material acts as an insulator. As it sits in an electron beam, the sample gains electrons, causing it to deteriorate and reducing the quality of the images obtained from the microscope by deflecting electrons away from the sample. To minimize this effect, a thin coating of a conductive material is applied to the sample to improve its electrical conductivity. For TEM applications, a 5-10 nm coating of amorphous carbon is often sputtered onto the sample. The amorphous carbon is electron transparent, conductive, and will not interfere with most TEM techniques making it a good choice for improving the conductivity and therefore the sample stability in the TEM.

A thin (5nm) coating of amorphous carbon was applied to all samples using a Gatan Model 682 Precision Etching Coating System. The sample was rotated during the sputtering process to ensure a uniform coating was applied. This step is not described in the work of other groups; however it allows the examination of sample in the microscope without charging and reduces the damage to the sample.

3.2 Transmission Electron Microscopy (TEM)

TEM examines samples at the nanometer scale. A basic microscope consists of an electron gun, lenses that refine the electron beam, apertures to select different portions of the beam, a sample holder and tilt mechanism, a camera to record images and a viewing screen. The system creates projections of the structure in the sample and allows the user to gather other information about the structure.

The electron gun is designed to produce a stream of high-energy electrons. These electrons are emitted with hundreds of keV of energy in a high vacuum. The electrons travel through a series of electromagnetic lenses that are used to focus the electron beam and magnify an object point (an area illuminated by the electrons) or demagnify the image of the electron source (to form a nanometer or sub-nanometer probe). As the beam passes through the sample, some of the electrons are scattered by interactions with atoms and/or planes of atoms (the crystal structure) within the sample. The resulting scattered beams can be used to create a variety of images of the sample. As well, the lenses and apertures can be operated to generate diffraction patterns of the materials in the sample. Other detectors gather data about the chemistry or bonding in the sample based on the results of the electron interactions within the sample.

3.2.1 Microscopes Used

Transmission Electron Microscopy (TEM) was performed using the microscopes at the Canadian Centre for Electron Microscopy at McMaster University. The samples were examined using two microscopes: a Philips CM-12, and an FEI Titan 80-300 Cryo In-situ. Both microscopes achieve sub-nanometer resolution, so they provide sufficient resolution to observe the nanometer scale structures expected in this work.

The Philips CM-12 was used for bright-field imaging, diffraction patterns and dark-field imaging. This microscope operates at 120 kV and can collect images on either Kodak SO-163 film or a CCD Camera (Gatan's Orius model). The film negatives are developed in a darkroom and scanned at 450 pixels per inch with a scanner. Digital image files were saved in DM3 format for inspection, measurements and analysis in Gatan's Digital Micrograph software.

The FEI Titan 80-300 Cryo In-situ operates over the range of 80 to 300 kV and stores images in digital format. This instrument is equipped with a cryo-twin lens (11mm gap in the polepiece) and dedicated cryoblades to improve the vacuum level and reduce contamination during the experiments. Bright-field imaging, Scanning Transmission Electron Microscopy (STEM), Energy Dispersive X-ray Spectroscopy (EDXS), Electron Energy Loss Spectroscopy (EELS) and tomography used the Titan TEM. The microscope was operated at 300 kV and all data was recorded in digital format.

3.2.2 TEM Imaging

For bright-field (BF) imaging the lenses and apertures are operated as shown on the right in figure 3.5. The electrons that are scattered and diffracted by the sample are stopped by an objective aperture placed in the back-focal plane of the objective lens and the unscattered, undiffracted electrons that pass straight through the sample are used to form the image. This microscope setup would result in all of the electrons hitting the screen or film if there were no sample in the microscope, hence the term bright-field. The image of the area of interest appears over a bright background. To increase the contrast in the images, the objective aperture was always used in this work.

In dark-field (DF) imaging the lenses and apertures are operated such that only electrons that are diffracted to a specific angle and location are used to form the image. These images are useful to show where specific Bragg scattering lattice planes are present in the sample, but it must be noted that only the planes aligned for diffraction to the specific area will show in dark-field imaging. Other planes with the same lattice spacing within the sample will not appear if the diffracted beam does not enter the objective aperature. With no sample in the microscope there will be no diffracted electrons. No electrons will hit the image plate and the image will be dark, hence the name dark-field. The image of the area of interest appears over a dark background.

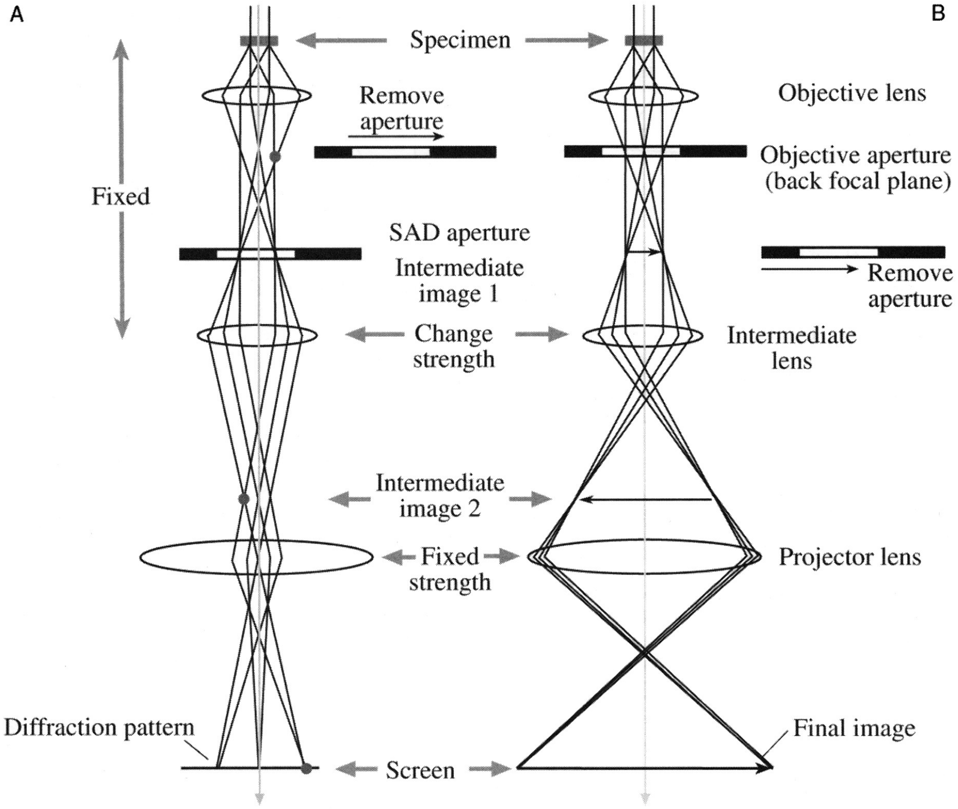

Figure 3.5: Schematic diagram of TEM electron beam path for diffraction (left) and bright-field imaging (right). From Williams & Carter (1996).

3.2.3 TEM Selected Area Diffraction (SAD)

SAD allows the user to select an area on the sample, and then observe the diffraction pattern arising from the materials in the underlying volume. If the volume contains a single crystal, the diffraction pattern in the back focal plane of the objective lens will be a series of spots that allows the determination of the crystal structure of the material and its orientation. If the selected area is polycrystalline and the crystals are randomly oriented, the diffraction pattern will be a series of rings that can be used to calculate the lattice parameters of the crystals included within the diffracted area. With this information, the material in the selected area can be identified, however its orientation may be impossible to decipher due to the large number of crystals in the selected area. If the crystals of the polycrystalline material are ordered, that is they have a degree of alignment, the diffraction pattern will not be complete rings. Instead the rings will be broken into small arcs, with the angular dispersion of the arc indicating the angular spread of the lattice plane's alignment in the material. This property is known as texture.

3.2.4 Scanning Transmission Electron Microscopy (STEM) Imaging

In STEM imaging, the incident electrons are focused into a small beam that is rastered across the sample. Bright-field images comparable to bright-field TEM images in contrast can be formed, but the strength of STEM is in dark-field techniques. Unlike dark-field TEM imaging, where a single diffracted beam at a specific angle is used to create the image, Annular Dark-Field (ADF) STEM has an annular detector that surrounds the straight through beam to collect electrons scattered to that angle in all directions around a complete circle. ADF STEM collects more signal, so the resulting images are less noisy than DF TEM images. By selecting an appropriate height for the ADF detector (also known as camera length), the inner detector collection angle can be modified and the contrast in the image can also be optimized compared to a DF TEM image. One difficulty with ADF STEM is the reduced resolution of the image. A Field Emission Gun (FEG) electron source in the TEM to reduce the energy spread of the beam improves the resolution.

ADF STEM images contain contrast formed by both Z-contrast and Bragg scattering as the collection angle is less than three times the convergence angle of the probe. Z-contrast arises from incoherently scattered electrons from interaction with an atom that are scattered through large angles whereas Bragg scattering results in only small angle scattering. To remove the Bragg scattering from the contrast, High Angle Annular Dark-Field STEM (HAADF STEM) was developed. This technique uses a circular detector with a very large central aperture, see figure 3.6. By positioning the detector an appropriate distance below the sample (changing the camera length), the effects of diffraction can be removed from the image, leaving only contrast that arises from the Z-contrast. Z-contrast is dependent on the atomic number of the atoms in the sample, with higher atomic numbers forming greater contrast. Other detectors can be used to simultaneously gather information about X-rays created within the sample or energy lost by the electron beam in the sample.

For this project, STEM was performed on the Titan. Care was taken to not let the beam dwell on any point of interest as damage would occur. High Angle Annular Dark-Field (HAADF) conditions were used for imaging, using an annular detector. The work used an 8 mrad convergence angle, a camera length of 152 mm, and an inner collection angle of 35 mrad. These conditions result in atomic number contrast, minimizing contributions from diffraction contrast.

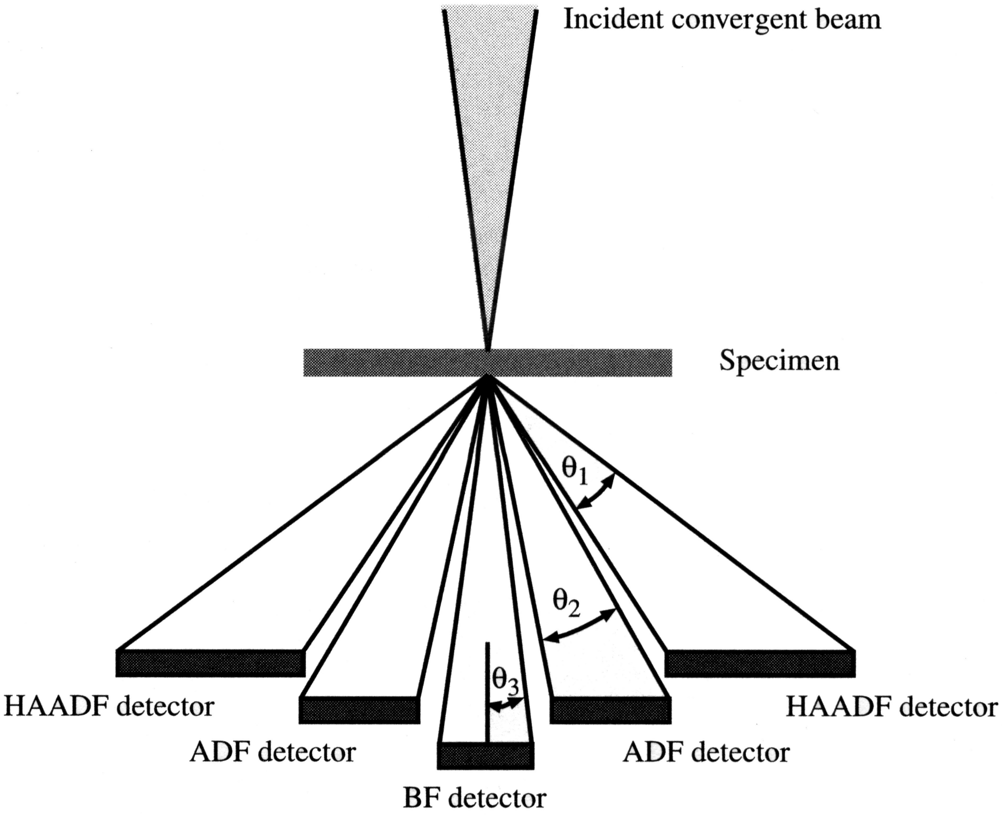

Figure 3.6: Schematic diagram of detector locations for High Angular Annular Dark-Field (HAADF) Annular Dark-Field (ADF) and Bright-Field (BF) imaging. From Williams & Carter (1996).

3.2.5 STEM Energy Dispersive X-ray Spectroscopy (EDXS)

EDXS generates information about the chemical composition of the sample. An incident electron that interacts with the electrons of an atom can cause ionization of the atom by ejecting an inner shell electron in an inelastic interaction. An outer shell electron will replace the ejected electron with the release of an Auger electron or a characteristic X-ray. The result is a spectrum of X-ray intensities for each pixel scanned in STEM mode. The resolution of the results depends on the interaction volume of the material and the escape volume of the characteristic X-ray. The interaction volume is the volume in the material where the inelastic interaction between the two electrons occurs. The escape volume defines the depth from which a characteristic X-ray will be emitted instead of absorbed in a sample. Analysis of the resulting spectra can be used to determine the types and concentrations of atoms present.

EDXS spectroscopy was performed on the Titan in STEM mode. An Oxford Instruments INCA system was used to collect the spectra and analyse the results. Since the sample must be tilted 15° towards the spectrometer to obtain correct data, this technique is limited in application.

3.2.6 Electron Tomography

TEM imaging provides a two-dimensional projection of the structure with inherent interpretation errors. Electron tomography was developed to help understand the third dimension in samples. Tomography is based on reconstruction of a three-dimensional volume from a set of two-dimensional projections. The technique has been applied to the medical field in the form of CAT (Computerized Axial Tomography) scans using X-rays, and has had applications in biological microscopy since the mid 1980s (McEwen & Heagle, 1997).

Tomography based on TEM bright-field images has been successfully applied to the reconstruction of cilia (McEwen *et al.*, 1986), macromolecules (Baumeister *et al.*, 1999), and other biological structures. Biological structures are eminently suited to electron tomography, as they have minimal diffraction contrast due to crystallinity. For valid tomographic reconstructions, the contrast in the tilt series must vary monotonically with thickness. If diffraction contrast is present in the sample, the intensity at any given point in the sample not only will vary with thickness, but also will rise and fall as the crystalline portions of the sample rotate in and out of their optimal diffraction conditions. To allow tomographic reconstruction from nanoscale images, Midgely and Weyland developed electron tomographic techniques based on Z-contrast HAADF STEM imaging. This technique uses images formed from electrons that have been strongly scattered from the straight through beam by interaction with an atom. Since this deflection is much larger than Bragg scattering from the crystal, diffraction does not contribute to the contrast in these images. The resulting tilt series has contrast that varies monotonically with the thickness of the material in the path of the electron beam, unlike BF tomography where the contrast would vary with diffraction as well. As a result, tomographic reconstruction can be performed on tilt series of crystalline materials using Z-contrast HAADF STEM (Midgley & Weyland, 2003).

Tomography was performed on the Titan in STEM mode. An Advanced Tomography Holder (model 2020) from Fischione allowing imaging with tilts up to +/- 76 ° was used. The Titan microscope tomography software was used to collect the tilt series and calibration files were created with the help of Dr. Erwan Sourty of FEI. The calibration files were also used to assist in the alignment of the resulting images.

After the Titan was electron-optically aligned and an area of interest in the sample was identified, the area was tilted to +75 and -75 ° to determine at what tilt the sample became too thick for observation with the electron beam. Areas with maximum possible tilt ranges were chosen for tomography. The sample was manually set close to the eucentric height, and then the microscope tomography setup program was used to position it at the exact eucentric height. Automatic focusing and site tracking were established as part of the setup before the tilt series settings were entered. Tilt series settings include how often to perform the autofocus steps (before every image is collected or after 2 or more images), how often to track the image shift and what tilt settings to use. A typical tilt series took images every 2 ° between -60 and +60 ° and every degree above ± 60°. A discussion of the necessity of large tilt angles and the implications for the resolution of the tomographic reconstruction is presented in appendix B.

When utilizing both the autotracking and autofocusing features, collection of a 2000 by 2000 pixel data set takes approximately 150 minutes. If either of the automatic features fails, the user is asked to focus or track manually. The focal depth is changed as the beam rasters to ensure that the entire image is in focus despite the inclination of the sample. The resulting data set is about 700 MB in size and contains approximately 90 images with their associated microscope and calibration data.

After collection of the tilt series, the images must be aligned to ensure the tilt axis in all of the images is defined and coincident. If the tilt axis is incorrectly defined, errors in the form of smearing arcs will appear in the reconstruction (see figure 3.7). Alignment can be achieved by applying markers to the sample and tracking the movement of the markers through the tilt series, or by cross correlation of features between filtered images. The alignment and reconstruction are performed on an offline computer using FEI's Inspect 3D software. The first alignment is performed using the holder calibration. This calibration takes into account imperfections in the tilt angle and shift caused by the holder and goniometer. Secondary alignment aligns the images with each other using cross correlation between features in the images. Because the tilt step between images is low, filtering and cross-correlation allow alignment of the images to within a portion of a pixel after three or four applications of the alignment process. After alignment of the images, the correct tilt axis is applied to the data set prior to reconstruction.

Reconstruction uses a direct method called the simultaneous iterative reconstruction technique (SIRT) to create a 3D model of the volume. SIRT starts with the aligned images from the tilt series, which are projections of the structure from different vantage points. The densities at various points of the images are back projected to develop a prospective volume (see figure 3.8). The total density in the prospective volume is the scaled to match the total density in the original projections. The scaled prospective volume is then projected to form a new series of images to restart the cycle. The SIRT technique is shown to achieve the best reconstruction after 15 cycles; then the reconstruction has converged to the minimum discrepancy from the true volume (Gilbert, 1972). Reconstruction is a computational and memory intensive process that requires several hours or even days to calculate structures for small volumes. When reconstruction is complete

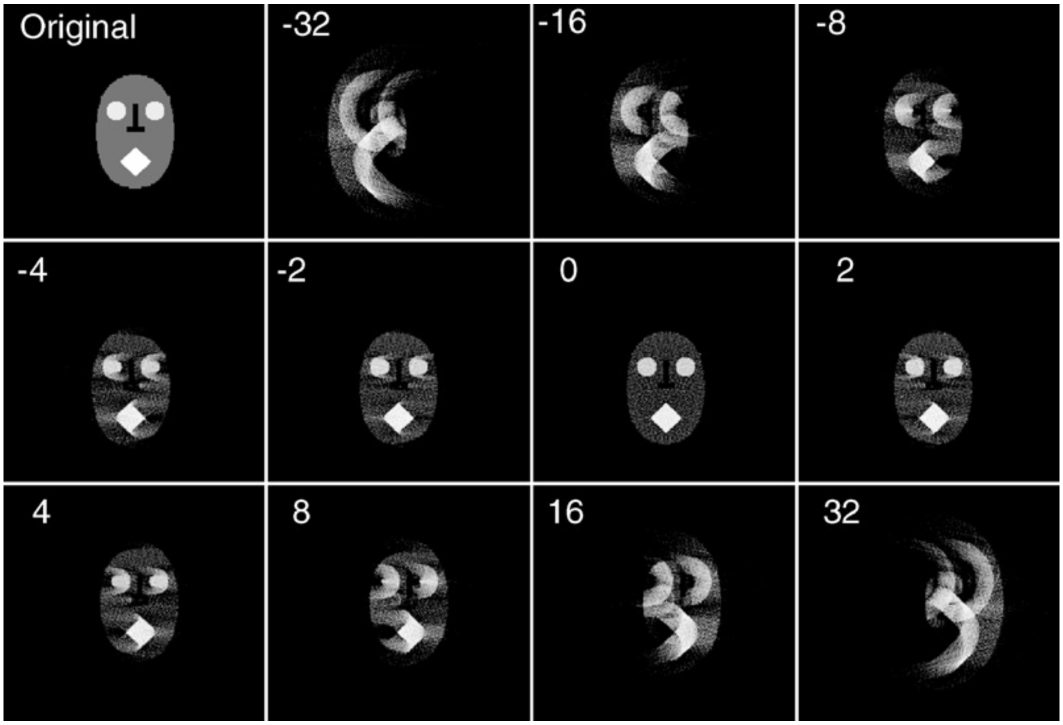

Figure 3.7: Demonstration of the effect of assigning the incorrect tilt axis on the reconstruction. The tilt axis has been shifted left or right by the number of pixels indicated and the resulting reconstruction is shown. From Midgley & Weyland (2003).

the volume is stored as a series of orthogonal slices. The slices are loaded into Resolve RT, FEI edition 4.1.2 (a form of Amira by Mercury Systems) for visualization.

The slices of the reconstruction can be viewed as slices, but segmentation is usually performed. Segmentation defines which voxels (three dimensional pixels) are surfaces in the volume. There are automated selection tools, but often the final segmentation must occur manually, making segmentation a very subjective step in the tomography sequence. A typical way to segment the volume is by grey scale. All voxels brighter than a chosen value are part of the volume of interest and the surface is at the chosen grey level. The difficulty arises in choosing the appropriate grey level. If the grey level is too high, a portion of the desired material will not be included in the volume of interest. If the grey level is too low, noise in the reconstruction may wash out fine details of the structure. Segmentation must be performed carefully to ensure that the true details of the sample are retained and that false features are not created inadvertently.

After segmentation is performed, the surfaces of the sample are rendered and displayed. If the segmentation has created a very large textured surface, rendering will take a long time. This time can be reduced by simplifying the surface but care must be used to ensure the form of the structure is respected. Both images and video montages of the surfaces can be created and displayed, facilitating observation and measurement of the structure.

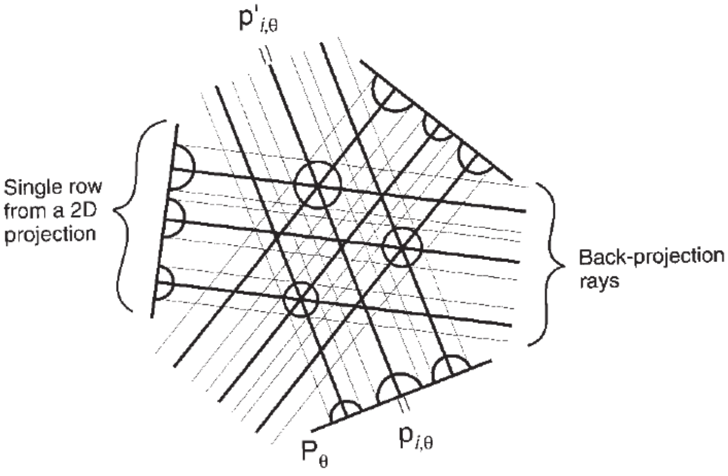

Figure 3.8: Illustration of the back projection algorithm for tomographic reconstruction. Three projections are shown as the straight lines with arcs representing high mass density in the 3D structure. For one projection, P_θ, the contents of a single pixel, $p_{i,\theta}$, and its back projection ray, $p'_{i\theta}$, are shown. Backprojection rays from the three projections intersect in the reconstruction volume indicate areas of high mass density in the original structure. From McEwen & Heagle (1997)

Chapter 4

Longitudinal Sections

4.1 Initial Imaging Results

Cryogenically ion milled samples of fully dense human cortical bone were prepared parallel to the long axis of the bone. This sample direction is expected to show collagen fibrils lying approximately in the plane of the sample. The resulting sections have a lamellar structure in one direction making the samples very sensitive to bending perpendicular to the lamellae during handling.

In the electron microscope the samples were stable under the electron beam once coated with an approximately 5 nm thick amorphous carbon layer. This amorphous carbon layer is unique to this study; it has not been described in previous works of mineralized tendon or bone. Typical imaging parameters did not cause damage to the samples. However using a highly focused beam or exposing an area of the sample to the electron beam for an extended time (>20 hours) caused sample deterioration.

4.2 Bright-Field Images

A typical image of a longitudinal section sample is shown in figure 4.1. Two features should be noted: the banding running from the upper left to lower right across the sample and long dark narrow structures running perpendicular to this banding. The banding repeat measures 67 nm which is the expected banding repeat for type I collagen. The dark sections of the banding measure 40 nm across and correspond to the gap zone in the type I collagen structure. The bright sections are 27 nm across and which would correspond to the width of the overlap zone of the collagen structure if view normal to the axis of the fibrils. This confirms that the fibrils lie oriented approximately parallel to the plane of the section.

Portions of the imaged area show banding; however the banding is not uniform across the image. The banding is visible because of the mineral present within the gap zones. As a bright-field image, the image in figure 4.1 is created by the electrons that have not been scattered through diffraction or an elastic interaction in the sample outside the objective aperture. The dark sections are dark because the electrons interact with material in the sample as they pass through this area and are scattered away from the optic axis. They are then removed by the objective aperture

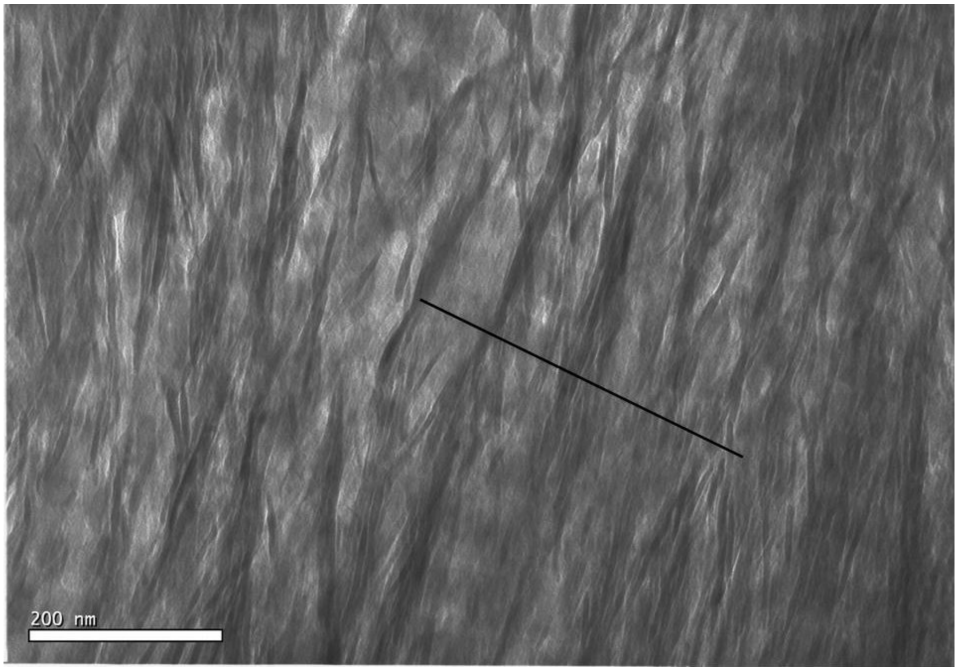

Figure 4.1: An image of a longitudinally cut section of a human femur. Collagen banding runs from the upper left to lower right parallel to the line drawn on the image and spans more than 400 nm in the image, indicating the direction of the collagen fibrils that run perpendicular to the banding. Also note the elongated structures running perpendicular to the banding, where the HA is located. The elongated structures are clustered together in bundles.

prior to image formation. The overlap zone appears brighter because the interaction between the collagen and the electron beam is much less than that between the mineral and the electron beam in the gap zone. If the boundary between the gap zone and the overlap zone is not parallel to the electron beam, the transition will not have a crisp boundary, but will instead have a gradient between the dark and light zones as shown schematically in figure 4.2. As the samples are up to 100 nm thick, it is likely that the angle of the boundary is such that the gradient completely obliterates any differences that would be seen if the collagen was viewed at an ideal angle. This means that the areas of the image with collagen banding are not the only

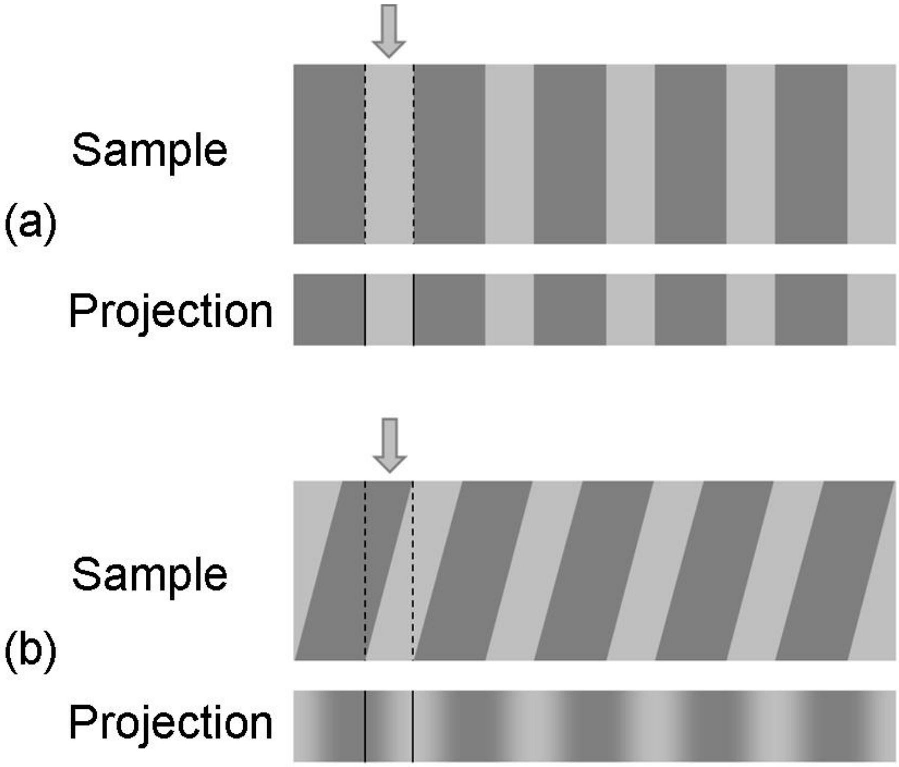

Figure 4.2: Schematic representation of projections of 100 nm thick collagen cut (a) parallel to the collagen fibrils and (b) at a 15 degree angle to the collagen long axis. Note crisp banding in (a) but contrast gradient in (b) that would be less clearly defined in images.

areas with collagen in the sample. It simply means the section was not cut perfectly parallel to the collagen fibrils in those areas so the banding is not visible.

Collagen is protein consisting mainly of carbon, oxygen, nitrogen and hydrogen atoms with low atomic numbers and little crystalline order compared with a crystalline material like HA; therefore collagen provides significantly less contrast than HA in an EM image. The majority of the contrast in an image comes from the higher atomic number calcium and phosphorous atoms and the smaller unit cell of the mineral.

4.3 Diffraction Patterns

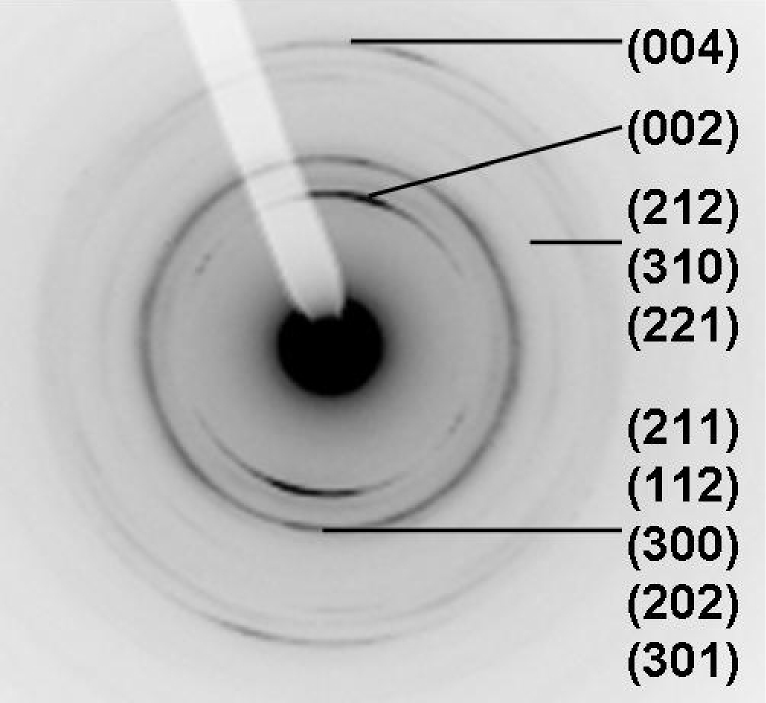

Figure 4.3: Indexed selected area diffraction pattern for an area centred on figure 4.1. The Millar indices (*hkl*) for each reflection are indicated.

Diffraction patterns of the sample are used to identify the crystalline materials present in the sample. To confirm that the samples contain hydroxyapatite (HA), diffraction patterns were formed. An example of a diffraction pattern for a selected area aperture centred on figure 4.1 is shown in figure 4.3. The crystallographic planes corresponding to the rings in the patterns have been indexed to the JCPDS powder diffraction file for HA (JCPDS 09-0432) and this therefore confirms the presence of HA in the samples. Of interest in the diffraction pattern is the shape of the different reflections. The reflections with Miller indices h and k not equal to zero appear as full circles, while the (00*l*) reflections appear as symmetric arcs spanning approximately 40 degrees in the longitudinal section diffraction patterns. Orienting the diffraction pattern to match the rotation of the image (which has been done for figure 4.3 relative to figure 4.1) shows that the mineral in bone has its c-axis aligned with the collagen long axis (Robinson & Watson, 1952; Weiner & Traub, 1992, 1986; Cressey & Cressey, 2003; Fernandez-Moràn & Engstrom, 1957). This may indicate that the long, thin dark areas seen in bright-field images are projections of the mineral in the sample; however, the diffraction pattern could arise from material within the gap zones. To further confirm that these structures are mineral, dark-field images from the (002) diffraction arcs were obtained.

4.4 Dark-Field Imaging

By selecting a specific reflection in the diffraction pattern with the objective aperture, an image can be formed showing where crystals with diffracting planes corresponding to the (hkl) at a given Bragg angle to the electron beam are located in the sample. This produces a dark-field image as shown in figure 4.4(b) with its corresponding bright-field image, figure 4.4(a). Mapping the dark-field (002) image in figure 4.4(b) onto the bright-field images in figure 4.4(a) shows that the (002) planes are in the long, thin dark structures seen in the bright-field image. The (002) planes are located in the mineral, so the long dark structures are mineral and will be referred to as *mineral structures* from now on.

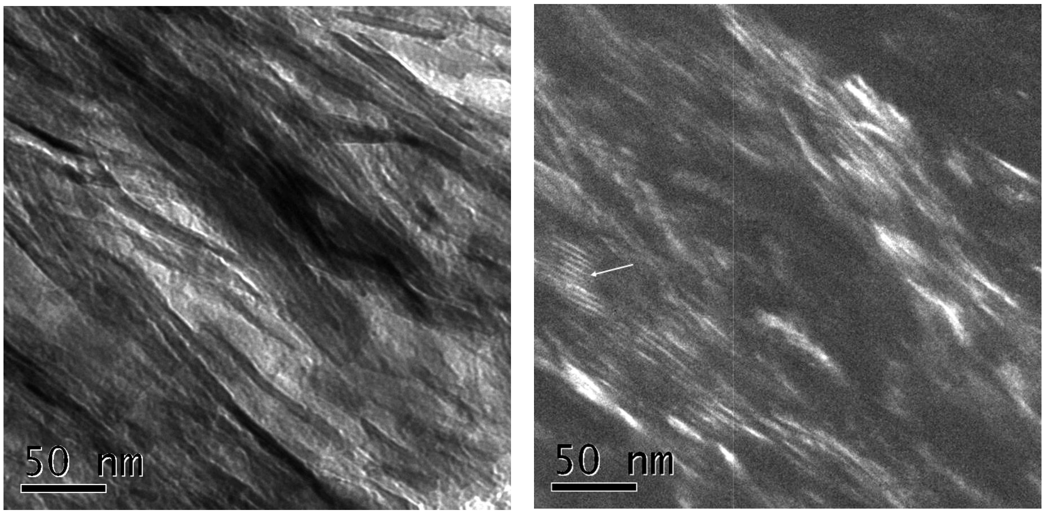

(a) Bright-field image (b) (002) Dark-field image

Figure 4.4: Bright-field and (002) dark-field images of a longitudinal section of human femur. Arrow in 4.4(b) indicates Moiré fringe.

Dark-field images also show further interesting features of the mineral structures. Selecting areas from part of the (211) ring results in illumination of small areas of the structures (figures 4.5). Rotating the objective aperture around the (211) diffraction ring causes areas of the image to illuminate as the (211) planes in that area are aligned suitably for diffraction. Interestingly, the area that lights up moves consecutively along the mineral structures as the selected portion of the diffraction pattern moves around the ring – that is the entire mineral structure does not diffract at the same angle; the crystal structure orientation varies gradually from one end of the structure to the other. This demonstrates why the BF TEM mineral measurements are larger than those by diffraction methods (as shown in section 1.1.3, figure 1.6 and in Eppell *et al.* (2001)).

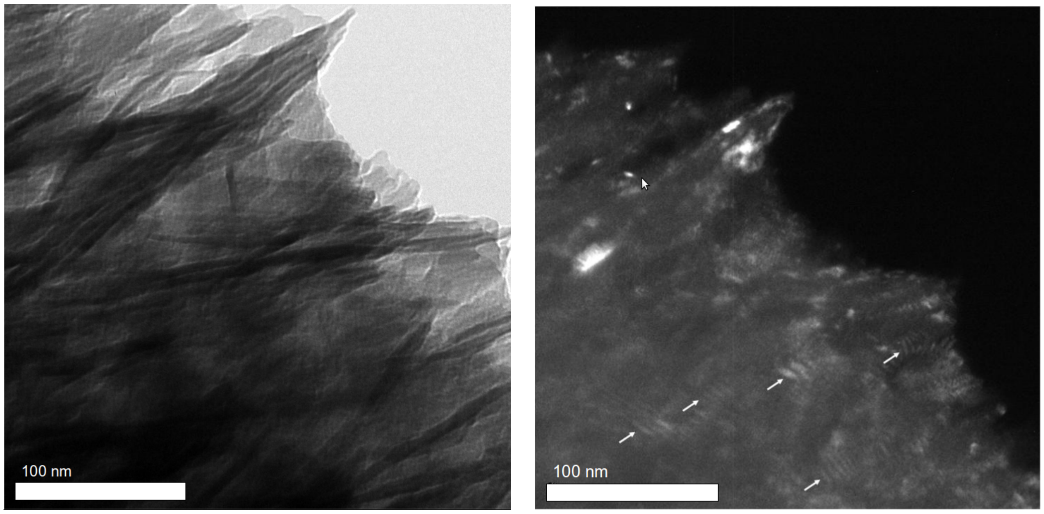

(a) Bright-field image (b) (211) Dark-field image

Figure 4.5: Bright-field and (211) dark-field images of a longitudinal section of human femur cut parallel to the long axis of the bone. Note Moiré fringes indicated by arrows in 4.5(b)

Another feature of the dark-field images are Moiré fringes. These arise from two overlapping but unaligned lattices. It has been proposed that the mineral in bone is in the form of thin plates with one dimension being much smaller than the other two (Robinson & Watson, 1952; Fernandez-Moràn & Engstrom, 1957; Siperko & Landis, 2001; Cressey & Cressey, 2003; Ge *et al.*, 2007; Hong *et al.*, 2009). The presence of Moiré fringes over relatively large areas in the dark-field images with no corresponding features in that area of the bright-field image suggests that samples cut in different orientations as well as different imaging techniques will be needed to fully understand origins of such features. In bright-field imaging, the mass–thickness contrast arising from very thin plates of a material oriented normal to the electron beam is very small when compared to the strong contrast arising from objects with a larger dimension parallel to the electron beam. Dark-field imaging shows this slight contrast because of the reduced number of electrons that are used to form the entire image, as shown in figure 4.4(b) and 4.5(b).

No clear bright zones were identified arising from the gap zones in DF images. Other evidence will be presented that calcium and phosphorous (presumably in the form of HA) is present in these features but for reasons unknown at present, they do not produce coherent scattering of electrons at the Bragg angles expected for HA.

4.5 Energy Dispersive X-Ray Spectroscopy

A second way to confirm the location of the mineral in the longitudinal sections is to do energy dispersive X-ray spectrometry (EDXS). EDXS is performed in STEM mode by collecting an energy spectrum for each pixel of the image allowing the chemical composition of the sample to be mapped. Measurements of the EDXS signal from a longitudinal sample show that the calcium and phosphorus levels are elevated in the mineral structures identified by dark-field imaging, as well as in the gap regions of the collagen banding (4.6). The Ca:P atomic ratio ranges from 1.46:1 to 1.75:1 in both areas which is within an acceptable range around 1.67:1 as expected from the chemical formula for HA, $Ca_5(PO_4)_3OH$. These results will be examined further in chapter 8.

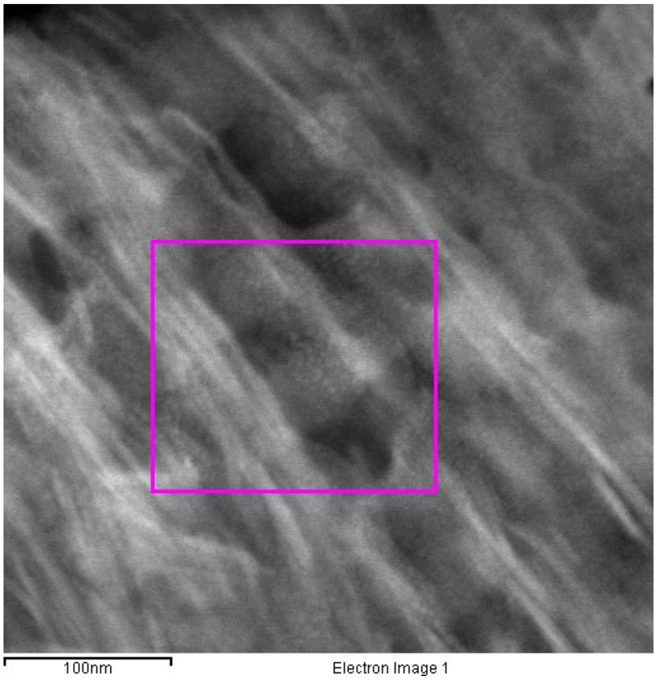

(a) STEM Image

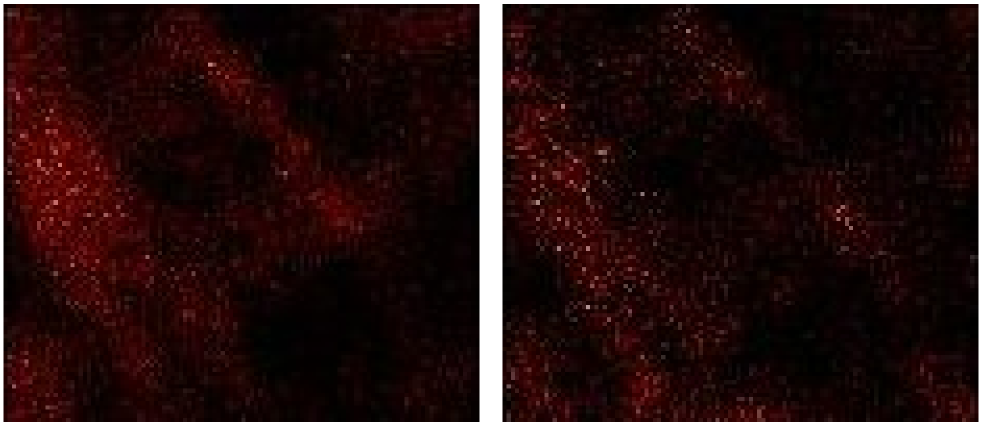

(b) Calcium Counts

(c) Phosphorus Counts

Figure 4.6: Calcium (4.6(b)) and phosphorus (4.6(c)) counts for the area indicated in the STEM image (4.6(a)) of a longitudinal section of human femur. Note the contrast in the STEM image is reversed compared with bright-field images because it is a dark-field technique. The shades of the gap and overlap sections of the banding are reversed and the mineral is white on a black background.

4.6 Mineral Thickness Measurements

From longitudinal structures, two dimensions of the mineral structures can be measured. The narrow dimension parallel to the collagen banding is defined as the thickness while the length is the larger dimension perpendicular to the collagen banding. Measurements of the thickness give a normal single mode distribution with an average of 5 nm and a standard deviation of 1 nm (see appendix A.1 for values). This measurement is in general agreement with literature reports of the thickness of the mineral structures (whether interpreted as plates or needles) in both bone and mineralized tendon (Weiner & Traub (1992); Landis *et al.* (1996b); Fernandez-Moràn & Engstrom (1957); Robinson & Watson (1952); Speckman & Norris (1957); Landis *et al.* (1993); Arsenault & Grynpas (1988); Lees *et al.* (1994)), however it is much thicker than the average of 0.61 nm measured using atomic force microscopy by Eppell *et al.* (2001).

4.7 Mineral Length Measurements

The length of the mineral structures is much more challenging to measure because of the difficulty of finding the ends of the structures in an image. The structures can be seen to be longer than a gap zone unlike what would be expected from the Landis model. In fact, the structures run much longer than one repeat of the 67 nm collagen banding (figure 4.7). Structures up to 200 nm in length have been measured, longer than previously reported in the literature. The majority of reports in the literature range up to 100 nm for the maximum dimension (Robinson & Watson, 1952; Fernandez-Moràn & Engstrom, 1957; Weiner & Traub, 1989; Weiner & Price, 1986; Landis *et al.*, 1993), and between 100 and 150 nm (Speckman & Norris, 1957; Sasaki *et al.*, 2002; Moradian-Oldak *et al.*, 1991), but none ranging into the hundreds of nm. The difference in length can be attributed to the sample preparation technique for TEM measurements and the measurement technique for diffraction measurements. Ion milled sections allow clearer visualization of these structures in fully mineralized bone and greater accuracy in the measurement of their dimensions.

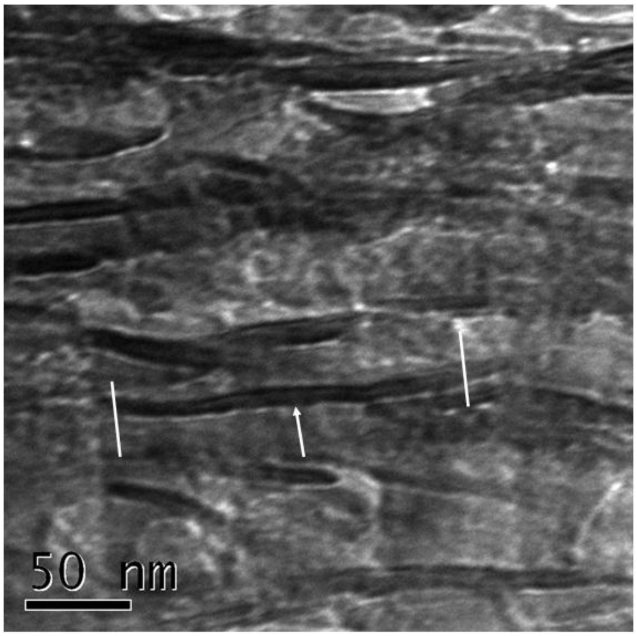

Figure 4.7: Bright-field image of a sample cut parallel to the long axis of a human femur. Indicated mineral structure is 175 nm long.

Other groups have measured the mineral by removing it from the organic matrix by first grinding bone and then exposing it to an agent that dissolves the organic phase (Weiner & Traub, 1989; Eppell *et al.*, 2001). The mineral is then resuspended in a liquid and placed on a grid for TEM examination. The length of these structures has been measured as up to 36 nm (Weiner & Traub, 1989). The mechanical force applied to grind the samples and the forces applied in dissolving the organic matter and removing it in centrifugation could damage the brittle HA structures that are over 40 times longer than they are thick. This damage may explain why lengths measured using these techniques are much less than measurements made of the mineral in situ with a less damaging sample preparation technique.

Diffraction methods like X-ray or neutron diffraction measure the dimensions of the volume that have consistent lattice spacing and direction. If the lattice spacing is not consistent and uniform, the size of the structure is underestimated (see figure 1.6). In the dark-field results it was noted that the bright spot moved along the length of the mineral structure as the selected portion of the diffraction ring was rotated, indicating that the crystal lattice may tilt along the length of the mineral structure. Since the crystal lattice is not uniform for the entire length of the mineral structure, diffraction methods would underestimate their length. If the mineral structures are polycrystalline, another possibility based on the diffraction results, diffraction measurements of the mineral structure sizes will report the length of the individual crystal grains, not the length of the entire polycrystalline mineral structure. Dark-field and X-ray diffraction results consistently report mineral crystal lengths much shorter than the measurements made by bright-field TEM (Fratzl *et al.*, 1996; Ziv & Weiner, 1994; Arsenault, 1989; Arsenault & Grynpas, 1988; Cressey & Cressey, 2003).

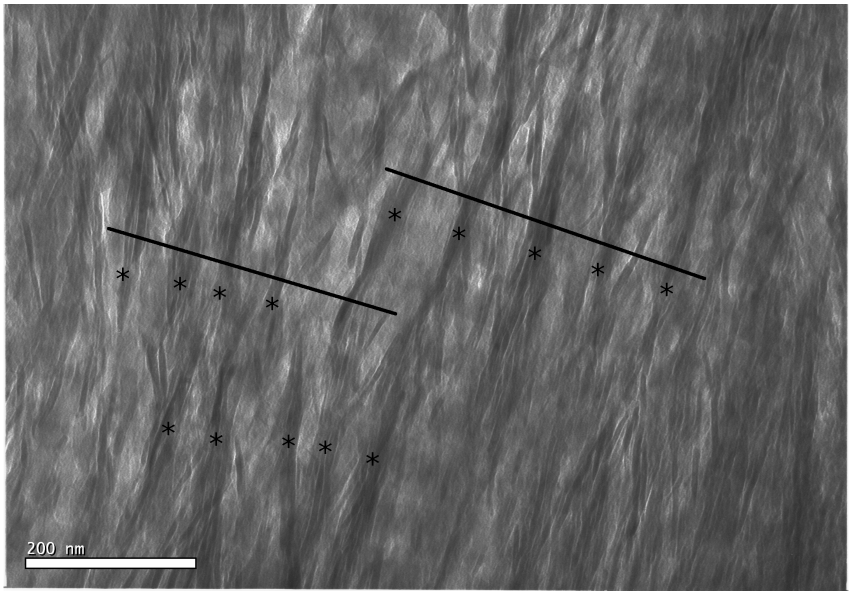

Figure 4.8: Bright-field image of a human femur cut parallel to the long axis of the femur. Clusters of mineral structures form bundles that have been identified by asterisks. Lines indicate location of measurement of bundle spacing.

4.8 Mineral Bundles

Examining the locations of the mineral structures in the longitudinal images reveals another feature that will be of interest during discussion of the perpendicular sections in Chapter 5. The structures are clustered together in bundles running parallel to the collagen fibrils and perpendicular to the collagen banding. These bundles are between four and six structures wide and hundreds of nanometres long (see figure 4.8. The spacing between adjoining bundles averages 53 nm with a standard deviation of 13 nm, while the bundle width averages 22 nm with a standard deviation of 7 nm (refer to appendix A.2 and A.3 for values and calculation). Their significance will be explained in the next chapter.

4.9 Chapter Summary

The longitudinal sections produced by cryogenic ion milling show sharply defined zones of more intense contrast, approximately 40 nm wide, and spaced 67 nm apart. These correspond to the gap zones in collagen widely recognized by others. Also, long dark structures run perpendicular to the banding and much longer than the banding (up to 200 nm) These structures are shown to be mineral and average 5 nm across. The mineral structures appear in 22 nm wide bundles separated by 53 nm gaps in which the collagen banding appears. Dark-field imaging shows Moiré patterns extending over areas of the images with no corresponding features in the bright-field images.

Chapter 5

Perpendicular Sections

5.1 Results

The images from ion milled sections cut perpendicular to the long axis of the femur, as in figure 5.1, are strikingly different than ion milled sections cut parallel to the long section of the bone.

5.2 Bright-Field Images

Ion milled sections cut perpendicular to the long axis of the femur show an open structure not typically seen in the literature (Cressey & Cressey, 2003; Jantou

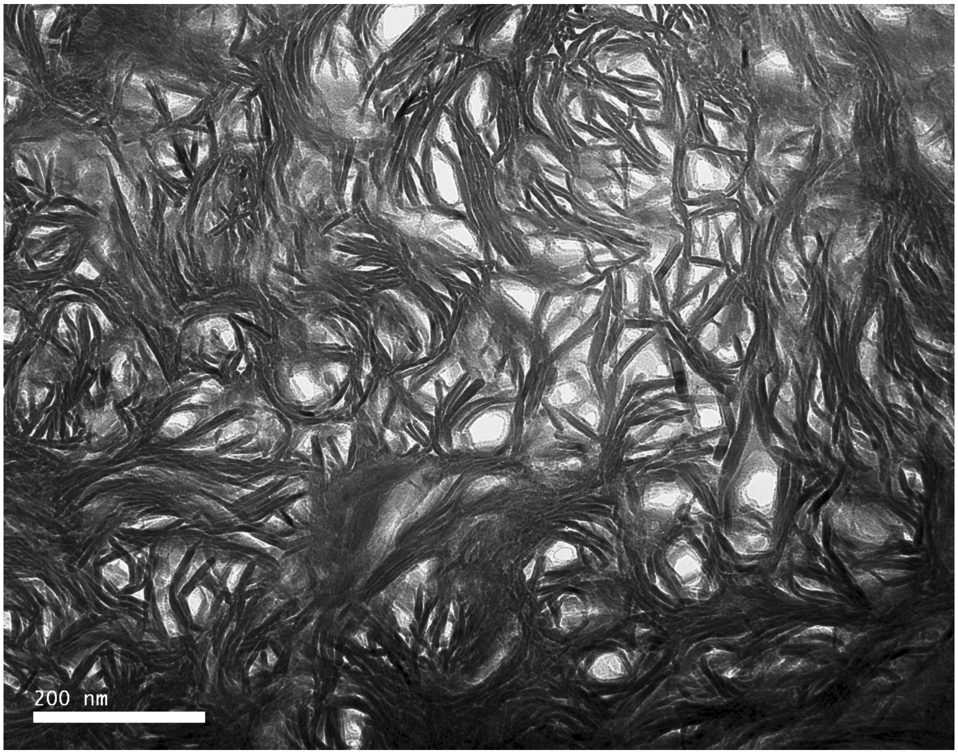

Figure 5.1: Bright-field image of an ion milled sample of cortical human femur cut perpendicular to the long axis of the bone. Note the mineral structures are tangential to the open areas, but that there is no uniform orientation of the mineral structures across the image.

et al., 2009). Rarely are the collagen banding or the parallel mineral structures of the longitudinal sections visible (figure 5.2). In the areas without collagen banding in the perpendicular sections, the dark structures have no overall preferred orientation, although mineral structures located next to each other often have a mutually parallel orientation. Analysis of the orientation confirms the randomness of the dark structure orientation over the image with a significance level (p-value) of 0.05 (see appendix A.9 for an explanation of the randomness test and the data used). These randomly oriented structures tangentially surround areas with little to no contrast, creating a lacy fabric of apparently open areas surrounded by dark

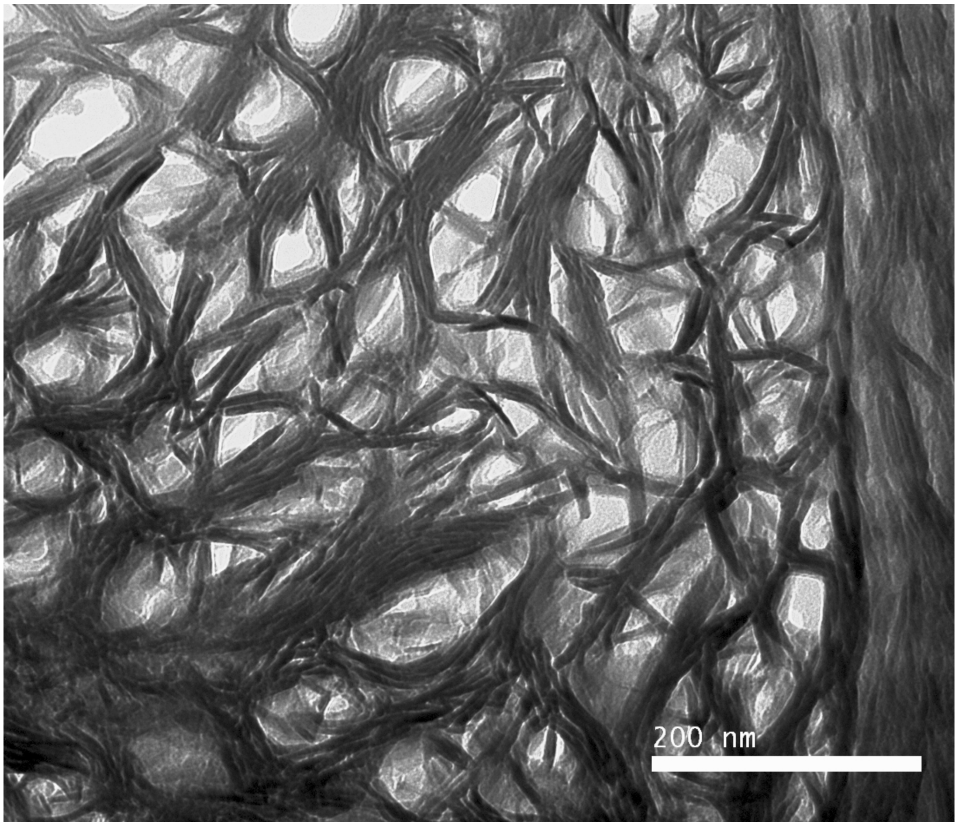

Figure 5.2: Bright-field image of an ion milled sample of cortical human femur cut perpendicular to the long axis of the bone. This image illustrates the presence of both areas similar to the longitudinal sections and the open lacy structure of perpendicular sections.

structures. Similar patterns are seen in images obtained on ion-milled sections by Cressey & Cressey (2003), as shown in figure 1.12.

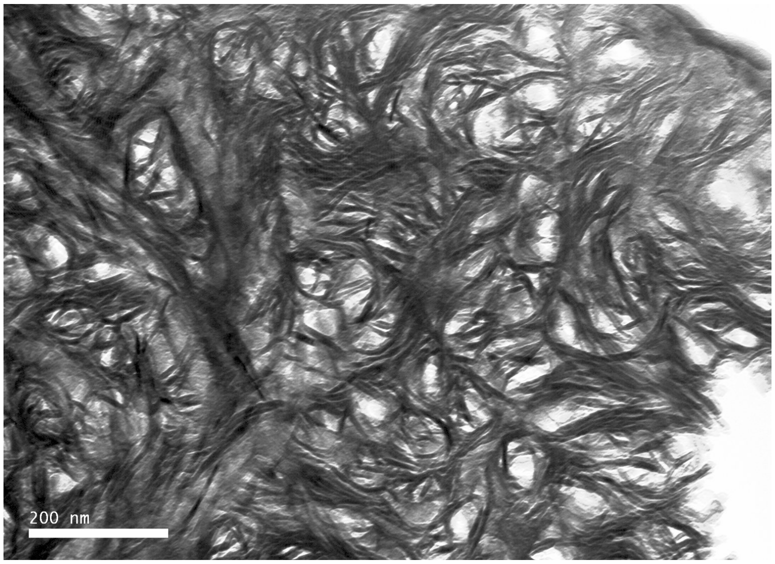

(a) Bright-field Image

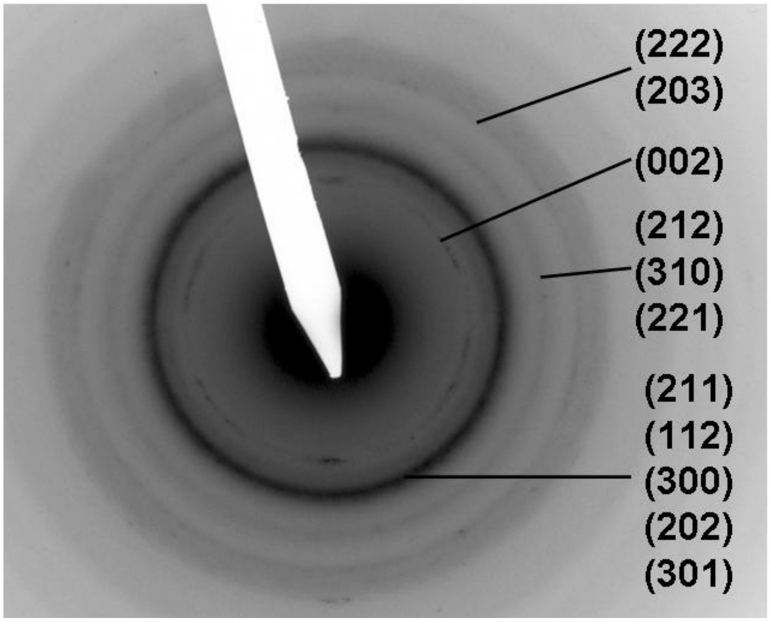

(b) SAD Pattern

Figure 5.3: Bright-field and SAD pattern of an area centred on the bright-field image of an ion milled sample cut perpendicular to the long axis of a human femur. Diffraction pattern is rotated to match orientation of image and is indexed to hydroxyapatite using JCPDS 09-0432. Note (002) reflections in many directions, compared with the (002) arcs of the longitudinal section diffraction pattern (figure 4.3).

5.3 Diffraction Patterns

Hydroxyapatite (HA) has a characteristic diffraction pattern (JCPDS 09-0432), and the selected area diffraction (SAD) pattern for these samples matches the known HA pattern (figure 5.3) demonstrating that the mineral in these samples is HA. The diffraction pattern also confirms the overall randomness of the mineral orientation in these cross-sectioned samples. Unlike the longitudinal sections, where the (002) reflections in the selected area diffraction patterns form short arcs, the (002) reflections for the perpendicular section are weak and randomly oriented around the central beam, with some brighter spots. This randomness shows that there is no preferred direction for the (002) axes in these samples and the weakness shows that few crystals are oriented with the (002) direction in the plane of the sample.

5.4 Measurements

Measurements of the structures in these images give a thickness of 5 nm with a standard deviation of 1 nm (see appendix A.4 for details). Thickness is the dimension that is shown in its full extent in both longitudinal and perpendicular sections, so it can be used as a test to ensure that the same mineral structures are being measured in the two very different motifs of the longitudinal and perpendicular sections. Comparison of the two sets of thickness measurements from the longitudinal and perpendicular samples using a Students' t-test shows that the two sets of measurements are from the same distribution with $p = 0.05$ (see appendix A.5. This test suggests that the same mineral structures are being imaged in both sets of images. As shown previously, this thickness is within the range reported for mineral thickness by other groups (Weiner & Traub, 1992; Landis *et al.*, 1996b; Fernandez-Moràn & Engstrom, 1957; Robinson & Watson, 1952; Speckman & Norris, 1957; Landis *et al.*, 1993; Arsenault & Grynpas, 1988; Lees *et al.*, 1994).

The width of the structures in the perpendicular sections is 68 nm with a standard deviation of 19 nm (see appendix A.6). This dimension could not be measured in the longitudinal sections, just as the length can not be measured in the perpendicular sections. This width is comparable with measurements of the smaller dimension normal to the thickness of isolated crystals removed from the matrix and also in some TEM images by other researchers (Lees *et al.*, 1994; Landis *et al.*, 1993; Fernandez-Moràn & Engstrom, 1957; Robinson & Watson, 1952).

Another measurement made on the cross section images is the width of the open, less electron dense areas. The open areas are irregularly shaped, but roughly round. They average 45 nm with a standard deviation of 23 nm in diameter (see appendix A.7). This diameter corresponds well to the 50 nm diameter of native type I collagen fibrils prepared in solution (Ramachandran, 1967) and to measurements of collagen fibril diameter in bone of other species (Tzaphilidou, 2005), suggesting that the open areas are the locations of the collagen fibrils in the sample. The collagen is unstained, has low atomic number atoms and no crystallinity so the holes appear to be unfilled in these images. The oval shape of some structures is likely due to sectioning the collagen fibril at an angle that is not perfectly perpendicular to its long axis and imaging the section with the electron beam not perfectly parallel to the collagen axis. This effect leads to the large standard deviation of the data.

5.5 Nanostructure of Cortical Bone

The perpendicular section measurements combined with those made on the long section images indicate that a large portion of the mineral in fully dense cortical bone is in the form of plates, approximately 5 nm thick, 65 nm wide, and greater than 200 nm long. These mineral plates, called mineral structures, surround openings 45 nm in diameter where the collagen fibrils are located. See figure 5.4 for a sketch of this model.

The contrast arising from face on mineral structures will be minimal compared with that from the edge on structures. As a result, in both longitudinal and perpendicular sections, only the structures oriented edge on with respect to the plane of the section are visible in micrographs. In the perpendicular sections, mineral can be seen tangentially surrounding the cross sectioned collagen fibrils. The bundles noted on the longitudinal section in figure 4.1 of chapter 4 are edge on views of the mineral structures lying in the zone between two collagen fibrils. These two features are the same structure of tightly packed mineral between the collagen fibrils visualised from different directions.

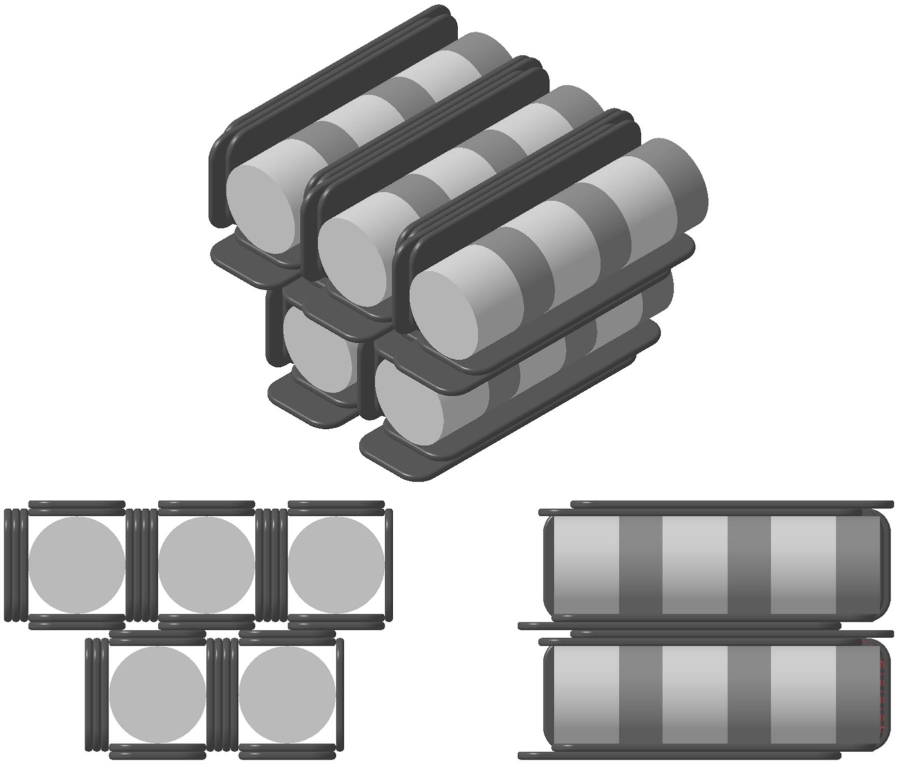

Figure 5.4: A simplified model of the external mineral in bone structure. 45 nm diameter collagen fibrils are surrounded by 200 nm long, 65 nm wide, 5 nm thick plates of mineral. The top image shows the model in an isometric view. The bottom left shows the model projected down the fibril long axis, as if it were a perpendicular section. The bottom right shows the model projected across the collagen fibrils, as if it were a longitudinal section.

In the perpendicular sections, the viewing direction is down the collagen fibril, while in the longitudinal sections, the collagen fibrils lie in the plane of the section. In both cases, the mineral can be seen only if one of the larger dimensions (length or width) are oriented perpendicular to the sample plane. If mineral is viewed edge or end on it is seen in the image as a dark line, while if it is viewed face on, the scattered intensity it creates will be too weak to create enough contrast to be visualised in BF microscopy. Overlapping plates lying face on will generate Moiré fringes that can be seen in dark-field images of longitudinal sections (figure 4.5(b)).

This model with external mineral is similar to the suggestion by Ge et al (Ge *et al.*, 2007), but in their work with zebrafish they find coarser structures ($\sim$150 nm spacing of stripes vs. 52 nm in this work). They model the mineral surrounding the fibril as a cylinder, not discrete plates. Sasaki et al. envision a similar structure based on their AFM studies of bovine cortical bone (figure 1.11) but the collagen fibril diameter they infer is 110 nm in diameter while the mineral 'crust' completely surrounding the fibril is 10 to 20 nm thick. In some respects this model resembles the proposed interpretation of the cross sectioned TEM images but our TEM images show the crust is assembled from many plates instead of one solid piece of mineral.

5.6 Chapter Summary

Samples cut perpendicularly to the long axis of the femur show a open motif not seen frequently in the literature. 50 nm open areas are tangentially surrounded by 5 nm thick, 65 nm long mineral structures. From these data and the longitudinal sections a ing emerges where the extra-fibrillar mineral in cortical bone is in the form of 5 nm thick, 65 nm wide, 200 nm long mineral structures tangentially surrounding 50 nm diameter collagen fibrils. There is no alignment of the mineral structures in the cross sectioned samples, unlike in the longitudinal sections. This model explains two features found in the longitudinal sections. First, the bundles are interpreted as the areas between collagen fibrils where the mineral structures are viewed edge on. Second, the Moiré patterns observed in dark-field images of longitudinal sections are now interpreted as areas where overlapping mineral structures are viewed face on. In bright-field images of longitudinal sections, the face on mineral structures cannot be seen as the contrast arising from the 5 nm beam path length is much less than contrast arising from the 65 nm beam path length of edge on structures. This external mineral model is similar to that proposed by Ge et al. and Sasaki et al. using TEM and AFM on zebrafish and bovine bone respectively (Sasaki *et al.*, 2002; Ge *et al.*, 2007).

Chapter 6

Discussion of Sample Preparation Techniques

6.1 Ion Milling

Images of ion milled samples of dense cortical bone cut parallel to the long axis of the femur strongly resemble images of samples of MTLT, cortical and embryonic bone cut in the same direction by ultramicrotoming. Images of samples of dense cortical bone cut perpendicular to the long axis do not resemble corresponding images of ultramicrotomed samples of MTLT, cortical and embryonic bone. To confirm that the open structure seen in the perpendicular section images is not an artefact of sample preparation, an ion milled sample cut at 45 degrees to the long axis of the human femur was prepared. This sample orientation is intermediate between the longitudinal and perpendicular sections and should therefore show, by tilting, both types of images if the ion milling is not damaging the sample.

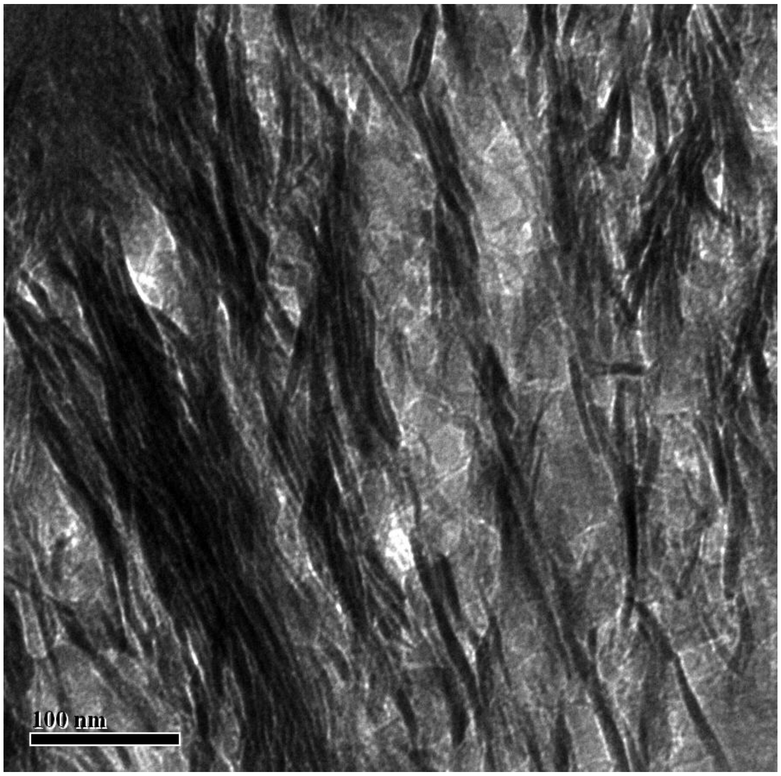

Figure 6.1: 45 Degree human section tilted to -45°. This orientation shows the structure typical of longitudinal sections. The collagen banding is indistinct.

After tilting to -45° so that the electron beam is perpendicular to the long axis of the femur, the resulting image is similar to that of the longitudinal sections (figure 6.1). The microscope goniometer did not allow tilting the sample to an angle where the collagen banding could be seen (as described in section 4.2 and figure 4.2); however, it is expected that it would be present if the microscope permitted a higher tilt angle. Tilting to +45°, such that the sample/beam orientation mimics orientation of the perpendicular section, shows the open structure characteristic of the ion milled perpendicular sectioned samples (figure 6.2). The presence of both structures in one sample confirms that the ion milling process has not created the lacy fabric of the perpendicular sectioned images. If the sample had been damaged during ion milling, orienting the sample to mimic a longitudinal section would not show the structure reported in the literature.

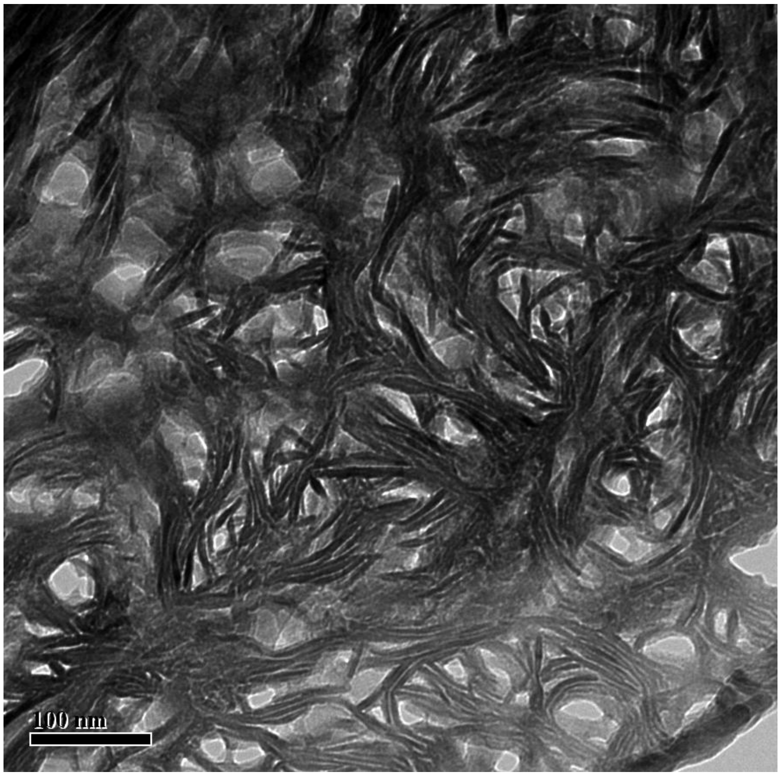

Figure 6.2: 45 Degree human section tilted to +45°. This orientation shows the structure typical of perpendicular sections.

6.2 Ultramicrotoming

Comparison of images obtained by ion milling in this study with analogous published images of sections of ultramicrotomed fully mineralized cortical bone raises concern about the use of ultramicrotoming to create samples of mineralized tissues. The two major components of bone have widely varying mechanical properties and the bending forces applied during ultramicrotoming could severely damage the structure, particularly that of HA, the comparatively brittle material (Boyde & Pawley, 1976).

To assess these concerns, samples of the cortical bone of bovine femurs were ultramicrotomed by Marcia Reid, an experienced technician in the Hamilton Health Sciences Electron Microscopy laboratory, as discussed in the section 3.1.9. Samples were prepared in both the parallel and perpendicular orientation relative to the long axis of the femur. Bright-field images of the ultramicrotomed samples were prepared for comparison with images prepared from ion milled samples and with images presented in the literature for ultramicrotomed samples.

A characteristic image of an ultramicrotomed sample cut parallel to the long axis of the femur is shown in figure 6.3. In this image, the collagen banding is not present, the mineral is aligned locally, but no alignment over the whole image is seen. The mineral structures average 37 nm long with a standard deviation of 12 nm (see appendix A.10). A sample of bovine femur cut parallel to the long axis of the bone was ion milled, and a representative image can be seen in image 6.4. The ion milled sample is clearer, shows the collagen banding running from upper

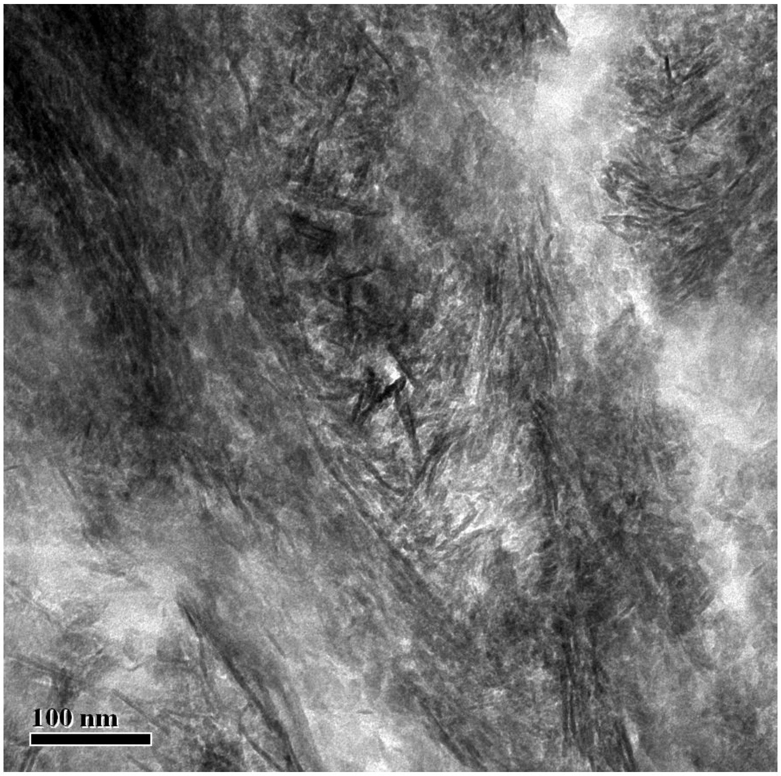

Figure 6.3: Ultramicrotomed bovine femur cut parallel to the long axis of the femur.

left to lower right, with the mineral running perpendicular to the collagen bending. The mineral structures average 77 nm long with a standard deviation of 32 nm (see appendix A.11). The length of the ion milled mineral structures averages twice that of the ultramicrotomed mineral structures.

An image of an ultramicrotomed sample of bovine femur cut perpendicular to the long axis of the bone is shown in figure 6.5. This image is characteristic of the sample. The open structure widely visible in ion milled perpendicular sections (see figure 6.6) does not appear in these samples. Figure 6.7 shows an area in the ultramicrotomed section with more order, but the order resembles that of a

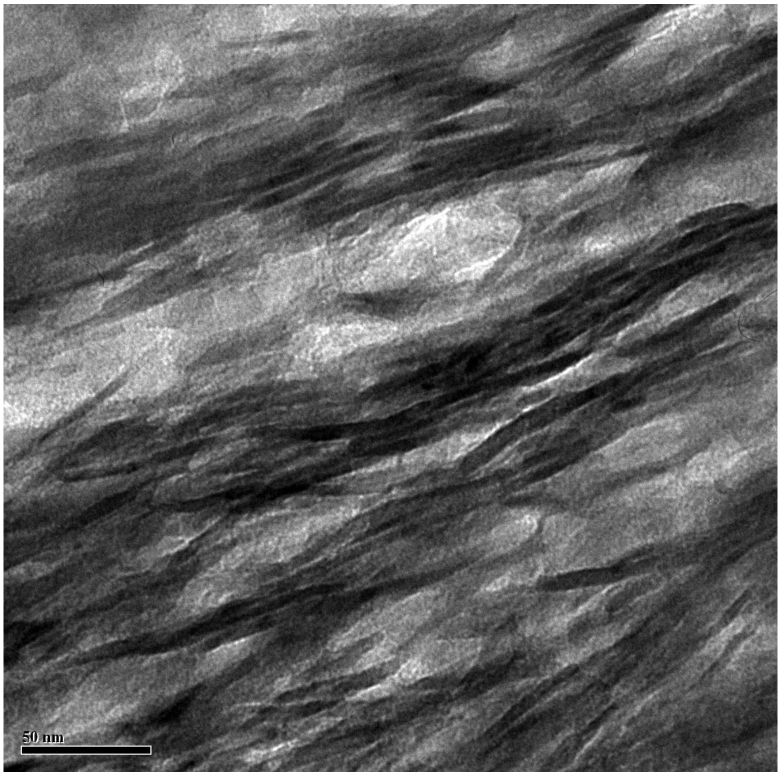

Figure 6.4: Ion milled bovine femur cut parallel to the long axis of the bone. Overall collagen banding runs from upper left to lower right, mineral structures are roughly aligned perpendicular to the banding.

longitudinal section and the open structure is not evident. Again, the average mineral structures' long dimension in the ion milled samples, the width in this image, is double the same dimension in the ultramicrotomed sample (see appendices A.12 and A.13).

If the sample is able to withstand significant bending without damage, ultramicrotoming is an appropriate technique for sample preparation. Most biological samples are therefore suitable for ultramicrotoming. To improve the

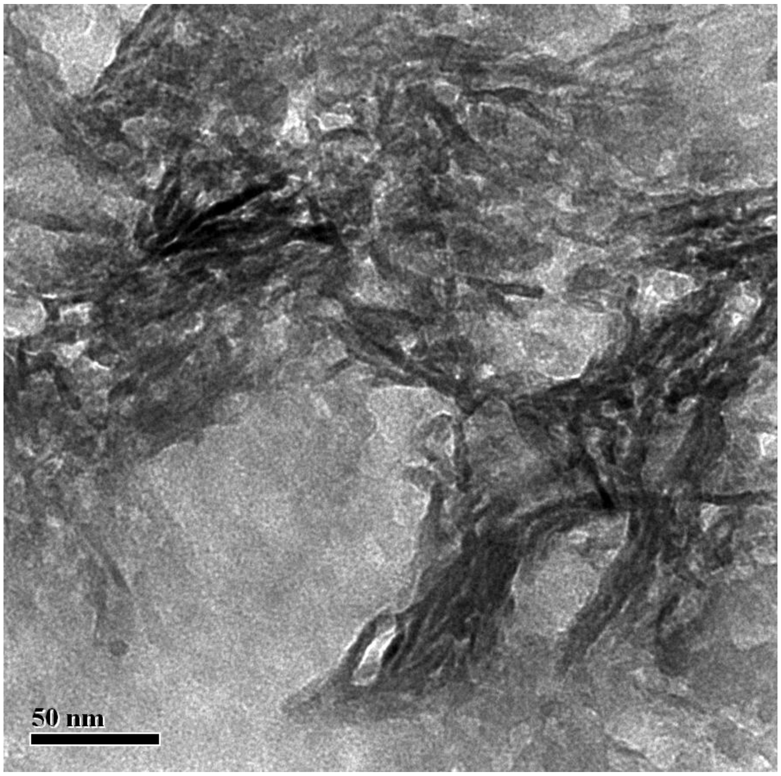

Figure 6.5: Ultramicrotomed bovine femur cut perpendicular to the long axis of the bone. Note areas of order and disorder and absence of open lacy structure.

ultramicrotome results, biological samples are often embedded in a polymer to stabilize the structure. Bone is a composite biological material. One part of the composite, collagen, is a traditionally ultramicrotomed biological material. HA is a crystalline material with low flexibility and high stiffness. While collagen may withstand the bending and shear forces applied during ultramicrotoming, HA may shatter, creating artefacts (Volkert *et al.*, 2004).

The low flexibility and high stiffness of HA explains why the ion milled sections in this work show the mineral plates being much longer than previously reported

Figure 6.6: Ion milled bovine femur cut parallel to the long axis. The open structure is preserved by ion milling.

(200nm here vs 80 nm with ultramicrotome (Landis *et al.*, 1996b)). The plates are more than 40 times longer than they are thick. Bending this structure through the 45 degrees imposed by the diamond knife causes it to fracture. Ion milled sections of dentine, an analogue of bone, also show mineral structures 40 times longer than they are thick (Boyde & Pawley, 1976).

Ultramicrotome damage may have led to several incorrect conclusions about the location and orientation of the mineral within a fibril and a section in bone. Several groups describe the mineral inside fibrils being in a parallel alignment (Weiner & Traub, 1986, 1992). From our ultramicrotomed images it is clear that

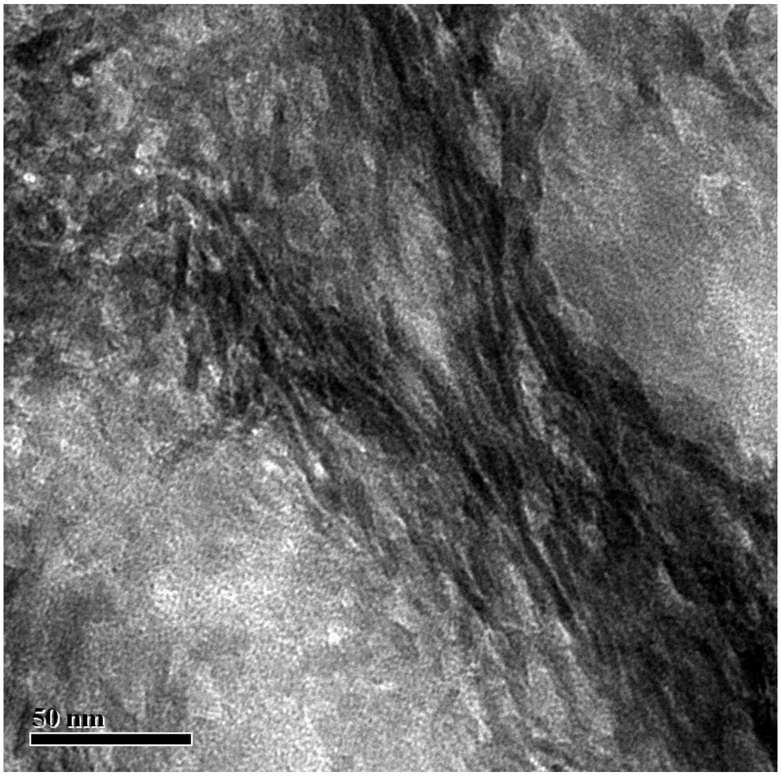

Figure 6.7: Ordered area in ultramicrotomed bovine femur sample cut perpendicular to long axis of the femur.

the open structure is degraded by ultramicrotoming and the small areas with parallel structures are relatively undamaged. The images led other researchers to infer that the mineral structures lie parallel to each other and to the collagen long axis in both the longitudinal and perpendicular sections as shown in figure 1.9. In addition, the absence of open areas to house the collagen fibrils would lead to the conclusion that the crystalline mineral is located inside the fibrils.

6.3 Note on the Comparison of Human and Bovine Samples

As this work required the preparation of samples of the cortical bone of bovine femurs, it is noted that the images prepared from these samples and measurements from the images correspond well with the images and measurements made on human bone. It is speculated that the three-dimensional structure developed in chapter 5 is a common motif found in mammalian bone.

6.4 Mineralizing Turkey Leg Tendon

An additional concern about sample preparation is the samples themselves. A significant portion of the literature about the nanostructure of bone uses mineralizing turkey leg tendon (MTLT) as a model for bone nanostructure. MTLT differs from bone in several ways. First, the maximum mineralization level in MTLT is 15 volume % while bone achieves 40 to 45 volume % mineralization (Jager & Fratzl, 2000). The difference in mineralization level means that the final structure in MTLT is not as dense as bone and some locations within the collagen framework may not be mineralized. Second, in MTLT the mineralized collagen fibrils are close–packed with very little space or mineral between them (Weiner & Traub, 1986), while bone has mineral both inside and outside the fibrils (Landis & Song, 1991; Landis *et al.*, 1996a; Prostak & Lees, 1996). The collagen fibril diameter in MTLT is several hundred nm (Lees *et al.*, 1994), while the fibril diameter in rabbit, mouse, and rat bones is 63, 46, and 48 nm respectively (Tzaphilidou, 2005). A larger fibril diameter allows the ratio of intra- and extrafibrillar mineral to be weighted towards the intrafibrillar locations. Finally, bone is loaded in compression in the body while MTLT is loaded in tension. In ceramic materials, the tensile strength is a tenth of the compressive strength (Callister, 2006). HA is a ceramic and the variation in loading type means its contribution to the mechanical properties of MTLT will be very different from that in bone. It is also possible that tissue loaded differently will develop different structures. For instance, mesenchymal cells that will form cartilage when loaded hydrostatically will differentiate to form bone when they are loaded uniaxially or biaxally (Pelttari *et al.*, 2008; Wagner *et al.*, 2008; Jung *et al.*, 2009). MTLT was used because it is easily ultramicrotomed and because it shows a gradient in mineralization level; however, from the work using ion milling, it is seen that open structures in the perpendicular sections will be damaged by ultramicrotoming.

6.5 Chapter Summary

A sample cut at 45 degrees to the long axis of the femur, then cryogenically ion milled shows that the ion milling process does not create the open texture seen in the cross sectioned samples. When the 45 degree sample is tilted so the electron beam is perpendicular to the collagen fibrils, the micrograph resembles that of a longitudinal section. When the 45 degree section is tilted so the electron beam is parallel to the collagen fibrils, the structure is that of the perpendicular sections.

If the cryogenic ion milling process were damaging the sample, the two structures would not be present in the same sample.

A piece of bovine bone was used to compare the size of the mineral structures in ultramicrotomed and cryogenically ion milled samples. The mineral sections in the ion milled sections cut parallel to the long axis of the femur are twice the length of mineral sections in ultramicrotomed samples cut in the same orientation. Ultramicrotomed samples cut perpendicular to the long axis of the bone do not show the open structure of the cryogenically ion milled samples. Again, the mineral structures in the ultramicrotomed samples are half the length of the cryogenically ion milled samples. The deformation imposed by the slicing process of ultramicrotomy makes it an inappropriate sample preparation technique for bone samples. The images of bovine samples strongly resemble those of cortical human bone and the feature measurements are similar, indicating that the structure of human and bovine bone is similar and that this structure may be conserved across the mammalian class.

Chapter 7

Tomography

Traditional TEM and STEM imaging create projections of a three-dimensional structure on a two dimensional image plane. To fully understand the three-dimensional nature of a structure, tomographic imaging is used. The goal in this work is to create a three-dimensional model of the structure to confirm how the two very different types of images resulting from the longitudinal and perpendicular sections come from the same material. The technique uses a series of images at very small tilt steps relative to each other and then mathematically reconstructs the three-dimensional structure that created the projections.

Previously, Landis et al. (Landis *et al.*, 1993, 1996b) used high voltage (HVEM) electron tomography on 250 nm thick samples of MTLT and embryonic bone. Tomographic reconstruction requires a monotonic relationship between the contrast and the amount of material the beam passes through (Midgley & Weyland, 2003). The HVEM tomography technique relies on TEM bright-field images, with the majority of contrast assumed to be mass–thickness contrast. In the case of most biological samples, with minimal crystallinity, this would be true. However, the mineral in bone is highly crystalline, resulting in diffraction contrast dominating over mass–thickness contrast. The contributions of diffraction contrast to the image would vary with the orientation of the crystals as the sample is tilted during the tilt series collection. At angles where the planes are aligned properly for diffraction, the contrast would be high, while nearby angles that do not satisfy diffraction conditions would have much less contrast and the diffraction component of the total contrast would be lower. TEM BF images of bone and mineralized tendon are therefore not monotonic and are unsuited to tomographic reconstruction. Midgley and Weyland showed that the use of Z contrast HAADF STEM imaging in these situations forms projections with the required monotonic relationship between contrast and thickness, allowing tomographic reconstruction of the dataset (Midgley & Weyland, 2003). Recent advances in STEM technology allow nanometre resolution in HAADF STEM images, resulting in DF tomography becoming a viable technique. With this knowledge, HAADF STEM imaging was used to prepare tomographic datasets on three samples of ion milled cortical bone from the femur of a 60 year old human male: cut perpendicular, parallel and at 45 degrees to the long axis of the femur.

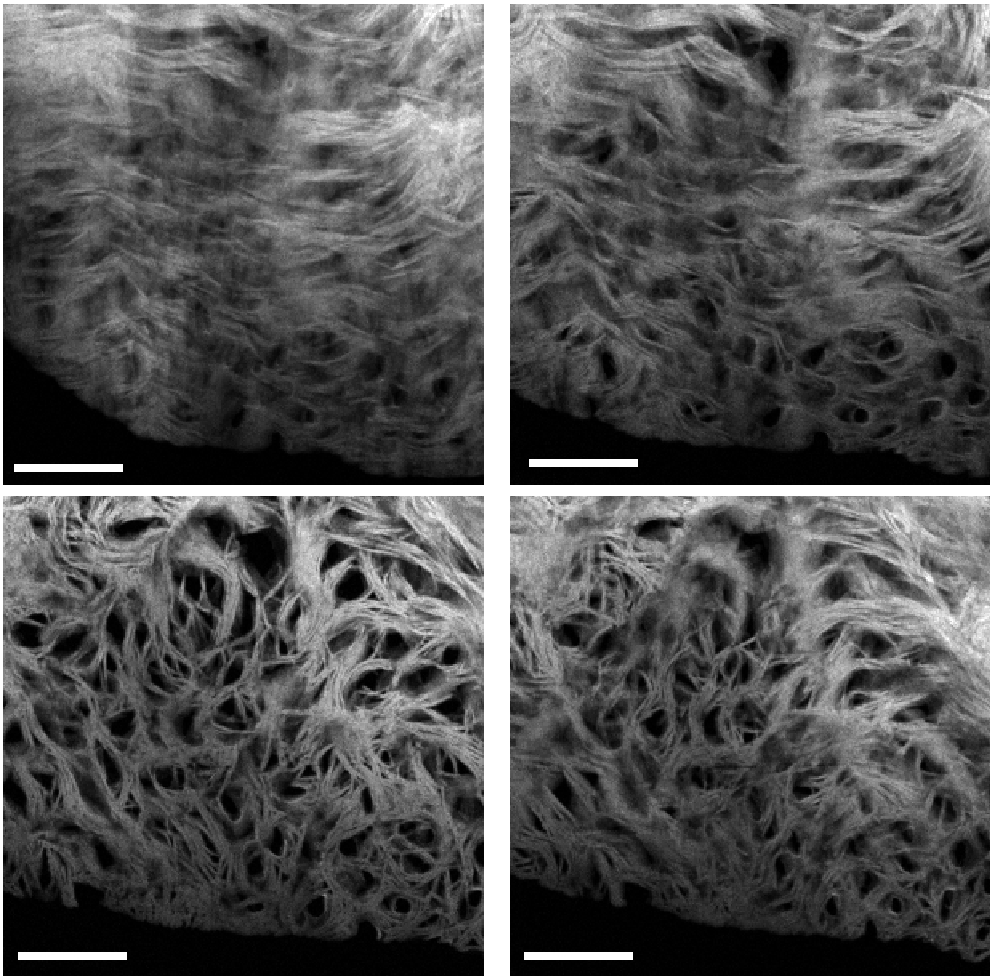

Figure 7.1: Images from the tilt series of a perpendicular section of human cortical bone. Top row, -44° and -24° tilt, Bottom row, 24° and 46° tilt. Bar is 200 nm and the tilt axis is vertical.

7.1 Tilt Series

The first step in tomography is to collect the data. The dataset is images of the sample taken over a wide range of tilt angles. Three datasets were collected, one for each of the three sections. For the longitudinal section, the tilt series was collected from -75 to +75°. The perpendicular section had data from -76 to 76°, while the

45 degree section had -65 to 72° data. The variation in the collection angle was determined by variations in the sample around the area of interest. Data was only collected at angles where the resulting image had useful information. At angles higher than those collected the sample was too thick or the area of interest was shadowed by another portion of the sample, causing the image to contain no useful information.

A series of selected images from the tilt series of the perpendicular section is seen in figure 7.1. These images confirm that the mineral structures are in the form of plates. Figure 7.2 shows two images of the same mineral structure taken 16° apart. In figure 7.2(a) the mineral structure is seen edge on, while in figure 7.2(b) the same mineral structure is seen to be a plate widening out at this angle. The mineral structures measure approximately 5 nm across, in agreement with the measurements made in the bright-field images earlier.

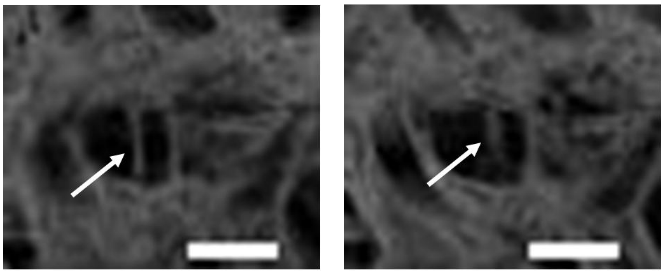

(a) 38 degree tilt

(b) 22 degree tilt

Figure 7.2: Image of the same area of the sample viewed 16° apart. Note indicated mineral structure changing from edge on view in 7.2(a) to wider in 7.2(b). Bar is 50 nm long and the tilt axis is vertical.

A comparison of figures 7.2(a) and 7.2(b) shows that the contrast from the mineral structure changes with the tilt. This is expected because when the mineral structure is viewed edge on, it is viewed down the width or length, both of which are at least ten times larger than the thickness. As the sample is tilted towards being face on, the beam path length through the sample shortens and the resulting contrast decreases. Because the images were recorded with HAADF STEM, the contrast is caused by Z-contrast imaging, not diffraction, so the monotonic requirement for contrast to perform tomographic reconstruction is satisfied. The contrast in HAADF STEM images is dependent on the atomic number of the atoms present in the material and their quantity. Volumes with high concentrations of the heavier calcium and phosphorus atoms are visualized, while collagen, composed of low atomic number elements, mainly carbon, nitrogen, oxygen and hydrogen, does not create contrast in the images. Note that the images created in HAADF STEM imaging are dark-field images: bright areas represent the location of the mineral.

7.2 Reconstruction and Initial Visualization

Reconstruction of the volume imaged by the tomographic tilt series was performed using the simultaneous iterative reconstruction technique. The result is a volume of voxels (three-dimensional pixels) with each voxel having a density resulting from the calculation of the structure. Visualization of the voxels is an initial way to view the reconstruction. Mapping the voxel density onto a colour scale creates a voltex representation of the reconstructed volume. In figure 7.3 low density voxels are represented by blue while high density voxels are yellow and densities in between are colours between blue and yellow. All figures of tomographic reconstructions do not have scale bars because they are screen captures of three-dimensional structures. The size of the reconstructed area is given in the figure caption.

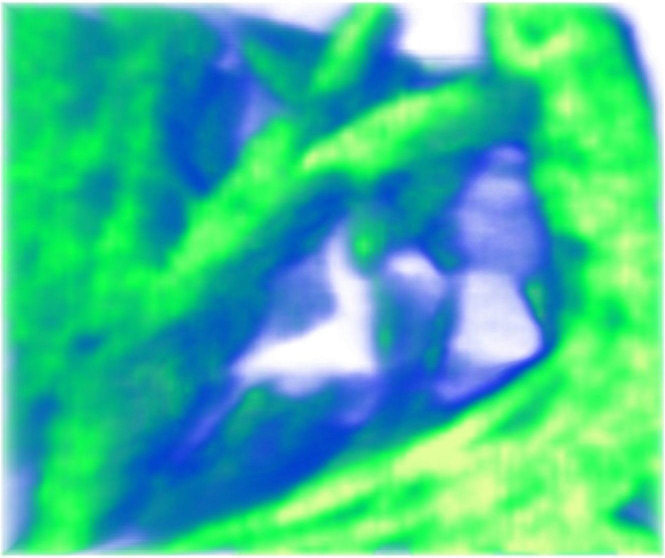

Figure 7.3: Images of a voltex representation of the reconstructed volume created from the tilt series prepared from a perpendicular section. Voxels are represented from blue (low density) to yellow (high density). The reconstructed volume is 130 nm wide, 110 nm high and 70 nm deep

Figure 7.3 shows the reconstruction has created a volume with varying density, as expected. The volume contains long thin dense areas surrounding a tunnel through the volume. This tunnel can be better visualized using the video file titled Perpendicular Section Voxel Visualization on the included DVD.

To examine the dataset in more detail, orthoslices through the dataset are visualized. The orthoslices show the varying density in a one voxel thick slice of the volume. Figures 7.4 and 7.5 show two orthogonal views of the perpendicular dataset. Figure 7.4 shows a hole approximately 65 by 40 nm in area tangentially surrounded by dense 5 nm wide features. This image resembles the structure seen in the perpendicular bright-field images, but with reversed contrast. The main difference is the smaller number of discrete mineral structures visible. This lower number is because the image is one voxel thick, not a projection of a thick structure; only the mineral structures that cross this plane in the volume are shown. In the bright-field image, the mineral structures throughout the volume are projected onto the image plane.

Figure 7.5 shows an orthoslice cut perpendicular to the orthoslice shown in figure 7.4. The orthoslice displays roughly aligned 5 nm wide lines running from the top to the bottom of the slice (see appendix B for a discussion of resolution in tomographic reconstructions). This image resembles the parallel section images, which is expected since it is orthogonal to the open structure of the cross section image. In the middle of figure 7.5 is an area of very low density which presumably represents where this one voxel thick slice cuts through a collagen fibril. The lack of density emphasizes the much lower mineral density inside the collagen fibril. This sample is thick enough to have one full 67 nm repeat of the collagen banding, but despite being expected, it does not appear in this region. In all of the reconstructions, the interior of the fibrils appears to be devoid of mineral content, despite the presence of collagen banding in the tilt series.

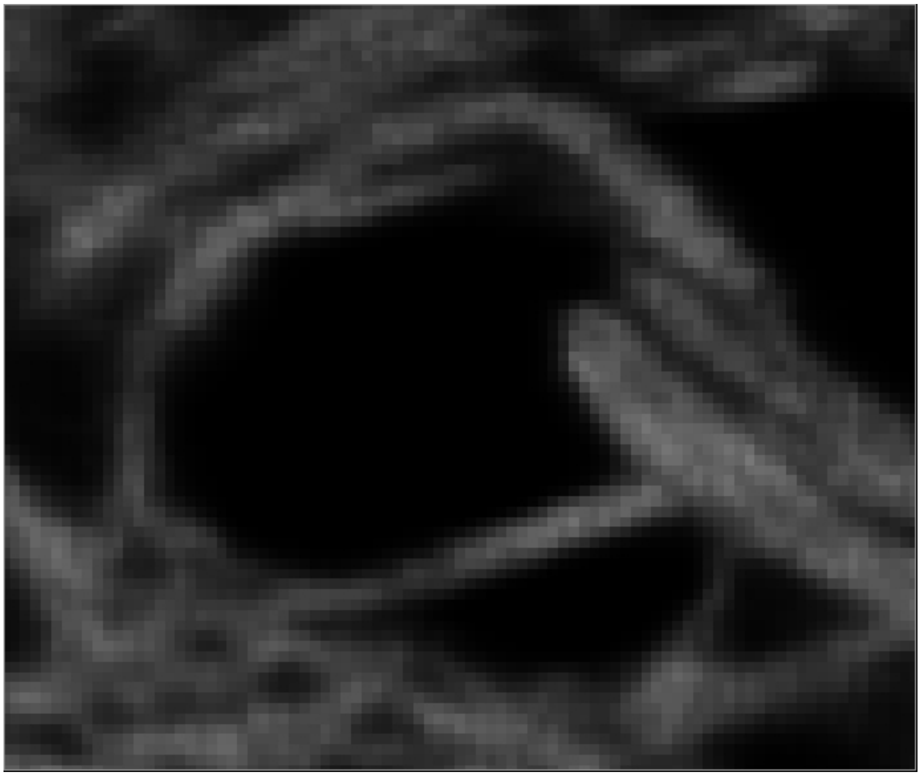

Figure 7.4: XY orthoslice of a reconstruction from the perpendicular tilt series. The slice is in the middle of the reconstructed volume. The collagen fibrils are oriented approximately normal to the page in this slice. The open area is approximately 65 by 40 nm and is the same open area seen in figure 7.3 . The dimensions of the visualized area are 130 nm across and 110 nm high

7.3 Segmentation of Tomographic Reconstruction

In order to convert the voltex images into more realistic views of the distribution of mineral-rich volumes in bone, a procedure called segmentation was employed. This procedure converts the diffuse boundaries of voltex representations (figure 7.3) to sharply defined edges which are intended to show the external surfaces of the mineral structures. An edge to the structures is defined selecting a minimum greyscale level that will determine the voxels that lie inside and outside the

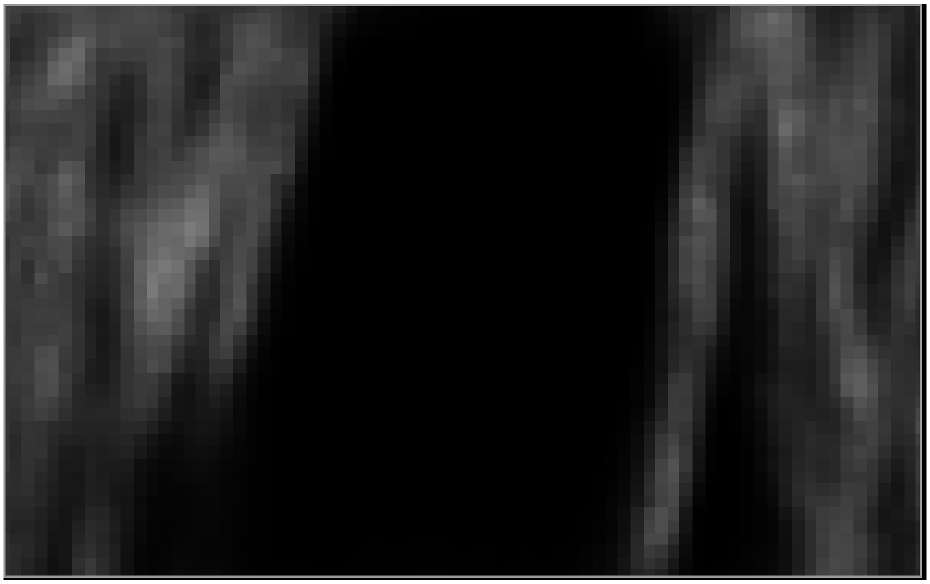

Figure 7.5: YZ orthoslice of a reconstruction from the perpendicular tilt series. This orthoslice is of a plane perpendicular to that shown in Figure 4 and is near the centre of the reconstructed volume. The collagen fibrils run from top to bottom in this orthoslice and the open area in the centre corresponds to the holes seen in the centre of figure 7.4. The structures running from top to bottom are approximately 5 nm wide. The visualized area is 130 nm wide and 70 nm high.

volume. The surface where the greyscale level matches the threshold is defined as the surface of the structure. Choosing a grey level that is too high (dark) will cause the mineral volumes in the reconstruction to include multiple mineral structures in one volume, generating structures that are too large and coarse. A greyscale level that is too low (light) will remove the finest detail from the visualization making the volume appear to contain too little mineral. Use of the automatic selection tools combined with manual correction results in the optimal definition of the surfaces in the reconstructions.

Visualization of the segmented surfaces shows only the surfaces defined by the segmentation parameters. Visualization is very memory intensive, so simplifying the surface by merging facets and smoothing can significantly decrease the processing time. This must be carefully balanced with the need to preserve points of interest in the reconstruction.

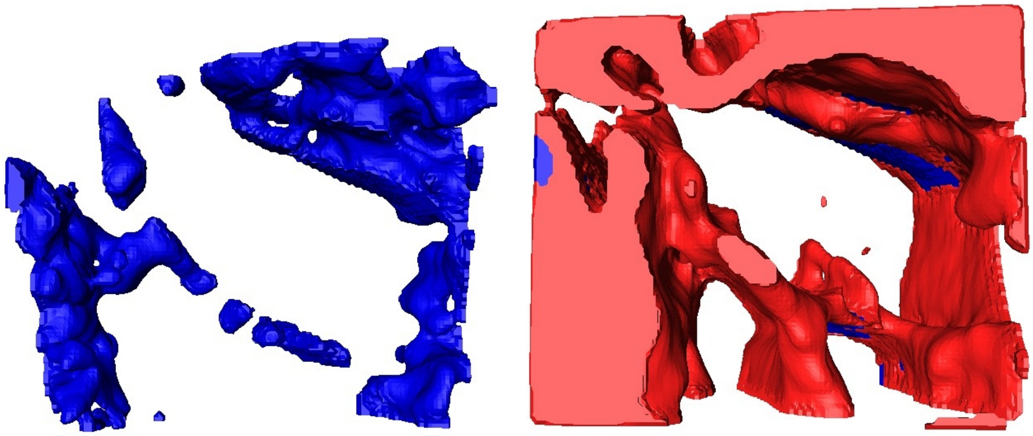

(a) Higher Segmentation Level (b) Lower Segmentation Level

Figure 7.6: Surfaces resulting from choosing different greyscale levels for the interface. In figure 7.6(a) a lighter greyscale level was used and the resulting volume is less than in 7.6(b). Note larger volume identified as mineral in 7.6(b) and absence of small features like the holes shown in the upper right corner of 7.6(a). At some points in 7.6(b) the contrast between neighbouring voxels was sufficient to have the boundary for both volumes at the same point. These points are shown by the blue colour in 7.6(b).

Figure 7.6 shows segmented surfaces from the perpendicular section. In figure 7.6(a) a brighter segmentation greyscale level was chosen (20 0000 on a scale of -32000 to 32000) than in figure 7.6(b) (5000 on a scale of -32000 to 32000). The differences in the resulting surface calculation can be clearly seen. First, the volume enclosed by the surfaces in 7.6(b) is much larger than in 7.6(a). Second, the individual 5 nm thick mineral structures remain distinct in 7.6(a) but are coalesced into larger sections in 7.6(b). In both cases, the mineral surrounds open areas, but the diameter of the open areas decreases with the dark grey level in

7.6(b). This is the same reconstruction and therefore the same underlying dataset, but different visualization parameters cause varying interpretations of the data. Figure 7.6(a) shows a structure that corresponds well with the images prepared by TEM and STEM while figure 7.6(b) shows much larger mineral structures.

Note that, as a result of the selection of higher greyscale levels to define the volumes containing mineral, the visualized forms may in fact represent the merger of two or more mineral structures. Nevertheless, a clearer image of the configuration of these packages of mineral structures in 3-dimensions is obtained with this technique.

7.4 Longitudinal Section Tomography

Alignment of the tilt series images for the longitudinal section was more challenging than alignment of the cross sectioned section's tilt series. The repeating collagen banding and elongation of the mineral along one axis required multiple cross-correlations using varying filtering parameters to obtain good alignment. In the tilt axis alignment task, the shape of the structures mimics the elongation due to a misaligned tilt axis, making this step difficult. The results of the reconstruction are shown in figures 7.7, 7.8, and 7.9.

In figure 7.9, packages of mineral structures are seen oriented parallel to the collagen fibril (which is not shown in the image). As could be seen in normal

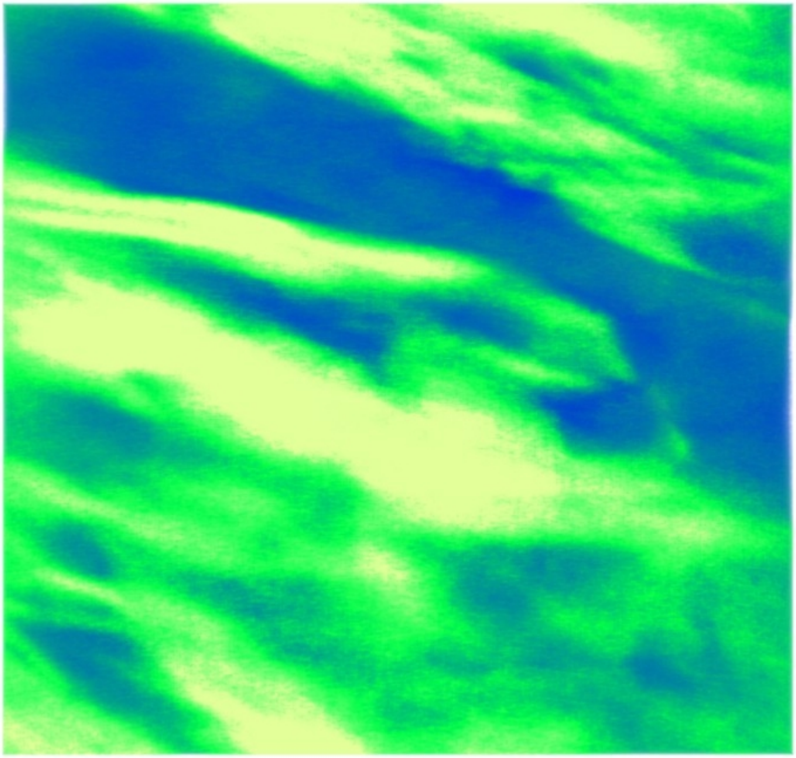

Figure 7.7: Image of a voltex representation of the reconstructed volume created from the tilt series prepared from a longitudinal section. Voxels are represented from blue (low density) to yellow (high density). The reconstructed volume is 275 nm wide, 260 nm high and 75 nm deep

bright-field TEM images (in chapter 4) the mineral structures are stacked parallel to one another and in some cases the software has caused them to merge into these block-like packages also aligned parallel to the fibril. The thinnest structures in this image are 5 nm thick and presumably represent the mineral structures seen in normal TEM images

In the longitudinal section reconstruction, mineral surrounds open areas where the collagen is present. The collagen banding and the mineral expected to be present within the collagen fibrils from the Landis model are not seen in any of the

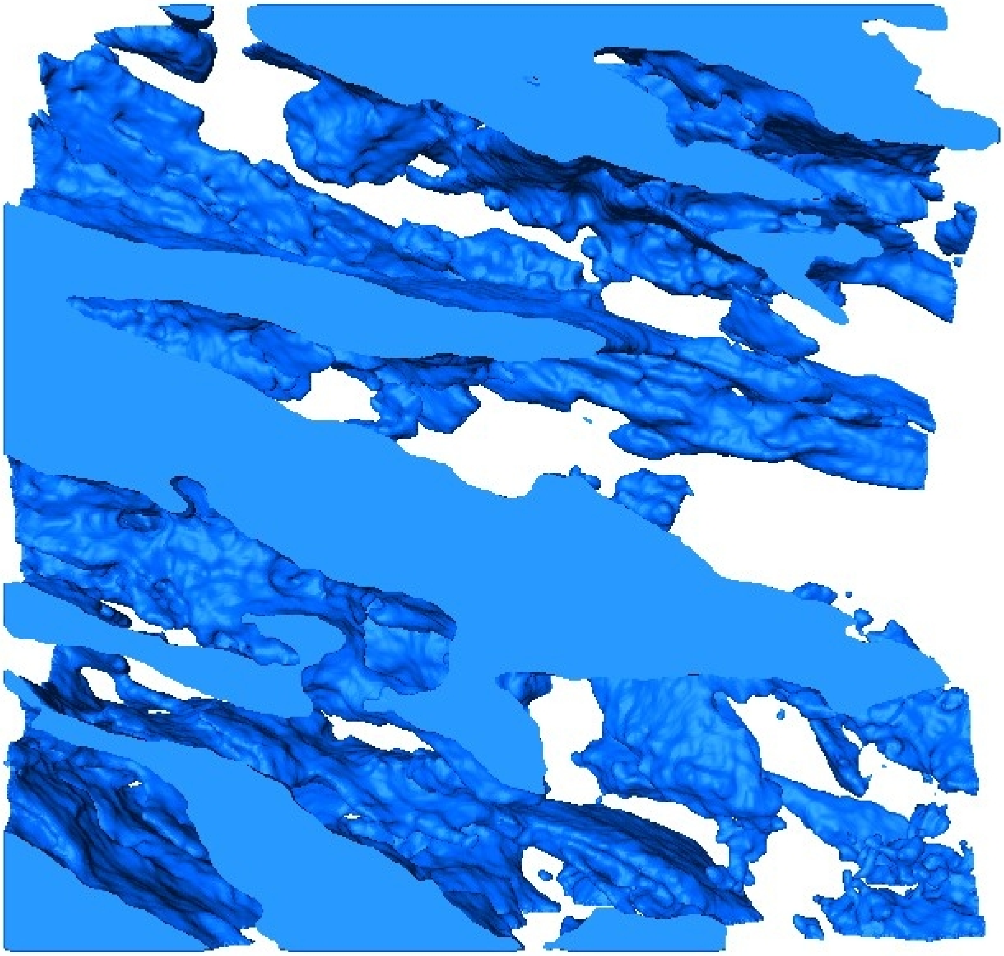

Figure 7.8: Segmented visualization of the reconstruction shown in voltex form in figure 7.7. The collagen fibrils run in the plane of the image. The alignment of the mineral structures parallel to the collagen fibrils can be seen, along with both face on and edge on mineral structures. Open areas are the locations of collagen fibrils. The reconstructed volume is 275 nm wide by 260 nm high by 75 nm thick.

reconstructions (Landis *et al.*, 1996b). The SIRT back projection method uses weighting to remove noise from the model between iterations. The banding, arising from the mineral within the collagen fibrils, has lower contrast than the mineral structure even in HAADF imaging and is removed by the weighting. The FEI software used for the reconstruction allows basic changes to the weighting

Figure 7.9: Segmented Visualization of the Reconstruction Shown in Voltex Form in Figure 7.7, viewed in a direction perpendicular to figure 7.8. This image is looking along the collagen fibrils. The open areas are the collagen fibril channels and the blue is the mineral volume as chosen by segmentation. The segmentation parameter for this tomogram is lower than that for the perpendicular tomogram: the mineral structures appear to be merged together. The dimensions of the reconstruction volume shown in this image are 275 nm wide by 75 nm thick.

parameters, but the use of a different reconstruction software with more control over the parameters may provide reconstructions of the collagen banding as well.

7.5 45 Degree Section Tomography

A tomographic series was collected from a section cut at 45 degrees to the long axis of the femur. As the section was tilted the transition from plates arranged circumferentially around a fibril (figure 7.10) to plates arranged parallel to the fibril axis (figure 7.11) was visualised. Once again, the selection of grey-level cutoff has resulted in coalescence of multiple mineral structures into elongated blobs.

Figure 7.10: Segmented visualization of the reconstructed volume created from the 45 degree section. This view is looking down the collagen fibrils. Open areas are the locations of collagen fibrils. The reconstructed volume is 260 nm wide by 160 nm high.

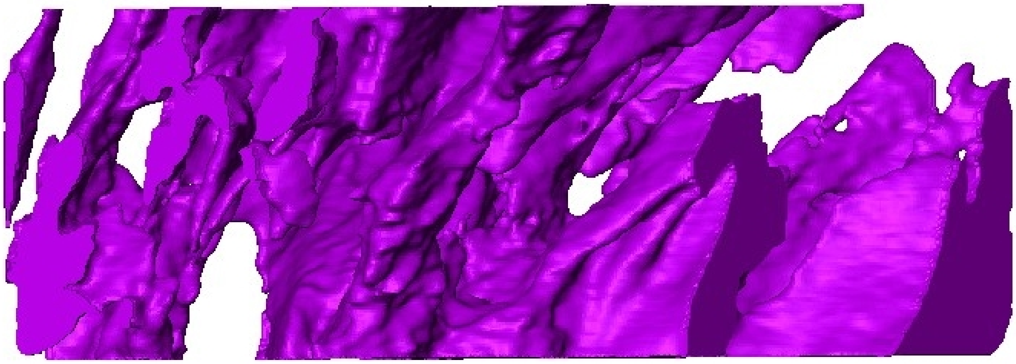

Figure 7.11: Segmented visualization of the reconstructed volume created from the 45 degree section, viewed perpendicular to figure 7.10. Note the inclined angle of the mineral structures relative to the surfaces of the sample. The reconstructed volume is 260 nm wide by 100 nm thick.

7.6 Video Visualization of Tomography Results

Video files of the three reconstructions are included on a DVD accompanying the thesis. The files show the structure resulting from the reconstruction of the three tilt series. All three reconstructions show similar structures: open, roughly circular channels surrounded by material. The segmentation limit for the three videos varies. In the video of the perpendicular section, prepared using the highest segmentation parameter, the individual mineral structures are resolved. The 45 degree section using the lowest segmentation parameter shows the individual mineral structures merged into larger volumes. The rotation seen in the video files emphasises the way the mineral structures area are aligned around the open areas containing the collagen fibrils and the difference between the open structure viewed down the collagen axis and the dense structure viewed across the collagen axis.

7.7 Comparison of BF and HAADF Tomography Results

The tomographic images help to define the three-dimensional form of the mineral structures seen in cross section in the TEM images of previous chapters. In earlier tomographic studies by Landis et al. on mineralized turkey tendon and embryonic bone (Landis *et al.*, 1993, 1996b), the mineral was seen as irregular, quasi-planar structures with their long axes oriented parallel to the fibril axis. The structures are oriented in parallel arrays as seen in figure 1.8, the result of using bright-field images. At some angles, the strong contrast created by the crystals aligned for diffraction at that angle would cause those crystals to appear much brighter than crystals with only mass thickness contrast arising from not being oriented correctly for diffraction at that angle. During the back projection iterations, the diffracting crystals would be emphasized and the non-diffracting crystals would be removed from the structure. HAADF images remove the strong contrast from diffraction, result in the contrast varying monotonically with the path length of the electron beam and therefore allow crystals in all orientations to be visualised after the tomographic reconstruction.

7.8 Chapter Summary

Z-contrast tomography removes the diffraction contrast from the tilt series to allow tomographic reconstruction of crystalline materials. Using this technique on cortical bone samples shows that the external mineral is arranged around cylindrical channels where the collagen is located. This is unlike previous bright-field tomography where the mineral was shown arranged in parallel arrays through the fibrils.

Chapter 8

Calculation of External Mineral Percentage

Sasaki et al. estimate the percentage of intra- and extrafibrillar mineral from their images to be 23 % and 77 % respectively (Sasaki *et al.*, 2002). On examination of their AFM images, they assert that 20 % of the surface of the collagen fibril remains unmineralized. Other groups have reported estimates of 65 % (Bonar *et al.*, 1985) and 75 % (Pidaparti *et al.*, 1996) for the percentage of extrafibrillar mineral in bone. Cross sectional TEM images and tomography of samples prepared by ion milling show that the mineral completely surrounds the fibril, so these estimates are somewhat questionable. With the energy dispersive X-ray spectroscopy results, images from ion milled samples, and tomography results, an estimation of the external percentage of mineral is calculated for this work.

A region of a longitudinal sample showing gap, overlap and mineral regions was found and EDXS measurements of the three regions of interest are made as shown in figure 8.1(c) and table 8.1.

Site number	Site Description	Ca Counts from Integrated EDXS Peak Area
1	Mineral	702
2	Collagen Overlap Zone	166
3	Collagen Gap Zone	455

Table 8.1: Integrated EDXS Ca counts for the three areas shown in figure 8.1.

The EDXS peak intensity measurements show that the three regions have varying Ca levels as the EDXS counts are directly proportional to the amount of Ca present in the volume chosen. There are five assumptions to be made that allow the calculation of the intra- and extrafibrillar mineral in bone.

First, the mineral in the gap zone does not extend into the overlap zone. This assumption is based on the appearance of the collagen banding in the longitudinal sections. When the banding appears, the boundary between the gap zone and the overlap zone is sharply defined. The boundary would not be crisp if the mineral extended into the collagen. Also, the banding will not appear if the section is not cut perfectly parallel to the collagen fibril.In a tilt series acquired for tomography the banding appears and disappears over a range of 10 degrees due to smearing effects as discussed in the Chapter 4.

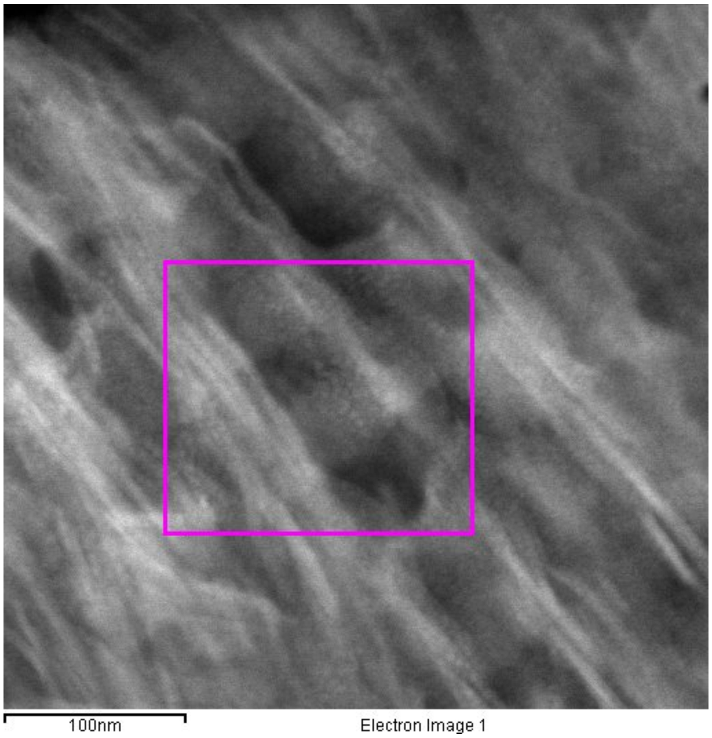

(a) STEM Image

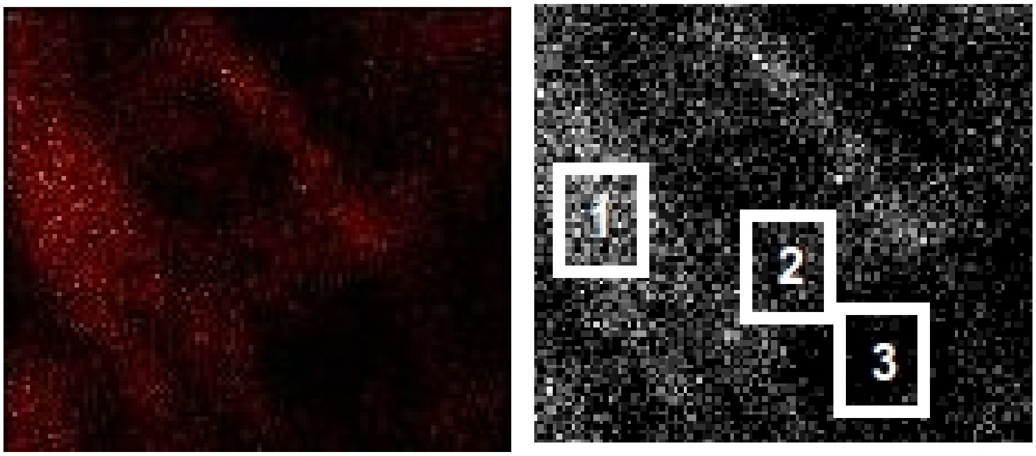

(b) Calcium Counts

(c) Measurement Locations

Figure 8.1: 8.1(a) STEM image of a longitudinal section of human femur cut parallel to the long axis of the bone. 8.1(b) Ca EDXS counts for the area indicated on the STEM images. 8.1(c) locations of sites used to calculate external mineral percentage. Area 1 is a mineral structure, Area 2 is the gap zone and area 3 is the overlap zone. EDXS Ca counts are given in table 8.1.

The second assumption is derived from the first and assumes that the Ca counts in the overlap zone come from the extrafibrillar mineral overlying or underlying the collagen in a face-on manner. Based on the first assumption, there should be no mineral and therefore no calcium in the collagen at this location within the fibril. Ca counts in this area must therefore come from extrafibrillar mineral.

Third, the overlying and underlying mineral is further assumed to have a constant thickness over the entire sample, so it accounts for a percentage of the counts arising in the gap region and the mineral area. The remainder of the counts in the gap region are from the intrafibrillar mineral.

Based on these first three assumptions, the data in table 8.1 is adjusted to account for the overlaying layer of mineral. The overlaying mineral counts are subtracted from all three areas resulting in table 8.2.

Site number	Site Description	Modified Ca Counts from Integrated EDXS Peak Area
1	Mineral	536
2	Collagen Overlap Zone	0
3	Collagen Gap Zone	289
4	Over/Underlying Mineral	166

Table 8.2: Modified EDXS Ca counts for the three areas shown in figure 8.1(a).

The fourth assumption is that the mineral lies either perpendicular or parallel to the surface of the sample and that the collagen fibril has a square cross section. This simplification will over estimate the collagen overlap and gap zone volume and result in an underestimation of the amount of external mineral.

Finally, it is assumed that the volume contains only collagen and mineral. There are no other proteins present and no empty spaces in the structure.

The size of the area modelled is described by measurements from images in the longitudinal and cross sections. The width of collagen fibrils is approximately 50 nm, as measured on the cross sectioned lacy images and the stripe spacing in the longitudinal sections. The thickness of mineral between the collagen fibrils averages 22 nm from the cross sectioned samples. The area used for calculation is the length of one collagen banding repeat (gap + overlap length), by the width of a collagen fibril and mineral bundle. The result is an area 67 nm long by 72 nm wide, as shown in figure 8.2.

The area shown on the right of figure has 3 layers. The overlying and underlying mineral in figure 8.2 form the outer layers 67 nm long by 72 nm wide, while the middle comprises the collagen fibrils and external mineral structures. 22 x 67 nm of the middle layer is mineral, while 50 by 67 nm is the collagen fibril. Of the collagen, 65 by 40 nm is the gap zone while 50 x 20 nm forms the overlap zone. The thickness of the layers is unknown and does not enter into the calculation.

The Ca counts that occur from the overlying and underlying zones and the 22 x 67 nm area of the mineral comprise the counts from the external mineral while the counts arising from the 40 by 50 nm collagen gap zone are the internal mineral. Multiplying the areas of the site by the number of counts from that area in table 8.2 gives the total number of counts from each site (table 8.3). The ratio between the internal and external Ca counts represents the ratio of internal and external mineral

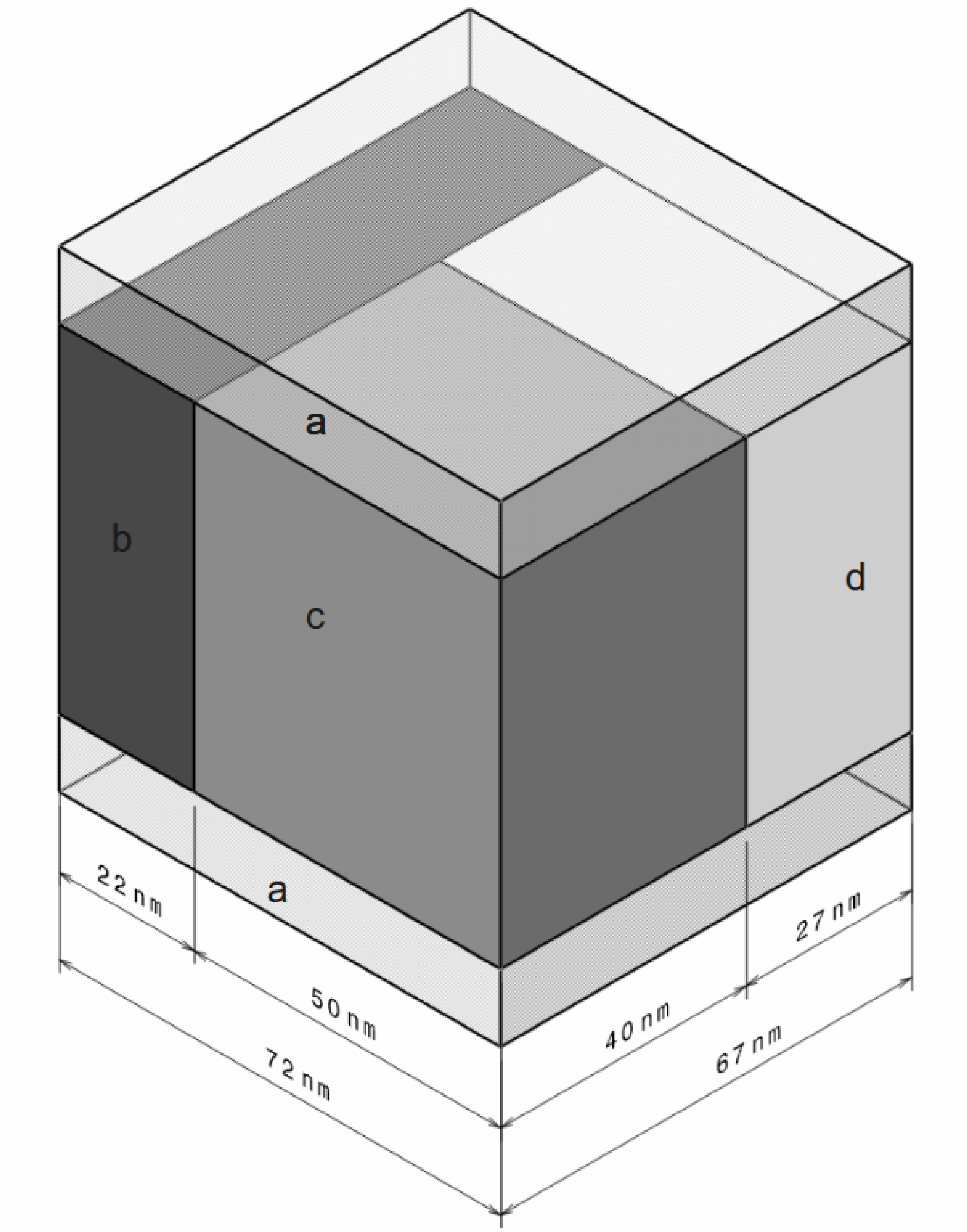

Figure 8.2: Diagram of model used for external mineral calculation. (a) represents the overlaying and underlying mineral, (b) represents the external mineral adjacent to the collagen fibrils, (c) is the overlap zone and (d) is the gap zone.

as EDXS counts are proportional to the amount of the element present. Since Ca is present only in the mineral, its EDXS counts are directly proportional to the amount of mineral present.

Site	Site letter in figure 8.2	Site Area (nm^2)	Calculated Counts in Area	Percentage of Counts
External Mineral	b	1474	790064	36
Collagen Overlap Zone	c	1350	0	0
Collagen Gap Zone	d	2000	578000	27
Over/Underlying Mineral	a	4824	800 784	37

Table 8.3: Calculations of the percentage of mineral that is external to the collagen fibrils based on the model described in the text and by figure number 8.2

From table 8.3 it is seen that 73% of the mineral is external to the collagen fibrils. The calculated error on this value is +/- 4%. Repetitions of the EDXS collection and calculation on other samples give external mineral percentages of 83 ± 5 % and 84 ± 5 %, with an average of 80 ± 6 % This result fits well with the suggestions of Sasaki et al. that 77 % of mineral in mature bovine femora is external to the collagen fibril and with Bonar et al.'s results showing that that at most 35% of mineral in mature bovine bone could be within the fibrils (Sasaki *et al.*, 2002; Bonar *et al.*, 1985). Models of bone mechanical behaviour also show that a large portion of the mineral ($\sim$75 %) must be extrafibrillar to obtain the observed mechanical properties of bone as a material (Pidaparti *et al.*, 1996). The Hodge-Petruska model for collagen has 12 volume % gap zones (Hodge & Petruska, 1963), while bone is 40 to 45 volume % mineral (Jager & Fratzl, 2000), meaning 70 to 73 volume % of mineral should be external to the collagen fibril. This large percentage of external mineral contradicts the gap zone mineral model which is prevalent in publications (Landis *et al.*, 1996b; Weiner & Traub, 1986; Traub *et al.*, 1992; Weiner & Traub, 1989; Arsenault, 1988). This work is based on adult bone, rather than the previously mentioned embryonic bone or mineralizing turkey leg tendon. These results are more conclusive about the properties and structure of fully mineralized bone.

8.1 Chapter Summary

EDXS counts combined with the simplified model for the external mineral in cortical bone presented in chapter 5 allow the calculation of the percentage of mineral that is external to the collagen fibrils. The calculation shows that approximately 80% of the mineral in bone is external to the collagen fibrils. This is in agreement with results from modelling (Pidaparti *et al.*, 1996), AFM (Sasaki *et al.*, 2002) and neutron scattering (Bonar *et al.*, 1985) of 75, 77 and minimum 65 % external mineral respectively.

Chapter 9

Conclusions

Cryogenic ion milling is an effective method for creating samples of human cortical bone for TEM. The resulting samples show less distortion and damage than ultramicrotomed samples, allowing better imaging quality and therefore understanding of the structure of cortical bone. The addition of a thin, approximately 5 nm, coating of amorphous carbon reduces charging and damage of the sample under the electron beam.

Images of samples cut parallel to the long axis of the human femur, called longitudinal sections, show the characteristic 67 nm collagen banding. Running perpendicular to the banding are elongated structures with higher levels of Ca and P atoms according to energy dispersive X-ray spectroscopy (EDXS) results. Diffraction patterns confirm the presence of HA in the sample and dark-field imaging shows that the structures are made of hydroxyapatite, so they are referred to as mineral structures. There is some evidence that the mineral structures are polycrystalline but no conclusions are made about that point. No Bragg scattering appears to arise from the gap zones, but no attempt is made to interpret the nature of the Ca-P rich material in these zones.

Samples cut perpendicular to the long axis of the human femur show a very different motif than longitudinal samples. The mineral structures have no overall alignment, instead they are arranged tangentially around roughly round open areas. This arrangement has been shown previously in the literature by Cressey and Cressey using modern sheep bone (Cressey & Cressey, 2003), but was not fully investigated and has not been previously shown in human bone. The dimensions of the open areas correspond well to the known diameter of type I collagen fibrils in human bone and are therefore concluded to be the location of the collagen fibrils.

The mineral structures that tangentially surround the collagen are approximately 5 nm thick in the collagen radial direction, 65 nm wide in the tangential direction and 200 nm long parallel to the collagen long axis. An average of 5 mineral structures are sandwiched between collagen fibrils. The thickness and width of the mineral structures correspond well to published reports from other researchers; however, the length is much longer. It is believed this increased length is due to the cryostage ion milling preserving the structure which can be damaged by the plastic deformation induced by ultramicrotoming.

The result is a simplified model for cortical bone structure as shown in figure 9.1.

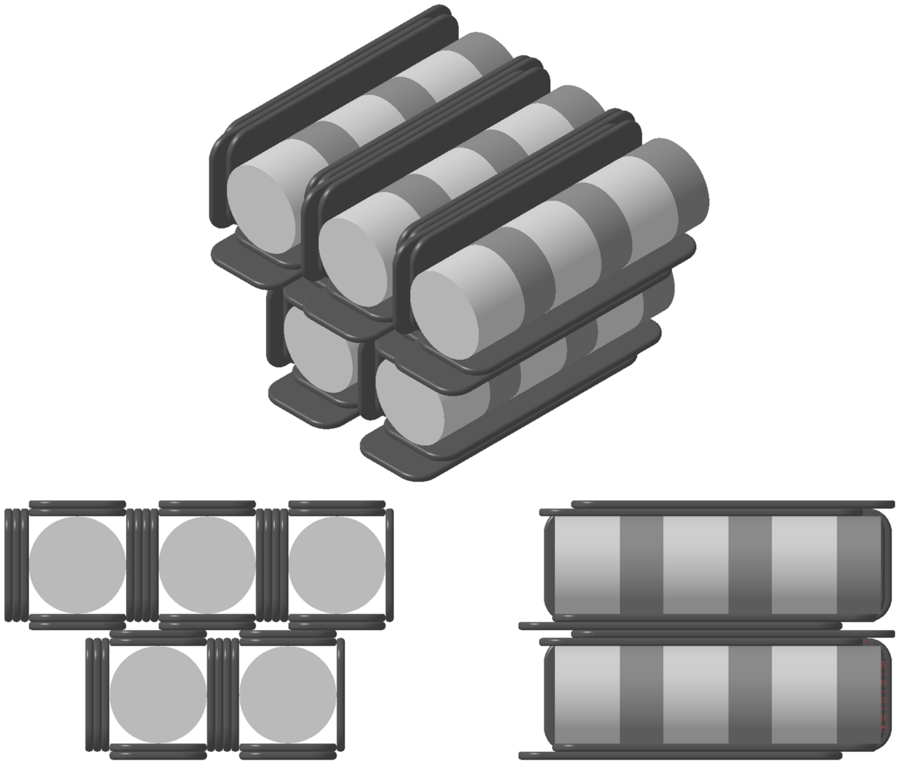

Figure 9.1: A simplified model of the external mineral in bone structure. 45 nm diameter collagen fibrils are surrounded by 200 nm long, 65 nm wide, 5 nm thick plates of mineral. The gap zones of the collagen are also filled with mineral, as indicated by the banding present in the fibril. The top image shows the model in an isometric view. The bottom left shows the model projected down the fibril long axis, as if it were a perpendicular section. The bottom right shows the model projected across the collagen fibrils, as if it were a longitudinal section.

While tomography has been performed previously on bone (Landis *et al.*, 1996b), that work used bright-field images which do not provide the required monotonic relationship between contrast and the beam path length through a single material. Z-contrast STEM imaging removes the diffraction contrast from the images collected for tomography providing the required variation in contrast with only thickness. Using SIRT backprojection for reconstruction verified that the majority of the mineral is external to the collagen fibrils, but could not recreate the collagen banding present in the samples. This is likely due to the backprojection parameters selected as well as the lower content of mineral in the gap zones as inferred from EDXS measurements . The reconstruction also confirmed that the external mineral's long axis is aligned with the collagen fibril's long axis and the mineral structures are oriented tangentially around the collagen fibrils in all directions.

Using EDXS results and the measurements of collagen fibril diameter and mineral structure size, a model was created to calculate the percentage of extrafibrillar mineral. To obtain the EDXS results, 80 % of the mineral in bone must be extrafibrillar. This model fits well with reports from groups working with AFM (Sasaki *et al.*, 2002), neutron diffraction (Bonar *et al.*, 1985) and mechanical modelling (Pidaparti *et al.*, 1996) but contradicts the gap zone model developed from earlier tomography and TEM results (Landis *et al.*, 1996b).

It is noteworthy that the observations summarized here were made on some thirty sections cut from essentially random locations within a sample of human femoral cortex. It is inferred that the model derived from these observations is applicable to all the bone within this cortical sample, regardless of whether it resides inside primary lamellar bone, or within secondary osteonal bone. Furthermore, the limited study of bovine bone suggests that the same model would be applicable to this material and leads to the suggestion that this structure of bone may be common across the mammals.

9.1 Future Work

This work has principally focused on cortical bone from a healthy 60 year old male. While the samples have been consistent for this individual, extension of the work to other samples from individuals with varied ages, sexes and diseases would be important. The techniques described in this thesis allow quantitative examination of the structure and variation of bone. Further nanoscale study of bone would lead to a better understanding of the way bone is affected by ageing and disease. The diseases and conditions could include osteoporosis, Paget's disease, osteogenesis imperfecta and osteomalacia.

Second, genetically modified or "Knockout" mice with varying bone densities could be used to show if the bone density variation is due to a change in the number of mineral structures or to a change in the size of the mineral structures. Both reasons are plausible and may be dependent on the gene chosen for modification.

Further study into the nature of the bone mineral structures is important to help understand the controls of mineralization. This study has some data that suggests that the mineral structures are polycrystalline, but further microscopic work is needed to fully characterize the mineral structures. For instance, HA has a hexagonal crystallographic structure which is expected to produce hexagonal crystals, not plates. How and why does the HA in bone form plates? Also, understanding the surface of the mineral structures and how they maintain their size, hold together, and nucleate are important for understanding the biological processes involved in mineralization.

A final area of interest would be examination of the reconstruction parameters used in the tomography software. As mentioned in the tomography chapter, different software packages allow varying levels of control over the reconstruction algorithm. To reconstruct the collagen banding, a wider choice of parameters is necessary and that may require a different reconstruction software package.

Appendix A

Statistical Data

Measurements were made using Gatan's Digital Micrograph software. The histogram tool within the software was used for measurements as it shows the edges of the structures as steep changes in the pixel intensity (see figure A.1). Film images were calibrated using known standards, while digital images used the camera's calibration. The maximum systemic error on each measurement is estimated as the width of two pixels. In all cases, the width of two pixels is less than 1 nm and the pixel size is given in the sections below. Repeated measurements of the width of mineral structures in longitudinal sections allowed a pooled variance of 0.155 nm to be calculated. Since this is less than the width of two pixels, the measurement error on all measurements is assumed to be two pixels wide.

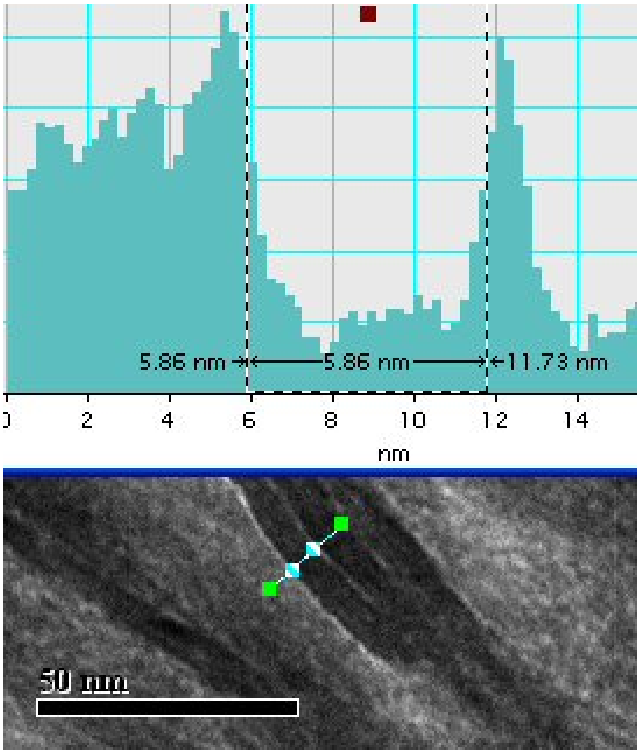

Figure A.1: The histogram tool is used to measure objects on calibrated images in Gatan's Digital Micrograph software. A histogram is drawn across the feature of interest, then the width is measured on the histogram.

A.1 Measurement of Mineral Structure Thickness Using a Longitudinal Section

The sample used is a piece of human femur cut parallel to the long axis of the femur (see figure A.2). Measurements of the thickness (smallest dimension) are shown in table A.1. The average of the thickness measurements from the longitudinal image is 4.8 nm with a standard deviation of 0.9 nm. The dataset is normally distributed at

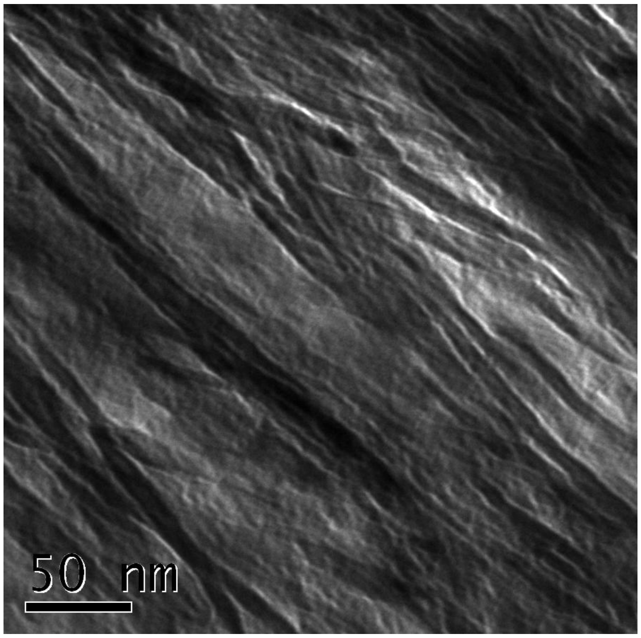

Figure A.2: Bright-field image of a sample cut parallel to the long axis of a human femur. Measurements of the thickness of the mineral structures were used for statistical purposes.

a significance (p-value) of 0.05. The measurement error is +/- 0.66 nm as the pixel size in this images is 0.33 nm.

5.4	5.1	4.4	4.8	3.7
4.4	4.0	4.4	5.4	3.0
3.7	4.4	5.8	3.8	4.2
5.5	6.7	6.4	5.7	5.4
5.0	4.7	4.4	5.0	5.4

Table A.1: Measurements (in nm) of mineral structures width (shortest direction) as seen in figure A.2.

A.2 Bundle Spacing in Longitudinal Section

The sample used is a piece of human femur cut parallel to the long axis of the femur. Measurement of the bundle spacing was performed on the image shown in figure A.3. The spacing between the bundles is given in table A.2. The average spacing in this image is 52.6 nm with a standard deviation of 12.7 nm. The error on the measurements is +/- 0.68 nm as the pixel size in this image is 0.34 nm.

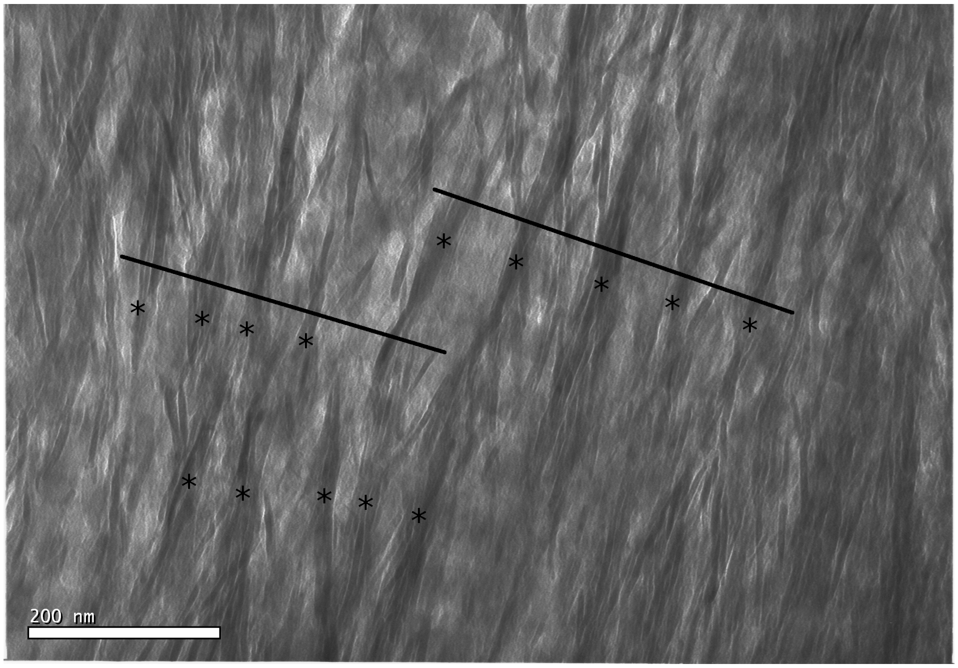

Figure A.3: Bright-field image of a sample cut parallel to the long axis of a human femur. Measurements of the thickness of the mineral structures were used for statistical purposes.

63.5	60.1	59.5	66.3	37.1	38.1	43.0

Table A.2: Measurements (in nm) of the distance between mineral bundles as seen in figure A.3.

A.3 Bundle Width in Longitudinal Section

The sample used is a piece of human femur cut parallel to the long axis of the femur. Measurement of the bundle spacing was performed on the image shown in figure A.3. The bundle width is given in table A.3. The average width in this image is 22.6 nm with a standard deviation of 7.4 nm. The measurement error is +/- 0.68 nm as the pixel size in this image is 0.34 nm.

22	31	17	14	29

Table A.3: Measurements (in nm) of the bundle width seen in figure A.3. All measurements are in nm.

A.4 Measurement of Mineral Structure Thickness using Perpendicular Section

The sample used is a piece of human femur cut perpendicular to the long axis of the femur (see figure A.4). Measurements were made in Gatan's Digital Micrograph Software using the microscope's calibration for scale and can be seen in table A.4. The average of the thickness measurements from the perpendicular image is 4.9 nm with a standard deviation of 0.9 nm. The dataset is normally distributed at a significance (p-value) of 0.05. The measurement error is +/- 0.36 nm as the pixel size in this image is 0.18 nm.

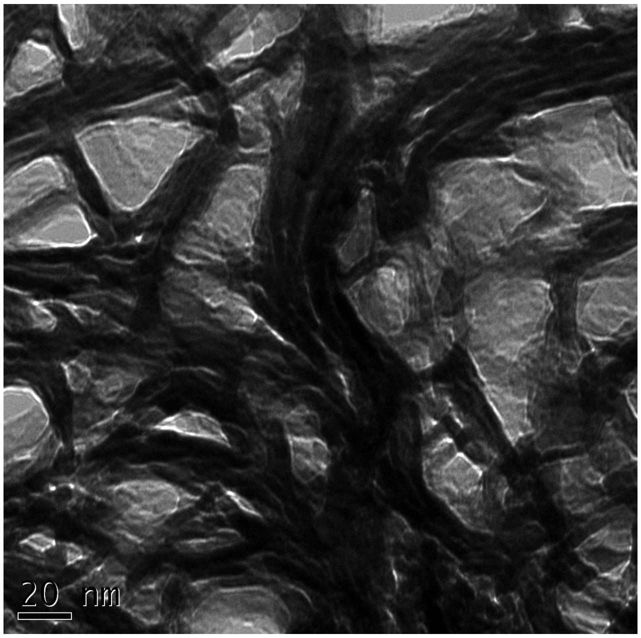

Figure A.4: Bright-field image of a sample cut perpendicular to the long axis of a human femur. Measurements of the thickness of the mineral structures were used for statistical purposes.

4.8	3.7	6.0	4.9	5.6
3.8	3.8	4.3	4.2	4.0
5.3	6.0	3.3	5.1	4.7
5.4	6.6	4.9	3.8	5.8
5.1	6.7	5.4	4.5	4.7

Table A.4: Measurements (in nm) of mineral structure thickness (shortest direction) as seen in figure A.4.

A.5 Student's t-test of Thickness Measurements

To determine if the thickness measurements from the the perpendicular sections is from the same distribution as the thickness measurements from the longitudinal sections, a Student's t-test is used. Both datasets (A.4 and A.1) are normally distributed so the t-test is appropriate. The results at a significance value (p-value) of 0.05 show that the means of the two datasets do not vary.

A.6 Measurement of Mineral Structure Width using Perpendicular Section

The sample used is a piece of human femur cut perpendicular to the long axis of the femur. It was imaged in bright-field mode and the image was recorded digitally in Gatan's Digital Micrograph format using the Philips CM-12 microscope and its Orius digital camera from Gatan (see figure A.5). Measurements were made in Gatan's Digital Micrograph Software using the microscope's calibration for scale and can be seen in table A.5. The average of the width measurements from the perpendicular image is 68.1 nm with a standard deviation of 18.8 nm. The measurement error in this image is +/- 0.64 nm as the pixel size is 0.32 nm.

49.1	50.0	80.6	65.9
55.1	67.1	116.5	59.2
66.6	63.1	76.34	

Table A.5: Measurements (in nm) of mineral structure width (longer direction) as seen in figure A.5.

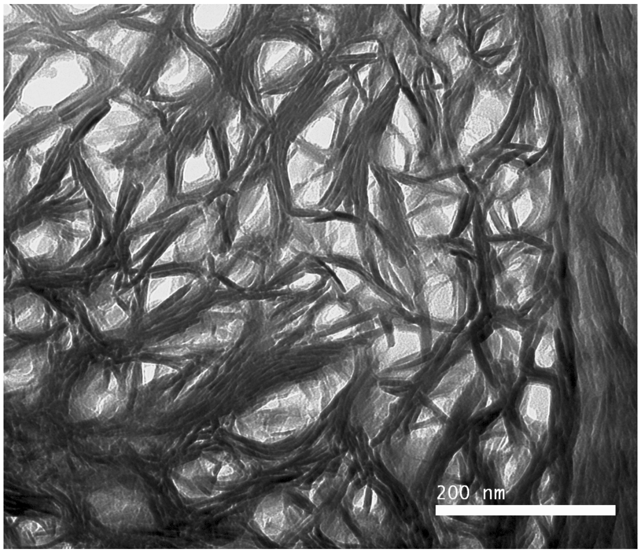

Figure A.5: Bright-field image of a sample cut perpendicular to the long axis of a human femur. Measurements of the width the mineral structures, the open areas and the width of the mineral bundles between the open areas were used for statistical purposes.

A.7 Average Diameter of Open Areas in Perpendicular Section

The sample used is a piece of human femur cut perpendicular to the long axis of the femur. It was imaged in bright-field mode and the image was recorded digitally in Gatan's Digital Micrograph format using the Philips CM-12 microscope and its Orius digital camera from Gatan (see figure A.5). Measurements were made in Gatan's Digital Micrograph Software using the microscope's calibration for scale and can be seen in table A.6. The two measurements in each row are for the same open area. The two measurements in each row were made perpendicular to each other. The average of the open area measurements is 45.4 nm with a standard deviation of 22.8 nm. The measurement error in this image is +/- 0.64 nm as the pixel size is 0.32 nm.

37.3	20.9
44.2	26.5
59.5	35.5
26.5	69.7
17.0	21.4
86.2	88.1
49.2	32.0
51.6	41.6
41.9	25.4
44.7	38.4
29.0	23.2
60.1	109.8
43.6	74.4
31.6	43.1

Table A.6: Measurements (in nm) of the open areas surrounded by mineral structure sin figure A.5. Each row represents the measurements of one area and the two measurements are made perpendicular to each other.

A.8 Average Thickness of Crystal Dividers in Perpendicular Section

The thickness of the mineral dividers between the open areas in the perpendicular sections were measured on the image shown in figure A.5. The measurements are shown in table A.7. The average width of the dividers is 27.7 nm with a standard deviation of 10.4 nm. The measurement error in this image is +/- 0.64 nm as the pixel size is 0.32 nm.

23.4	15.5	39.3	29.1
31.1	13.5	42.7	34.7
38.6	19.3	17.4	

Table A.7: Measurements (in nm) of the mineral dividers between the open areas figure A.5. Each row represents the measurements of one area and the two measurements are made perpendicular to each other.

A.9 Uniformity of Angular Distributions of Mineral Structures in Perpendicular Sections

A uniformity test was used to determine that the mineral structures in the perpendicular section are randomly oriented. The data used for this test is the angle of the line running along the long axis of the mineral structure with respect to an arbitrary line drawn on figure A.5. The angle was measured to a degree using a copy of the image on a rotating light table. The angles measured from the images are given in table A.8. The same mineral structure has two angular measurements 180 ° apart, so the values above 180° have 180° subtracted to get a value below 180°. Then to check that the spread of results is random over 180°, the angular measurements are doubled, as described in Davis (2002).

The test requires sorting the data in ascending order, then assigning an order statistic that represents its place in the ordered list. The following statistics are calculated for each data point:

$$D_n^+ = \frac{1}{n} - x_1, \frac{2}{n} - x_2, ..., 1 - x_n$$

$$D_n^- = x_1, x_2 - \frac{1}{n}, x_3 - \frac{2}{n} - x_2, ..., x_n - \frac{n-1}{n}$$

where x_n is the n^{th} data point and n is the total number of data points in the set. The maximum values of both D_n^+ and D_n^- are found and substituted into the V_n equation:

$$V_n = D_{nmax}^+ + D_{nmax}^-$$
$$V = V_n(n^{\frac{1}{2}} + 0.155 + \frac{0.24}{n^{\frac{1}{2}}})$$

Then a value of V for the data set is calculated. This value is compared with a critical value for V from Fisher (1993). If V is higher than the critical value, the dataset is not uniformly distributed.

For this dataset D_{nmax}^+ is 0.077, D_{nmax}^- is 0.109, V_n is 0.186 and V is 1.60. For an α (probability of type I error) of 0.10, $V_{critical}$ is 1.620, therefore this dataset is randomly oriented. This means there is no overall ordering of the direction of the mineral structures in the cross sectioned images.

232	307	36	333	34	50	103	68	140	270
293	312	329	251	225	155	96	47	323	280
253	251	200	136	187	242	175	92	99	140
221	254	327	307	231	290	0	49	1	101
152	52	87	31	91	61	341	284	282	346
47	130	102	66	19	10	311	234	156	115
61	56	139	287	345	291	273	238	135	112
67									

Table A.8: Angular measurement, in degrees, of 71 mineral structures in figure A.5. This data was used to verify the randomness of the direction of the mineral structures in the sample.

A.10 Ultramicrotomed Bovine Longitudinal Mineral Structure Lengths

The sample used is a piece of bovine cut parallel to the long axis of the femur, then ultramicrotomed to electron transparency. Measurement of the length of mineral structures was performed on the image shown in figure 6.3. The mineral structure lengths are given in table A.9. The average width in this image is 37 nm with a standard deviation of 12 nm. The measurement error is +/- 0.66 nm as the pixel size in this images is 0.33 nm.

28.6	48.2	33.4	62.9	20.4
36.5	31.3	30.6	46.3	31.3

Table A.9: Measurements (in nm) of mineral structures of a longitudinal ultramicrotomed section seen in figure 6.3.

A.11 Ion Milled Bovine Longitudinal Mineral Structure Lengths

The sample used is a piece of bovine cut parallel to the long axis of the femur, then ion milled to electron transparency. Measurement of the length of mineral structure was performed on the image shown in figure 6.4. The mineral structure lengths are given in table A.10. The average width in this image is 77 nm with a standard deviation of 32 nm. The measurement error is +/- 0.66 nm as the pixel size in this images is 0.33 nm.

63.7	59.6	50.7	62.9	44.1
51.3	104.6	80.5	134.5	118.9

Table A.10: Measurements (in nm) of mineral structures in figure 6.4.

A.12 Ultramicrotomed Bovine Perpendicular Mineral Structure Lengths

The sample used is a piece of bovine cut parallel to the long axis of the femur, then ultramicrotomed to electron transparency. Measurement of the length of mineral structures was performed on the image shown in figure 6.5. The mineral structure lengths are given in table A.11. The average width in this image is 26 nm with a

40.7	19.6	17.9	14.9	30.6
31.7	47.1	13.1	26.3	14.5

Table A.11: Measurements (in nm) of mineral structures of a perpendicular ultramicrotomed section seen in figure 6.5.

standard deviation of 12 nm. The measurement error is +/- 0.66 nm as the pixel size in this images is 0.33 nm.

A.13 Ion Milled Bovine Longitudinal Mineral Structure Lengths

The sample used is a piece of bovine cut perpendicular to the long axis of the femur, then ion milled to electron transparency. Measurement of the length of mineral structures was performed on the image shown in figure 6.6. The mineral structure lengths are given in table A.12. The average width in this image is 54 nm with a standard deviation of 18 nm. The measurement error is +/- 0.66 nm as the pixel size in this images is 0.33 nm.

58.4	88.3	30.3	55.3	43.8
35.4	65.7	58.5	69.4	38.4

Table A.12: Measurements (in nm) of mineral structures in figure 6.6.

Appendix B

Tomography Resolution

The resolution of a tomographic reconstruction is not the same as the resolution of the tilt series. Along the tilt axis in the reconstruction, the resolution is that of the images, while in the other two orthogonal directions the minimum resolution is lowered by

$$d_{yorz} = \frac{\alpha D}{N}$$

Where the number of images in the tilt series (N), the maximum tilt angle of the series (α) and the size of the objects being reconstructed (D) form the resolution in the other directions (d_{yorz}).

This equation holds for non-spherical objects or thin flat samples if D is defined as the maximum path length the electron beam travels in the sample (McEwen & Heagle, 1997). This path length is

$$D = \frac{T}{\cos \gamma}$$

where γ is is the maximum tilt angle and T is the thickness of the sample.

The geometry of the electron microscope means that the tilt series does not contain a full 180 degrees of information. At high tilt angles, the sample holder and the thickness of the sample will prevent images being taken. These missing images at tilt angles are referred to as the missing wedge. The higher the maximum tilt angle used in the experiment, the more reliable the three dimensional reconstruction. Figure B.1 from Midgely and Weyland shows the importance of obtaining data over a large tilt range. As the maximum angle of the tilt series increases, the accuracy of the reconstruction improves (Midgley & Weyland, 2003).

The resolution of a reconstruction can be estimated by combining the Crowther equation and the thin film equation, resulting in the formula:

$$d = \frac{\alpha T}{N cos \alpha}$$

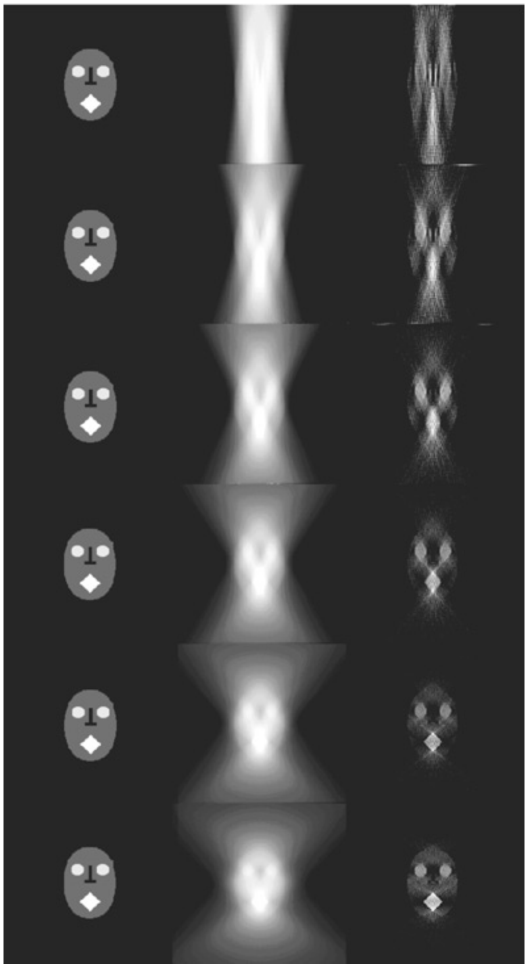

Figure B.1: Modelling the effect of different maximum angles in the tilt series on the validity of the reconstruction. From top down the angles start at 10° and finish at 60° in 10° increments. From Midgley & Weyland (2003).

where α is the maximum tilt angle in the tilt series, T is the thickness of the sample, and N is the number of images in the tilt series (Frank, 1992).

The smallest features of interest in this work are the 5 nm thick mineral structures. The number of images in the tilt series is 93 for the cross section, 91 for the parallel section and 78 for the 45 degree section. The estimated resolution depends on the number of images taken and the thickness of the sample. Because the sample is of finite thickness, at higher angles the path length of the electron beam through the sample is longer.

The combined Crowther-Thin Film resolution estimation equation uses the number of images in the tilt series, but does not say if the steps should be equally spaced or not. In this data the tilt series used tilt steps of 2 degrees between -60 and 60 degrees but 1 degree above ± 60 degrees. The estimated resolution is therefore calculated twice for each tilt series as shown in table B.1. The first calculation removes extra tilt steps above 60 degrees and uses an evenly spaced tilt step for the full tilt range. The second calculation uses the total number of images taken. Both calculations result in resolutions that are much higher than what is seen in the reconstruction. The calculated resolutions of the three tilt series for a 100 nm sample thickness are given in table B.1.

Sample	Maximum Tilt Angle	Equally Spaced Images	Total Number of Images	Equally Spaced Resolution	Total Resolution
Longitudinal	75	75	91	6.74 nm	5.56 nm
Perpendicular	76	77	93	7.12 nm	5.9 nm
45 Degree	72	69	78	5.89 nm	5.23 nm

Table B.1: Estimated resolution values for the tomographic reconstructions of the three tilt series. Equally spaced resolution disregards the odd tilt steps above 60 degrees, therefore using fewer images than the tilt series contains. Total resolution counts both the even and odd tilt steps above 60 degrees in the number of images.

The resolution of the tilt series images is sufficient to see demarcation between individual mineral structures (figures 7.1 and 7.2). These structures can also be resolved in the orthoslices of the reconstructions(figures 7.4 and 7.5) the individual mineral sections can still be resolved, indicating that the resolution of the reconstruction is much higher than the estimations would suggest. The Crowther and thin film equations do not take into account the resolution of the images in the tilt series. It seems apparent that a higher resolution tilt series will lead to a higher resolution tomographic reconstruction. As well, the addition steps in the tilt series improve the resolution in the direction perpendicular to the tilt axis even more (Weyland, Personal Communication, 2009).

Appendix C

Tomography .AVI files

The included CD includes 6 .AVI files showing the tilt series and reconstructions of the tomographic work. The files are:

- 45 degree section reconstruction.avi
- 45 degree section tilt series.avi
- Longitudinal section reconstruction.avi
- Longitudinal section tilt series.avi
- Perpendicular section reconstruction.avi
- Perpendicular section tilt series.avi

References

Alberts, B., Bray, D., Lewis, J., Raff, M., Roberts, K., & Watson, J. D. 1989. *Molecular Biology of the Cell*. 2nd edn. New York: Garland Publishing.

Arsenault, A. L. 1988. Crystal-collagen relationships in calcified turkey leg tendons visualized by selected-area dark field electron microscopy. *Calcified Tissue International*, **43**(4), 202–212.

Arsenault, A. L. 1989. A comparative electron microscopic study of apatite crystals in collagen fibrils of rat bone, dentin and calcified turkey leg tendons. *Bone and Mineral*, **6**(2), 165–177.

Arsenault, A. L., & Grynpas, M. D. 1988. Crystals in calcified epiphyseal cartilage and cortical bone of the rat. *Calcified Tissue International*, **43**(4), 219–225.

Baron, R. 2003. General Principles of Bone Biology. *Chap. 1, page 1 of:* Favus, M. J. (ed), *Primer on the Metabolic Bone Diseases and Disorders of Mineral Metabolism*, 5th edn. Washington, D.C.: American Society for Bone and Mineral Research.

Baumeister, W., Grimm, R., & Walz, J. 1999. Electron tomography of molecules and cells. *Trends in Cell Biology*, **9**(2), 81–85.

Bonar, L. C., Roufosse, A. H., Sabine, W. K., Grynpas, M. D., & Glimcher, M. J. 1983. X-ray diffraction studies of the crystallinity of bone mineral in newly synthesized and density fractionated bone. *Calcified Tissue International*, **35**(2), 202–209.

Bonar, L. C., Lees, S., & Mook, H. A. 1985. Neutron diffraction studies of collagen in fully mineralized bone. *Journal of Molecular Biology*, **181**(2), 265–270.

Boyde, A. 1974. Transmission electron microscopy of ion beam thinned dentine. *Cell and Tissue Research*, **152**(4), 543–550.

Boyde, A., & Pawley, J. B. 1976. Transmission electron microscopy of ion erosion thinned hard tissues. *Calcified Tissue Research*, **21 Suppl**(Aug), 117–123.

Boyle, W. J., Simonet, W. S., & Lacey, D. L. 2003. Osteoclast differentiation and activation. *Nature*, **423**(6937), 337–42.

Callister, W. D. 2006. *Materials Science and Engineering: An Introduction*. 7th edn. Wiley.

Chakhmourdian, A. R. 2009. *http://www.umanitoba.ca/geoscience/faculty/arc/apatite.html, Accessed November 10, 2009.*

Cressey, B. A., & Cressey, G. 2003. A model for the composite nanostructure of bone suggested by high-resolution transmission electron microscopy. *Mineralogical Magazine*, **67**(6), 1171–1182.

Davis, J. C. 2002. *Statistics and Data Analysis in Geology, 3rd ed.* John Wiley & Sons, Inc.

Dempster, D. W. 2002. Bone Remodeling. *Page 315 of:* Coe, F. L., & Favus, M. J. (eds), *Disorders of Bone and Mineral Metabolism*, 2 edn. Philadelphia: Lippincott Williams & Wilkins.

Ducy, P., Schinke, T., & Karsenty, G. 2000. The osteoblast: a sophisticated fibroblast under central surveillance. *Science*, **289**(5484), 1501–4.

Elliott, James C. 2002. Calcium Phosphate Biominerals. *Page 427 of:* Kohn, Matthew J., Rakovan, John F., & Hughes, John M. (eds), *Phosphates : Geochemical, Geobiological, and Materials Importance*. Reviews in Mineralogy & Geochemistry. Washington, DC: Mineralogical Society of America.

Engstrom, A., & Fernandez-Moràn, H. 1956. Ultrastructural organization of bone. *Nature*, **178**(4531), 494–495.

Eppell, S. J., Tong, W., Katz, J. L., Kuhn, L., & Glimcher, M. J. 2001. Shape and size of isolated bone mineralites measured using atomic force microscopy. *Journal of Orthopaedic Research*, **19**(6), 1027–1034.

Everts, V., Niehof, A., & Beersten, W. 2003. Transmission Electron Microscopy of Bone. *Page 299 of:* Helfrich, Miep H., & Ralston, Stuart (eds), *Bone Research Protocols*. Bone Research Protocols. Totowa, N.J.: Humana Press.

Fernandez-Moràn, H., & Engstrom, A. 1957. Electron Microscopy and X-Ray Diffraction of Bone. *Biochimica et Biophysica Acta*, **23**, 260–264.

Fisher, N. I. 1993. *Statistical Analysis of Circular Data*. Cambridge, UK: Cambridge University Press.

Frank, J. (ed). 1992. *Electron Tomography: Three-Dimensional Imaging with the transmission Electron Microscope*. New York: Plenum Press.

Fratzl, P., Schreiber, S., & Boyde, A. 1996. Characterization of bone mineral crystals in horse radius by small-angle X-ray scattering. *Calcified Tissue International*, **58**(5), 341–346.

Ge, J., Cui, F.-Z., Wang, X., & Wang, Y. 2007. New evidence of surface mineralization of collagen fibrils in wild type zebrafish skeleton by AFM and TEM. *Materials Science & Engineering C-Biomimetic and Supramolecular Systems*, **27**(1), 46–50.

Gilbert, P. 1972. Iterative methods for the three-dimensional reconstruction of an object from projections. *Journal of Theoretical Biology*, **36**(1), 105–117.

Grills, B. L., & Ham, K. N. 1989. Transmission electron microscopy of undecalcified bone. *Journal of Electron Microscopy Technique*, **11**(2), 178–179.

Harada, S.-I., & Rodan, G. A. 2003. Control of osteoblast function and regulation of bone mass. *Nature*, **423**(6937), 349–55.

Hodge, A. J., & Petruska, J. A. 1963. Recent studies with the electron microscope on ordered aggregates of the tropocollagen molecule. *Page 289 of:* Ramachandran, G. N. (ed), *Aspects of Protein Structure*. Academic Press.

Hohling, H. J., Kreilos, R., Neubauer, G., & Boyde, A. 1971. Electron microscopy and electron microscopical measurements of collagen mineralization in hard tissues. *Zeitschrift fur Zellforschung und Mikroskopische Anatomie*, **122**(1), 36–52.

Hong, S. I., Hong, S. K., & Kohn, D. H. 2009. Nanostructural analysis of trabecular bone. *Journal of Materials Science-Materials in Medicine*, **20**(7), 1419–1426.

Jager, I., & Fratzl, P. 2000. Mineralized collagen fibrils: a mechanical model with a staggered arrangement of mineral particles. *Biophysical Journal*, **79**(4), 1737–1746.

Jantou, V., Turmaine, M., West, G. D., Horton, M. A., & McComb, D. W. 2009. Focused ion beam milling and ultramicrotomy of mineralised ivory dentine for analytical transmission electron microscopy. *Micron*, **40**(4), 495–501.

Jantou-Morris, V., Horton, M. A., & McComb, D. W. 2010. The nano-morphological relationships between apatite crystals and collagen fibrils in ivory dentine. *Biomaterials*, **31**(19), 5275–86.

Jung, Y., Kim, S. H., Kim, Y. H., & Kim, S. H. 2009. The effects of dynamic and three-dimensional environments on chondrogenic differentiation of bone marrow stromal cells. *Biomedical Materials*, **4**(5), 1–7.

Kohn, M. J., Rakovan, J. F., & Hughes, J. M. (eds). 2002. *Phosphates : Geochemical, Geobiological, and Materials Importance*. Washington, DC: Mineralogical Society of America.

Kuhn, L. T., Grynpas, M. D., Rey, C. C., Wu, Y., Ackerman, J. L., & Glimcher, M. J. 2008. A comparison of the physical and chemical differences between cancellous and cortical bovine bone mineral at two ages. *Calcified Tissue International*, **83**(2), 146–154.

Landis, W. J. 1986. A study of calcification in the leg tendons from the domestic turkey. *Journal of Ultrastructure and Molecular Structure Research*, **94**(3), 217–238.

Landis, W. J., & Song, M. J. 1991. Early mineral deposition in calcifying tendon characterized by high voltage electron microscopy and three-dimensional graphic imaging. *Journal of Structural Biology*, **107**(2), 116–127.

Landis, W. J., Song, M. J., Leith, A., McEwen, L., & McEwen, B. F. 1993. Mineral and organic matrix interaction in normally calcifying tendon visualized in three dimensions by high-voltage electron microscopic tomography and graphic image reconstruction. *Journal of Structural Biology*, **110**(1), 39–54.

Landis, W. J., Hodgens, K. J., Song, M. J., Arena, J., Kiyonaga, S., Marko, M., Owen, C., & McEwen, B. F. 1996a. Mineralization of collagen may occur on fibril surfaces: evidence from conventional and high-voltage electron microscopy and three-dimensional imaging. *Journal of Structural Biology*, **117**(1), 24–35.

Landis, W. J., Hodgens, K. J., Arena, J., Song, M. J., & McEwen, B. F. 1996b. Structural relations between collagen and mineral in bone as determined by high voltage electron microscopic tomography. *Microscopy Research and Technique*, **33**(2), 192–202.

Lees, S. 1979. A model for the distribution of HAP crystallites in bone–an hypothesis. *Calcified Tissue International*, **27**(1), 53–56.

Lees, S., Prostak, K. S., Ingle, V. K., & Kjoller, K. 1994. The loci of mineral in turkey leg tendon as seen by atomic force microscope and electron microscopy. *Calcified Tissue International*, **55**(3), 180–189.

McEwen, B. F., & Heagle, A. B. 1997. Electron microscopic tomography: A tool for probing the structure and function of subcellular components. *International Journal of Imaging Systems and Technology*, **8**(2), 175–187.

McEwen, B. F., Radermacher, M., Rieder, C. L., & Frank, J. 1986. Tomographic three-dimensional reconstruction of cilia ultrastructure from thick sections. *Proceedings of the National Academy of Sciences of the United States of America*, **83**(23), 9040–9044.

McKee, M. D., Addison, W. N., & Kaartinen, M. T. 2005. Hierarchies of extracellular matrix and mineral organization in bone of the craniofacial complex and skeleton. *Cells Tissues Organs*, **181**(3-4), 176–88.

Midgley, P. A., & Weyland, M. 2003. 3D electron microscopy in the physical sciences: the development of Z-contrast and EFTEM tomography. *Ultramicroscopy*, **96**(3-4), 413–431.

Moradian-Oldak, J., Weiner, S., Addadi, L., Landis, W. J., & Traub, W. 1991. Electron imaging and diffraction study of individual crystals of bone, mineralized tendon and synthetic carbonate apatite. *Connective Tissue Research*, **25**(3-4), 219–228.

Noguchi, K., Araki, M., & Ohno, Y. 2000. Preparation of transmission electron microscopy specimens of as-drawn gold wire. *Scripta Materialia*, **43**(3), 199–204.

Olsen, B. R. 2003. Bone Morphogenesis and Embryological Development. *Chap. 2, page 9 of:* Favus, M. J. (ed), *Primer on the Metabolic Bone Diseases and Disorders of Mineral Metabolism*, 5th edn. Washington, D.C.: American Society for Bone and

Mineral Research.

Pelttari, K., Steck, E., & Richter, W. 2008. The use of mesenchymal stem cells for chondrogenesis. *Injury*, **39 Suppl 1**(Apr), S58–65.

Pidaparti, R. M., Chandran, A., Takano, Y., & Turner, C. H. 1996. Bone mineral lies mainly outside collagen fibrils: predictions of a composite model for osteonal bone. *Journal of Biomechanics*, **29**(7), 909–916.

Pollard, T. D., Earnshaw, W. C., & Lippincott-Schwartz, J. 2008. *Cell Biology*. Philadelphia: Saunders/Elsevier.

Prostak, K. S., & Lees, S. 1996. Visualization of crystal-matrix structure. In situ demineralization of mineralized turkey leg tendon and bone. *Calcified Tissue International*, **59**(6), 474–479.

Ramachandran, G. N. 1967. *Treatise on collagen*. London ; New York: Academic Press.

Recker, R. R., & Barger-Lux, J. 2002. Embryology, Anatomy, and Microstructure of Bone. *Page 177 of:* Coe, Fredric L., & Favus, Murray J. (eds), *Disorders of Bone and Mineral Metabolism*, 2 edn. Philadelphia: Lippincott Williams & Wilkins.

Robinson, R. A., & Watson, M. L. 1952. Collagen-crystal relationships in bone as seen in the electron microscope. *The Anatomical Record*, **114**(3), 383–409.

Sasaki, N., Tagami, A., Goto, T., Taniguchi, M., Nakata, M., & Hikichi, K. 2002. Atomic force microscopic studies on the structure of bovine femoral cortical bone at the collagen fibril-mineral level. *Journal of Materials Science-Materials in Medicine*, **13**(3), 333–337.

Siperko, L. M., & Landis, W. J. 2001. Aspects of mineral structure in normally calcifying avian tendon. *Journal of Structural Biology*, **135**(3), 313–320.

Speckman, T. W., & Norris, W. P. 1957. Bone crystallites as observed by use of the electron microscope. *Science*, **126**(3277), 753.

Teitelbaum, S. L. 2000. Bone resorption by osteoclasts. *Science*, **289**(5484), 1504–8.

Traub, W., Arad, T., & Weiner, S. 1992. Growth of mineral crystals in turkey tendon collagen fibers. *Connective Tissue Research*, **28**(1-2), 99–111.

Tzaphilidou, M. 2005. The role of collagen in bone structure: an image processing approach. *Micron*, **36**(7-8), 593–601.

Viguier, B., & Mortensen, A. 2001. Heating of TEM specimens during ion milling. *Ultramicroscopy*, **87**(3), 123–133.

Volkert, C. A., Busch, S., Heiland, B., & Dehm, G. 2004. Transmission electron microscopy of fluorapatite-gelatine composite particles prepared using focused ion beam milling. *Journal of Microscopy*, **214**(Pt 3), 208–12.

Wagner, D. R., Lindsey, D. P., Li, K. W., Tummala, P., Chandran, S. E., Smith, R. L., Longaker, M. T., Carter, D. R., & Beaupre, G. S. 2008. Hydrostatic pressure enhances chondrogenic differentiation of human bone marrow stromal cells in osteochondrogenic medium. *Annals of Biomedical Engineering*, **36**(5), 813–820.

Weiner, S., & Price, P. A. 1986. Disaggregation of bone into crystals. *Calcified Tissue International*, **39**(6), 365–375.

Weiner, S., & Traub, W. 1986. Organization of hydroxyapatite crystals within collagen fibrils. *FEBS letters*, **206**(2), 262–266.

Weiner, S., & Traub, W. 1989. Crystal size and organization in bone. *Connective Tissue Research*, **21**(1-4), 259–265.

Weiner, S., & Traub, W. 1992. Bone structure: from angstroms to microns. *The FASEB Journal*, **6**(3), 879–885.

Weiner, S., Arad, T., & Traub, W. 1991. Crystal organization in rat bone lamellae. *FEBS Letters*, **285**(1), 49–54.

Williams, D. B., & Carter, C. B. 1996. *Transmission electron microscopy : a textbook for materials science*. New York: Plenum Press.

Ziv, V., & Weiner, S. 1994. Bone crystal sizes: a comparison of transmission electron microscopic and X-ray diffraction line width broadening techniques. *Connective Tissue Research*, **30**(3), 165–175.